Imperial College
London

Development of Diode Pumped Alexandrite Lasers

Xin Sheng

Thesis submitted in partial fulfilment of the requirements for the degree of Doctor of Philosophy of Imperial College London

Photonics Group
The Blackett Laboratory, Department of Physics
Imperial College London, United Kingdom

September 2019

I declare that all work in this thesis is my own. Information used or derived from the work of others has been appropriately cited at each instance. A list of references is provided at the end of the thesis.

Copyright declaration

Acknowledgements

It is a genuine pleasure to express my deep sense of thanks to my supervisor Prof. Mike Damzen for always being supportive and constantly offering me invaluable help throughout my PhD. His scientific approach, timely suggestions and meticulous scrutiny have helped me to accomplish the PhD program. His sense of humour and beautiful singing have made my research life full of joy.

I profusely thank Dr. Ara Minassian for his kind support and assistance at every stage of my research. His extensive experience and inspirational thinking have deeply impressed me. I must thank Dr. Gabrielle Thomas for her patient guidance at the beginning of my PhD program. Her help and encouragement have contributed immensely to my thesis. I am grateful to Dr. Juna Sathian and Goronwy Tawy for the pleasant cooperation experience. I want to thank Dr. William Kerridge-Johns and Alexander Coney for sharing instruments in the lab, discussing academic problems together and offering me advice. Thanks also go to my friends at Imperial College London for making these four years such a wonderful experience.

I sincerely thank my parents for bringing me to this world and the sacrifices they have made to help me finish my studies.

I owe a deep sense of gratitude to Miss. Meihui Yang for her concern and encouragement throughout my PhD life. I am very grateful to her for spending this precious time with me.

Abstract

This thesis is focused on the development of diode-pumped Alexandrite lasers, especially in terms of understanding and optimizing their performance. Alexandrite possesses excellent physical properties and broad wavelength tunability (701-858 nm). Diode pumping of Alexandrite is a promising route to construct simple, compact and low-cost laser systems, which can enable a multitude of precision applications including remote sensing (LIDAR) light sources.

This thesis work presents the first demonstration of a Q-switched Alexandrite laser under CW diode pumping. The Q-switched laser was operated with pulse repetition rates up to 10 kHz. Pulses with maximum peak power of 1.19 kW were obtained at 1 kHz repetition rate. By modifying the already Q-switched laser system, a cavity-dumped Q-switched system was developed to generate shorter pulses. Pulses with considerably shorter duration of 2.9 ns and increased pulse energy of 200.8 μJ were produced. These correspond to a peak power of 69.2 kW which is more than 60 times that of the standard Q-switched operation.

This thesis also reports the first wavelength-tunable passively Q-switched diode-pumped Alexandrite laser using a semiconductor saturable absorber mirror (SESAM). The Q-switched wavelength tuning was achieved between 775 and 781 nm using a birefringent plate. Highly stable pulses with 73 mW average power, 6.9 μs pulse duration and 11.2 kHz repetition rate were obtained in fundamental TEM_{00} mode with excellent spatial quality ($M^2 < 1.1$).

Lastly, the first single-longitudinal-mode (SLM) operation of a CW Alexandrite ring laser under diode pumping was presented in this work. An ultra-compact bow-tie ring cavity with astigmatic compensation was developed. The unidirectional operation of the ring laser was realized using an optical diode consisting of a Faraday rotator and a half-wave plate, which resulted in the SLM output with power >1 W in TEM_{00} mode. The wavelength was tuned between 727 and 792 nm. These successful pulsed and continuous-wave operations promote the prospect of diode-pumped Alexandrite lasers in light source applications.

Publications

Journal papers

Xin Sheng, Goronwy Tawy, Juna Sathian, Ara Minassian, and Michael J. Damzen, "Unidirectional single-frequency operation of a continuous-wave Alexandrite ring laser with wavelength tunability," Opt. Express **26**, 31129-31136 (2018).

U. Parali, **X. Sheng**, A. Minassian, G. Tawy, J. Sathian, G. M. Thomas, and M. J. Damzen, "Diode-pumped Alexandrite laser with passive SESAM Q-switching and wavelength tunability," Opt. Commun. **410**, 970–976 (2018).

G. M. Thomas, A. Minassian, **X. Sheng**, and M. J. Damzen, "Diode-pumped Alexandrite lasers in Q-switched and cavity-dumped Q-switched operation," Opt. Express **24**, 27212–27224 (2016).

Conference submissions

Xin Sheng, Goronwy Tawy, Juna Sathian, Ara Minassian, and Michael J. Damzen, "Unidirectional single-frequency operation of a wavelength-tunable red-diode-pumped Alexandrite ring laser," in 8th EPS-QEOD Europhoton Conference, ThP.24 (2018).

Xin Sheng, Ufuk Parali, Gabrielle M. Thomas, Ara Minassian, and Michael J. Damzen, "Passively SESAM Q-switched red-diode-pumped Alexandrite laser," in Conference on Lasers and Electro-Optics Europe & European Quantum Electronics Conference (CLEO/Europe-EQEC), CA-P.1 (2017).

Gabrielle M. Thomas, Ara Minassian, William Kerridge-Johns, **Xin Sheng**, Alexander Coney, and Michael J. Damzen, "High power and high energy diode-pumped Alexandrite lasers," in Conference on Lasers and Electro-Optics Europe & European Quantum Electronics Conference (CLEO/Europe-EQEC), (2017).

Ufuk Parali, Gabrielle M. Thomas, Ara Minassian, **Xin Sheng**, and Michael J. Damzen, "Wavelength tunable passively Q-switched Alexandrite laser with direct diode-pumping at 635 nm," in 5th International Conference on Photonics, Optics and Laser Technology (PHOTOPTICS), (2017).

Contents

List of Figures

List of Tables

List of Abbreviations

MASER	Microwave amplification by stimulated emission of radiation
DPSS	Diode-pumped solid-state
FWHM	Full width at half maximum
YAG	Yttrium aluminum garnet
GGG	Gadolinium gallium garnet
YVO_4	Yttrium orthovanadate
$GdVO_4$	Gadolinium vanadate
MgF_2	Magnesium fluoride
CW	Continuous-wave
SESAM	Semiconductor saturable absorber mirror
TEM	Transverse electric magnetic
BPP	Beam parameter product
FP	Fabry–Pérot
TMD	Transverse mode discrimination
GSA	Ground state absorption
ESA	Excited state absorption
LIDAR	Light Detection and Ranging
BM	Back mirror
OC	Output coupler

HR	Highly reflecting
HWP	Half-wave plate
VCL	Vertical cylindrical lens
BBO	Beta barium oxide
KDP	Potassium dihydrogen phosphate
KD*P	Potassium dideuterium phosphate
CdTe	Cadmium telluride
BiFi	Birefringent filter

Chapter 1

Introduction

Lasers are devices that generate coherent monochromatic light through an optical amplification process based on the stimulated emission of radiation. The theoretical foundations for lasers was established by Einstein in 1917 [1]. An atom in an excited state transits from a higher energy level to a lower one, releasing energy in the form of a photon. If the photon emission is induced by an incident photon with suitable photon energy, this process is called stimulated emission. The photon is emitted into the mode of the incident photon. In effect, the incident radiation is amplified via this process. Moreover, the optical properties of the two photons are highly consistent, thus resulting in beams that are distinguished from ordinary light sources by their coherence, monochromaticity, brightness and directionality.

The advent of lasers is inseparable from the contributions of scientists and engineers over the last century. In 1954, Townes, Gordon and Zeiger realized the predecessor of the laser – microwave amplification by stimulated emission of radiation (MASER) [2]. The theoretical principles governing the operation of a maser were also proposed independently by Prokhorov and Basov [3,4]. Townes and Schawlow later described the principles of the maser and extended the principle to optical frequencies in 1958 [5]. Subsequently, Maiman successfully demonstrated the first laser operation using a ruby crystal optically pumped by a flashlamp in 1960 [6]. Since then, many different types of lasers have been developed, including solid-state, gas, liquid and semiconductor lasers. Lasers have revolutionized optical technology, enabling a wide range of applications in fields such as manufacturing, data storage, displays, optical communications, metrology, military and medicine.

A typical laser consists of a gain medium, a resonant cavity and a pump source. The pump source supplies energy to the gain medium that is able to amplify light through stimulated emission. The pump energy can be provided in a variety of ways, for example, in the form of optical, electrical and chemical pumping. The gain medium is positioned inside the resonant cavity that provides optical feedback with the most common type of resonant cavity consisting of a pair of mirrors. Light bounces back and forth between these two mirrors, passing through the gain medium repeatedly, and is amplified with each pass. Usually, one of the two mirrors is used as an output coupler, which allows a portion of the intracavity light to transmit through. The transmitted light is the output of the laser, which can be used in further applications.

Solid-state lasers are lasers that use solid-state gain media such as crystals or glasses doped with laser active ions (in most cases rare earth or transition metal ions). They can be fabricated in the form of bulk lasers or fiber lasers. Optical pumping is most commonly required for solid-state lasers with the choice of pump source depending on the gain medium used. Discharge lamps have been widely used as pump sources, however, they lead to a relatively low efficiency. In contrast, laser diodes tend to be more efficient and cost-effective, and have become more commonly used for solid-state lasers. In view of these advantages, the work in this thesis is concerned with the investigation and development of diode-pumped lasers based on Chromium-doped chrysoberyl (also known as Alexandrite), whose high efficiency and broadband tunability enable many real-world applications.

The outline of this chapter will be as follows. First, an introduction to laser diodes and solid-state laser materials is conducted, which includes the internal structure and working principle of the diodes, as well as the classification of solid-state materials. Then the history of solid-state lasers is briefly reviewed, and some of the important tunable solid-state lasers are compared, with the aim of showing their respective advantages. Different types of pumping schemes applicable to solid-state lasers are then introduced. This chapter concludes with an overview of the thesis.

1.1 Diode-pumped Solid-state Lasers

Solid-state laser materials are typically pumped either by discharge lamps or laser diodes. Discharge lamps are divided into two categories: arc lamps and flash lamps. Arc lamps are employed for continuous pumping, whereas flash lamps generating pump pulses can be used for pulsed operation of solid-state lasers. Both arc and flash lamps essentially consist of a quartz tube attached to metal electrodes and filled with a noble gas (e.g. Xenon or Krypton) [7]. An electric current is discharged through the gas filled tube creating hot plasmas. These plasmas radiate intense light that can be used to excite laser media. Due to its ability to achieve high optical power with relatively low cost, lamp pumping has been widely used, especially for high power systems. However, some disadvantages restrict its applications, such as a very limited lifetime (maximum of a few thousand hours) and low wall-plug efficiency (up to a few percent) [8]. In addition, discharge lamps are relatively noisy pump sources, resulting in a high level of laser noise. For example, relatively strong pulse-to-pulse fluctuations are often exhibited by lamp-pumped Q-switched lasers.

Diode-pumped solid-state (DPSS) lasers have become critically important in the laboratory and commercial markets. Compared with the discharge lamps, laser diodes are more compact, require low electrical power, and have long lifetimes. Furthermore, the efficiency of a solid-state laser can be greatly increased by selecting a laser diode with narrow emission bandwidth that matches the absorption peak of the gain medium. Diode pumping is, therefore, capable of providing significant improvements in overall system compactness, efficiency and reliability.

The diode pumping of solid-state lasers was initially hampered by the low output power and high cost. In the mid-1980s, significant advances were made in the development of linear laser diode arrays based on aluminium gallium arsenide (AlGaAs) quantum well technology [9]. Continued improvements over the next three decades have given rise to laser diodes with superior performance in output power, slope efficiency and wavelength control. These improvements, along with reduced cost, have led to an increase in demand for laser diodes in optical pumping. With the development of reliable high-power laser diodes, parallel improvements in DPSS lasers have also taken place. Through the direct use of laser diodes, DPSS lasers offer advantages including narrow linewidth and high beam quality.

1.1.1 Laser Diodes

A laser diode is a semiconductor device in which a laser beam is created at the diode's p-n junction, which is a boundary between two types of semiconductor materials. One of the two materials is doped with a material that liberates electron holes to form a p-type material, whereas the other is doped with electron donors to create an n-type material. When a positive voltage is applied to the p-material and a negative one to the n-material, electrons and holes will be driven into the p-n junction, and electron-hole recombination occurs in this region. In this process, electrons transfer from the conduction band to the valence band, which is accompanied by energy release in the form of photons. A population inversion can be achieved by injecting a high current through the p-n junction. Optical feedback is provided by a Fabry-Perot resonator that is usually formed by the cleaved end faces of semiconductor wafer [7].

Figure 1.1 shows the structure of an AlGaAs laser diode that consists of a stack of several semiconductor layers with varying thickness. The layer of the structure that produces the gain is the 'active layer' of the p-n junction. The active layer, with a thickness ranging from 0.1 to 0.3 μm, is sandwiched between n-AlGaAs and p-AlGaAs layers. These two layers are deposited onto n-GaAs and p-GaAs substrates, respectively. Current is passed through the diode via a metallic contact at the bottom of the n-GaAs layer and a stripe contact on the insulating layer [7]. The laser light emitted from the device is generated in the active layer as shown. Since the light is emitted from both end faces, high-power diodes are typically coated with a highly reflective film at the rear face [10].

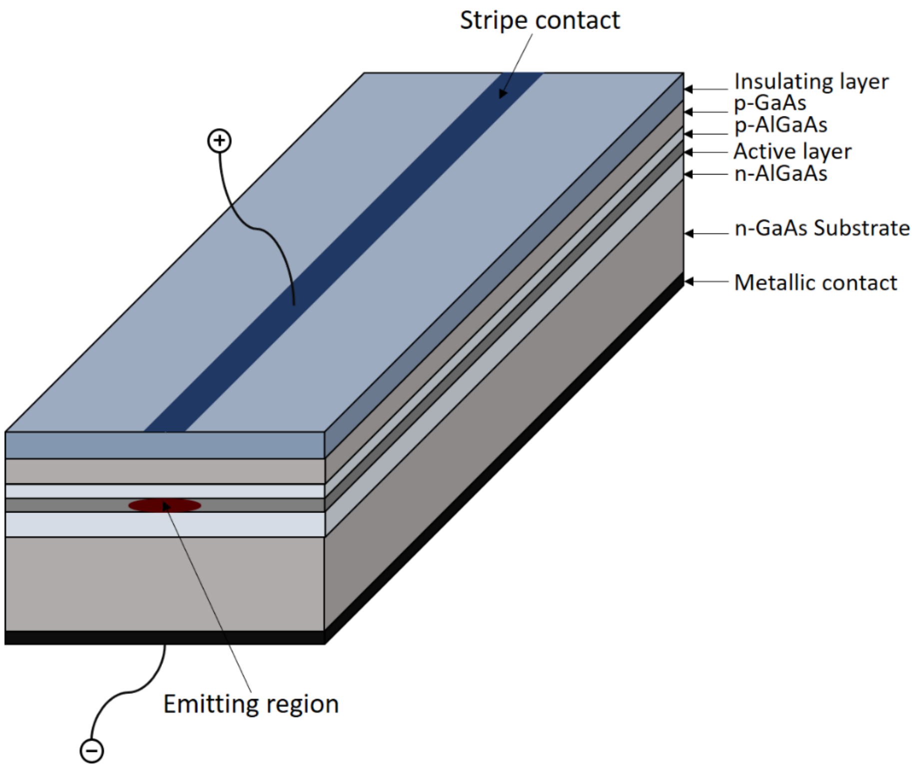

Figure 1.1. Schematic of a heterojunction laser diode. Adapted from [10].

This type of diode is referred to as a broad strip or single-emitter laser diode as the emitting region has the shape of a broad stripe. Because of the asymmetry of the emitter, the spatial properties of the emitted beam are different in the horizontal and vertical directions. The output beam emerging from a laser diode is illustrated in Figure 1.2. The beam in the horizontal direction (x) with a low divergence angle (typically 10° FWHM) is many times diffraction limited. By contrast, the beam in the vertical (y) is diffraction limited and diverges faster with a typical divergence angle of 40° (FWHM) [10]. Hence, the output from the diode is asymmetrical and requires additional collimating optics for beam shaping. For instance, a micro lens can be mounted near the emitting surface of the device to reduce the vertical divergence angle [7].

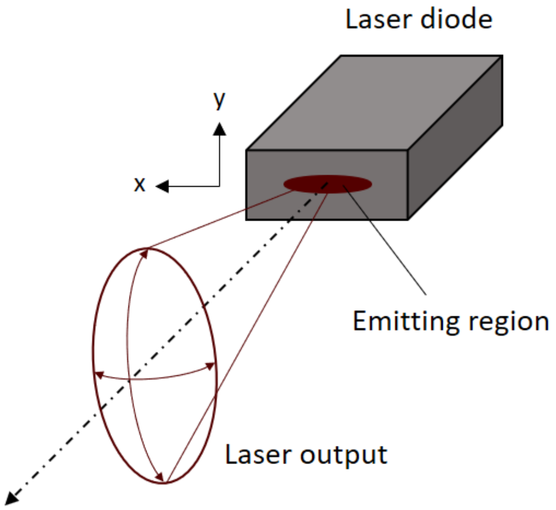

Figure 1.2. The spatial distribution of the output beam from a laser diode. Adapted from [10].

On its own, a single-emitter diode laser provides very limited pump power (normally sub-watt level). To overcome this limitation, diode bars that contain a one-dimensional array of single emitters can be used to provide a high-power beam. Typically, a diode bar contains 10 to 50 independent emitters and has a width of 10 mm [7]. In this configuration, optical power up to tens of watts can be produced, but the beam quality is relatively poor. Multiple diode bars can be further stacked vertically or horizontally to form a single diode module, which is capable of generating extremely high powers up to hundreds or even thousands of watts. Furthermore, unlike discharge lamps, light from laser diodes can be coupled into optical fibers. Fiber-coupled laser diodes can deliver a circular intensity profile with a symmetric beam quality, which is very convenient in many cases. These two types of diode modules are used in this work, and the detailed content will be presented in Section 4.1.

The center wavelength and the spectral width of laser diodes are important for pumping solid-state lasers. The emission wavelength (λ) of a laser diode is inversely proportional to the energy difference (ΔE) between the valence and conduction band, which can be expressed by

$$\lambda = \frac{hc}{\Delta E} \tag{1.1.1}$$

where h is the Planck's constant, and c is the speed of light. The energy difference (or the bandgap) is determined by the chemical composition of the semiconductor material. For example, the emission wavelength of an AlGaAs laser diode is dependent on the ratio of Al to Ga in the active layer, and it can be tailored over a broad range (from 720 to 850 nm) by altering the ratio [11]. The lower the Al concentration, the longer the wavelength. Other than the chemical composition of the semiconductor material, the emission wavelength is also affected by temperature. For example, the peak emission of an AlGaAs device changes by 0.3 nm with a temperature change of 1 °C [7]. Varying emission wavelengths due to temperature changes is often minimised using heat sinks. Table 1 summarizes the emission wavelengths of some common laser diodes. All active layer materials listed in the table are grown on a GaAs or InP substrate.

Table 1. The emission wavelengths of some common semiconductor laser diodes [11].

Material/Substrate	Emission wavelength (nm)
AlGaAs/GaAs	720-850
InGaAsP/InP	1200-1650
InGaAs/GaAs	900-1100
InGaAlP/GaAs	630-700

On the other hand, the spectral linewidth of a diode beam is very narrow (typically with only a few nanometers). For example, a stacked array consisting of 10 bars has a linewidth of 2.2 nm. For solid-state lasers with only a short absorption path, pumping with a laser diode that possesses a narrow spectral width allows most of the pump radiation to be absorbed. However, the linewidth becomes less important for optically thick materials since the pump radiation can be fully absorbed over the long distance [7].

1.1.2 Solid-state Laser Materials

The gain medium of a solid-state laser is a solid-state material, which comprises a host material doped with active ions (typically rare-earth or transition metal ions). This material absorbs and emits optical radiation when operating as a laser, thus its properties are critical to the laser performance. The host material determines the macroscopic mechanical, optical and thermal properties of the gain medium, whereas the active ions defines the spectroscopic properties of the laser and give rise to significant differences in lasing characteristics.

Host materials are required to withstand the rigorous operating conditions of practical lasers. Favourable properties include appropriate hardness, high resistance to mechanical stress, chemical stability, absence of refractive index variations, high thermal conductivity, low thermo-optic coefficients and high thermal fracture limit [7]. Appropriate hardness allows for high quality crystal cutting and polishing. Refractive index variations cause inhomogeneous propagation of light in the crystal, which eventually results in poor beam quality. Superior thermal properties can mitigate the effects of thermal lensing during high power operation. Other mentioned properties mainly ensure that the crystal is not susceptible to the external environment and thus has a long lifetime. In addition to these properties, the host crystal also needs to have suitable lattice sites that can accept the dopant ions. Ideally, a high doping concentration of active ions is achievable. However, the high doping concentration might lead to clustering, which is the tendency of the ions to form clusters rather than to disperse randomly in the host material. The clustering effect can severely degrade the laser efficiency through the quenching process [12]. Therefore, the doping concentration requires careful optimization. Generally, solid-state host materials can be divided into two main groups – crystalline solids or glasses.

Crystalline Materials

Since the first ruby laser, a great number of crystalline materials have been investigated as laser gain media. Crystals generally exhibit great hardness, and high thermal conductivity. Oxide crystals like sapphire, vanadate and garnets are one of the most common types of hosts.

Sapphire (Al_2O_3) has a high degree of hardness and high thermal conductivity. The Al site is too small for rare earth ions, so it is typically doped by transition metal ions instead [7]. One example of a sapphire based laser is the ruby laser, where the sapphire host medium is doped with Chromium (Cr^{3+}:sapphire). Another important sapphire-based laser is the Titanium-doped sapphire (Ti^{3+}:sapphire), which offers a significantly broad wavelength tuning range (660-1180 nm).

Garnets are another group of commonly used host materials and have many attractive properties. They are stable, hard and of high thermal conductivity. The most common garnets include yttrium aluminum garnet, $Y_3Al_5O_{12}$ (YAG) and gadolinium gallium garnet, $Gd_3Ga_5O_{12}$ (GGG) [13]. Rare earth ions such as neodymium (Nd^{3+}), thulium (Tm^{3+}), erbium (Er^{3+}) and ytterbium (Yb^{3+}) have been incorporated into garnet crystals. Among them, neodymium-doped yttrium aluminate garnet (Nd^{3+}:YAG) lasers have gained significance and become one of the most common commercial lasers [7].

Vanadates have a strong birefringence that effectively suppresses thermally induced depolarisation loss during high power operation. Similar to garnets, they are doped with rare earth ions (e.g. neodymium, ytterbium, erbium, etc.). Neodymium-doped yttrium orthovanadate ($Nd^{3+}:YVO_4$) is one of the most popular crystals. Compared to Nd:YAG, $Nd:YVO_4$ exhibits a high pump absorption, a large emission cross-section, a broad absorption bandwidth, but a low thermal conductivity [7]. Gadolinium vanadate ($Nd^{3+}:GdVO_4$) is also an attractive crystal, because its absorption cross-section is similar to that of $Nd:YVO_4$, whereas its thermal conductivity is higher than that of Nd:YAG [14,15].

Glasses

Compared to crystals, ion-doped glasses have wide bandwidths, which enable broad wavelength tuning ranges and the generation of ultrashort pulses. The enormous size capability and ease-of-fabrication feature allow glasses to be fabricated in a variety of sizes and shapes and to be used for high-energy applications [16]. Unlike many crystals, glasses can be doped with high concentrations of ions and still maintain good uniformity. However, glasses have inferior thermal properties that tend to cause thermal induced birefringence and optical distortion [17,18]. Moreover, glasses have a lower emission cross-section than crystals, which results in a higher lasing threshold [7].

Oxide glasses such as silicates and phosphates are the most common commercially available optical glasses. Compared with phosphate glasses, silicates have a large nonlinear coefficient and a small emission cross section. Glasses are often doped with rare earth ions such as Nd^{3+}, Er^{3+} and Yb^{3+} [19,20]. Nd-doped phosphate glasses have been used in large laser systems for fusion research [21,22]. Er-doped glasses are typically used for fiber amplifiers for optical communications [23,24]. Due to the weak pump absorption, Er:glasses are often co-doped with Yb ions to improve the system efficiency [25]. Pump radiation is first absorbed by the ytterbium ions which then transfer the energy to the erbium ions.

In short, crystalline and glass lasers are suited for different applications. Crystalline materials with high gain and superior thermal conductivity are suitable for continuous or high repetition-rate operation, whereas glasses providing broad emission bandwidths and size flexibility are ideal for high energy pulsed operation [7].

1.2 Tunable Solid-state Lasers

The discovery of the ruby laser triggered the exploration of other gain materials. An important laser material – neodymium-doped yttrium aluminate garnet (Nd:YAG) was found in 1964 by Geusic *et al.* [26]. Nd:YAG immediately replaced the application of Ruby in rangefinders, as it was shown to have superior properties over Ruby, for example, a low threshold and high efficiency. Lasers like Nd:YAG and Ruby can access only discrete wavelengths since laser transition occurs between discrete energy levels. Yet, wavelength tunability of solid-state lasers can be achieved when the emission of vibrational phonons is coupled with the stimulated emission of photons. This vibrational-electronic interaction generates vibrational sublevels in the energy bands. Laser transition can, therefore, occur over a range of energies. Such lasers are also called ‘vibronic lasers’, where the total energy of the transition is fixed but can be distributed between photons and phonons in a continuous manner [7].

A number of tunable solid-state lasers were developed between the 1860s and 1980s. The first vibronic laser – a nickel-doped magnesium fluoride (Ni:MgF_2) laser was reported by Johnson *el al.* in 1963 [27]. The same group built several other vibronic lasers based on fluoride and oxide hosts (e.g. V:MgO and V:MgF$_2$) [28]. The wavelengths of these lasers could be tuned between 1.12-2.17 μm, but they could only operate at cryogenic temperatures [7]. Johnson *el al.* later developed the first room-temperature vibronic laser based on Ho:BaY$_2$F$_8$ gain medium in 1974 [29]. In 1977, Walling *et al.* firstly demonstrated tunable laser operation of Alexandrite (Cr:BeAl$_2$O$_4$) at room temperature. Tuning over the wavelength range of 701 – 794 nm was achieved with this vibronic laser [30]. Later, the titanium-doped sapphire (Ti:Al$_2$O$_3$) laser was discovered by Moulton in 1982. It was continuously tuned from 660 to 986 nm [31]. Thereafter, Ti:sapphire lasers dominated the fields of wavelength-tunable lasers, as they have a broad tuning range, high output power and superior beam quality. Some important tunable lasers that are of interest, including Ti:sapphire, Alexandrite and Chromium-doped colquiriite lasers, will be discussed below.

Titanium Sapphire Laser

Ti^{3+} ions have a broad gain bandwidth. When doped into sapphire, they provide an exceptionally wide tuning range (660-1180 nm [31,32]) and the capability of generating femtosecond pulses (as short as 5 fs [33]). The host material – sapphire has excellent thermal conductivity, which can effectively alleviate the thermal effects of high-power operation. Ti:sapphire lasers, therefore, have become the most widely used vibronic laser. The fluorescence lifetime of Ti:sapphire is short (3.2 μs) [31], whilst the saturation power is very high. Thus, an intensely focused pump beam with high beam quality is required.

Ti:sapphire lasers are typically pumped by frequency-doubled neodymium lasers (Nd:YAG/Nd:YVO$_4$) or optically pumped semiconductor lasers. These pump sources are powerful, but make the overall system bulky, complex, and expensive, thereby limiting their use in real-world applications. The green laser diode [34] provides an alternative solution, bringing advantages in compactness and cost. As a result, systems using green laser diodes as a pump source have been demonstrated over the past few years [35,36]. However, such systems are currently constrained by the available power and price of the green diodes. Even so, diode pumping is still believed to be a promising solution, as it has the great potential to facilitate the development of simple, compact and low-cost Ti:sapphire laser systems.

Chromium-doped Lasers

Chromium-doped lasers are attractive vibronic lasers and have achieved considerable success as tunable laser sources. Cr^{3+}-doped laser materials possessing broad emission bands are capable of being tuned around 800 nm and generating femtosecond pulses. Moreover, they can be pumped with cost-efficient red diodes (AlGaInP), due to their broad absorption bands in the visible portion of the spectrum [37]. Cr^{3+}-doped lasers, like Alexandrite, Cr:LiCAF, Cr:LiSAF and Cr:LiSGaF have high intrinsic slope efficiencies (> 50%), and can lase at low thresholds with relatively high electrical-to-optical conversion efficiencies.

The Cr:LiCAF laser was found to possess a high intrinsic slope efficiency of 67% [38]. The emission wavelength can be tuned over a range of 720-871 nm [38,39]. The low stimulated emission cross-section (1.3x 10^{-20} cm^2) of Cr:LiCAF results in the low small signal gain, and thereby requiring high laser fluence and low loss optics [39]. On the other hand, Cr:LiSAF has a broader tuning range (780-1042 nm) [39,40] and a higher emission cross section (4.8x 10^{-20} cm^2 [41]) than Cr:LiCAF. However, it has an inferior thermal conductivity (3.1 $Wm^{-1}K^{-1}$) [42]. Therefore, diode-pumped Cr:LiSAF lasers suffer from thermal problems that limit the laser power level.

Additionally, Cr:LiSGaF has a tuning range from 777 to 977 nm and an intrinsic slope efficiency of 60% [39,43]. Cr:LiSGaF possesses a low melting point of 716 °C benefiting the growth of low-cost and large-scale crystals [44]. Due to the mediocre performance, Cr:LiSGaF has attracted less attention than either Cr:LiCAF or Cr:LiSAF.

Finally, Alexandrite has a tuning range from 701-858 nm and was the first tunable solid-state laser considered for practical applications [45,46]. Alexandrite's long fluorescence lifetime enables good energy storage potential for Q-switching. The high thermal conductivity allows the high-power operation of Alexandrite. It is one of the most popular tunable solid-state lasers and the focus of this thesis. Further details of Alexandrite will be presented in Chapter 3.

A comparison of spectroscopic and laser parameters of the four Cr^{3+}-doped lasers with those of Ti:sapphire is shown in Table 2. Compared to Ti:sapphire, the Cr^{3+}-doped crystals have low emission cross sections that result in smaller signal gain. Among the four Cr^{3+}-doped lasers, Alexandrite possesses the longest fluorescence lifetime and the highest thermal conductivity; Cr:LiSAF possesses the broadest tunability and the highest emission cross section; Cr:LiSGaF has the lowest melting point; Cr:LiCAF exhibits a relatively balanced performance.

Table 2. Comparison of the spectroscopic and laser parameters of the gain media (Ti:sapphire, Alexandrite, Cr:LiCAF, Cr:LiSAF and Cr:LiSGaF).

Gain Medium	Ti:sapphire	Alexandrite	Cr:LiCAF	Cr:LiSAF	Cr:LiSGaF
Tuning range (nm)	660 - 1180 [31,32]	701- 858 [45,46]	720- 871 [38,39]	780- 1042 [39,40]	777- 977 [39,43]
Intrinsic slope efficiency (%)	64 [47]	65 [48]	67 [38]	54 [39]	60 [39]
Room-temperature Fluorescence lifetime τ (μs)	3.2 [31]	260 [49]	175 [38]	67 [42]	88 [44]
Peak emission cross section σ_{em} (10^{-20} cm^2)	41 [42]	0.7 [49]	1.3 [42]	4.8 [41]	3.3 [44]
$\sigma_{em}*\tau_f$ (μs x 10^{-20} cm^2)	131	182	228	322	290
Thermal conductivity at room temperature ($Wm^{-1}K^{-1}$)	34 [42]	23 [49]	5.1 [42]	3.1 [42]	3.6 [50]
Melting point (°C)	2040 [51]	1870 [52]	804 [53]	766 [54]	716 [44]

1.3 Optical Pumping Schemes

In the development of diode-pumped solid-state lasers, a variety of optical pumping schemes have been utilized to transfer the radiation from the pump source to the laser gain medium. The pumping schemes have an immense impact on the overall efficiency of the laser system since they determine the pump distribution inside the gain medium. An appropriate pumping scheme leads to not only higher overall efficiency but also good laser beam quality. Depending on the type of the pump source and the geometry of the gain medium, the pumping schemes can be divided into three categories: end-, side-, face-pumping. The application scenarios for the three pumping geometries are discussed separately below.

1.3.1 End Pumping

End pumping is an optical pumping technique where the pump light is injected into the gain medium along the laser beam axis. The end pumping configuration is shown in Figure 1.3. The pump beam is typically circularized and focused by a lens onto the end-face of the crystal. This crystal can be a rod or a slab but is required to have enough length to absorb the pump radiation. This pumping scheme allows for good overlap of the pump beam and the fundamental laser mode, which is important for attaining a diffraction-limited beam. In addition, end pumping enables low threshold and high-power efficiency [55]. Therefore, end pumping is suitable for most diode-pumped solid-state lasers.

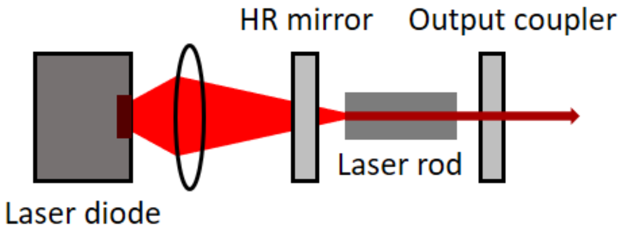

Figure 1.3. Schematic of an end-pumped solid-state laser. The laser system consists of a laser diode pump module, a pump beam focusing lens, a dichroic back mirror (highly-transmitting for the pump and highly-reflecting at laser wavelength), a laser rod, and an output coupler.

A disadvantage of the end pumping scheme is that the output power is limited by thermally induced lensing and fracturing. Since the pump beam is focused into a small area, it leads to intense thermal loads that induce thermal lensing. As the pump power increases, the thermal lensing disturbs the cavity stability and reduces the output power. In extreme cases, high pumping intensity gives rise to excess temperature differential and hence thermal fracture of the pumped crystal face. Moreover, the scheme puts constraints on the beam quality of the pump light. The end pumping scheme is, therefore, suitable for employing to achieve low or moderate output powers.

1.3.2 Side Pumping

Side pumping is another commonly used scheme for optical pumping, where the pump beam is injected into the gain medium from the side. The direction in which the pump beam is incident is perpendicular to the direction of the laser beam. Figure 1.4 shows a schematic diagram of a typical side-pumped solid-state laser.

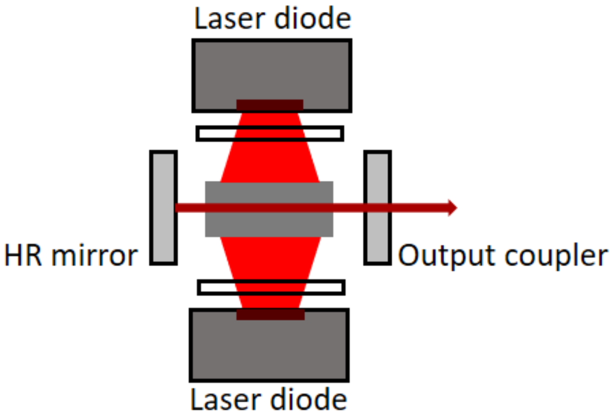

Figure 1.4. Schematic of a side-pumped solid-state laser. The laser system consists of two laser diodes (pump lasers), two vertical cylindrical lenses (shaping the pump beam in the vertical axis), an HR mirror (highly-reflecting at laser wavelength), an output coupler and a gain medium.

Side pumping has the advantage of allowing the use of pump sources with low spatial coherence. It permits a large pump area on the gain medium, which alleviates thermal loading as compared to the end pumping. Another advantage of this scheme is the power scalability. For example, multiple diode bars can be combined and placed along the length of the gain medium to provide pump radiation. The width of the emitting area can approach the crystal length. For these reasons, side pumping is often employed for high-power solid-state lasers [56,57]. However, due to the gain existing at the edge of the laser modes, the oscillation of higher-order spatial modes might occur, making it more challenging to achieve good beam quality and high efficiency.

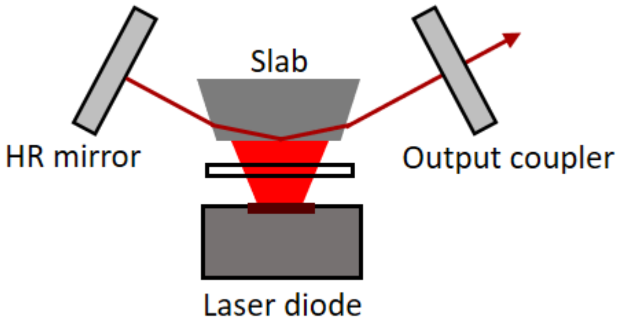

Figure 1.5. Schematic of a bounce geometry laser. The laser system consists of a laser diode, a vertical cylindrical lenses (used for pump beam shaping), an HR mirror (highly-reflecting at laser wavelength), an output coupler and a gain medium (slab).

The main reason for the inefficiency of the side pumping scheme is that the pump light is preferentially absorbed near the surface, whereas the laser mode is located inside the gain medium [58]. A special side pumping geometry worth mentioning is bounce geometry. The laser beam undergoes total internal reflection at the pump face of the crystal, as shown in Figure 1.5. This pumping scheme leads to a high inversion density located in a shallow region near the pump face and allows the laser beam to experience high gain as passing through the crystal. For gain media with strong pump absorption (e.g. Nd:YVO_4), most pump light can be absorbed within the fundamental mode to achieve excellent beam quality [59].

1.3.3 Face Pumping

Face pumping involves the use of a laser crystal that is in the form of a thin disk. Figure 1.6 illustrates the face pumping geometry of a solid-state laser. The thin disk, that is adhered to a heat sink, has a thickness considerably smaller than the laser beam diameter. The heat generated is uniformly distributed in the transverse direction and is mainly extracted through the end face attached to the heat sink. The end face is highly reflective coated for both the laser and pump wavelengths. It also acts as a folding mirror or an end mirror of the resonator. This cooling arrangement effectively reduces the transverse temperature gradient, which results in high beam quality [60]. The heat dissipation from the thin disk to the heat sink is highly efficient, and this allows high pump power densities without causing overheating of the crystal [61].

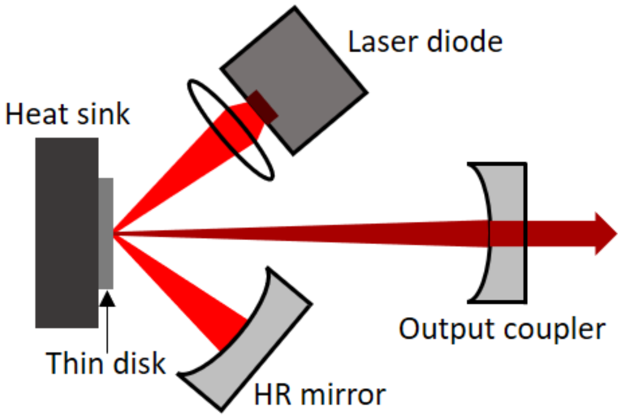

Figure 1.6. Schematic diagram of a face-pumped solid-state laser. The laser system consists of a laser diode, a focusing lens, an HR mirror, an output coupler and a thin disk (laser gain medium) adhered to a heat sink.

Due to the small thickness, the thin disk exhibits low pump absorption when only a single or double pass of the pump beam is used. This problem is solved using a multi-pass geometry, which easily allows for multiple pump beam passes (e.g. 16 or 24 passes [62,63]). A significant advantage of the face-pumped thin-disk geometry is power scalability. This is achieved by simultaneously increasing the pump power and area. The simple scaling law allows a variety of solid-state lasers operated at extremely high power (up to tens of kilowatts) [60]. Therefore, the thin-disk laser design has the potential to produce high output power, high efficiency and excellent beam quality.

1.4 Thesis Overview

As stated at the beginning, this thesis is concerned with the development of diode-pumped solid-state lasers based on Alexandrite crystals that produce broadly tunable wavelengths with high efficiency. The capability for direct diode pumping enables the construction of simple, compact and cost-efficient Alexandrite lasers that operate with high efficiency.

In Chapter 2, the theory of optical resonators applicable to solid-state lasers is introduced. More specifically, the requirements of stable optical resonators are shown. The formation and influence of thermal lensing are presented. In addition, laser modes are discussed, along with the experimental techniques for analyzing them. Theoretical background concerning with the behaviour of continuous-wave (CW) and Q-switched lasers are presented in the latter part. Idealized models are employed to introduce the mechanism of laser action. For CW operation, the expression for the output power and the optimum output coupling of laser oscillators are derived through theoretical analysis. Several practical methods for realizing single-mode operation are discussed in detail. Finally, the theory of Q-switching and typical methods of implementing Q-switched operation are discussed.

In Chapter 3, the physical and spectroscopic properties of Alexandrite relevant to the laser performance are presented. The physical properties of Alexandrite are compared with other common crystals, which proves that Alexandrite is superior for same applications among the possible choices of laser crystals. Laser kinetics for Alexandrite operated as either a 3-level or a 4-level system are discussed, along with the temperature-dependent characteristics. The spectral properties, as well as the wavelength tuning limits, are explained via combining absorption and emission processes. Diverse pump source options and the versatility of the Alexandrite lasers allow for a wide range of applications.

The remainder of this thesis is focused on experimental demonstrations and investigations of Alexandrite's diode-pumped laser performance. Chapter 4 presents the results from diode-end-pumped actively Q-switched Alexandrite lasers. The two laser-diode modules (a free-space laser module and a fiber-coupled one) used as pump lasers in the thesis work are introduced. The free-space laser module possessing nearly linearly polarised output and high output power (>60 W) was used as the pump source for actively Q-switched operation. The Q-switching was achieved via loss modulation, through the use of a BBO Pockels cell. Short pulses with repetition rates up to 10 kHz were demonstrated from the Q-switched laser. To obtain shorter pulses with higher peak power, a cavity-dumped Q-switched system was developed by modifying the already Q-switched laser system.

In Chapter 5, a wavelength-tunable passively Q-switched diode-pumped Alexandrite laser is investigated. A fiber-coupled red-diode module was employed to provide optical pumping due to its relatively favourable beam quality. The passively Q-switched operation was realized using a semiconductor saturable absorber mirror (SESAM), and the wavelength tuning was demonstrated using a birefringent plate. The laser design uses a Brewster-angle cut crystal and curved mirrors, which introduce astigmatism. The astigmatic properties of these elements are analyzed, and a compensation scheme is proposed and implemented. The results of the passively Q-switched laser using an X-shaped cavity design for astigmatic compensation are presented at the end of this chapter.

Chapter 6 presents the first unidirectional single-longitudinal-mode (SLM) operation of a CW diode-pumped Alexandrite ring laser with wavelength tunability. Based on the X-shaped cavity design of the passively Q-switched system described in Chapter 5, an enhanced design was developed as a precursor to the ring cavity. This enhanced X-shaped cavity design primarily includes the replacement of previously used plano-concave cavity mirrors with a pair of customized convex-concave mirrors (also known as ‘zero lens’ mirrors). The influence of the two types of mirrors on the pump light is quantitatively simulated and compared. The result shows that the ‘zero lens’ mirror has an insignificant impact on the pump light as compared to the plano-concave mirror. Moreover, the use of ‘zero lens’ mirrors with a short radius of curvature allowed a novel ‘displaced mode’ cavity design, which ensures the compactness of the laser system. The unidirectional SLM operation was implemented using an optical diode. The results open the way for the development of cost-effective and compact laser systems with high power, narrow linewidth and precise wavelength tunability.

Chapter 7 summarizes the main results of each chapter, along with a few ideas for further improvement. The significance of this thesis work is also highlighted at the end.

Chapter 2

Laser Theory

This chapter deals with the theory of optical cavities that is applicable to solid-state lasers. The requirements of a stable cavity are mathematically deduced, and the impact of thermal lensing is qualitatively discussed. The modes of a laser cavity are shown, along with experimental techniques to analyse them.

The theoretical background required to describe the continuous wave and Q-switching laser behavior was developed in the latter part of this chapter. Idealized models are employed to explain the operation of optically pumped solid-state lasers. Optimum output coupling of laser oscillators is presented, along with practical methods for single mode selection. Typical methods of realizing Q-switching are also discussed in detail.

2.1 Laser Cavity Stability and Modes

Optical cavities, which in most cases consist of two or more mirrors are a major component of lasers. The concept of cavity stability can be comprehended from a purely geometrical picture of how paraxial rays propagate around a laser cavity. For such a cavity, the multiple propagations of light rays can be analyzed using the matrix formulation of geometrical optics under the paraxial approximation.

In this section, the theory of optical cavities without active media is presented, and the stability criterion for a typical two-mirror system with/without an intracavity lens is derived using ray transfer matrix analysis. The optical pumping process is associated with heat generation in solid-state lasers. Since thermal lensing may affect the stability of the laser systems, a deep understanding of this effect is vitally important. The origin of the thermal lensing and its impact on laser systems are discussed here. The output beams of laser cavities are shown in terms of cavity modes, which characterize spatial and frequency properties of laser output. Experimental techniques to analyse cavity modes are also demonstrated in this section.

2.1.1 Cavity Stability

The ray transfer matrix approach is a type of ray tracing technique used to propagate rays through optical systems. A ray transfer matrix can be used to describe an optical element's effect on a laser beam. Figure 2.1 shows the propagation of a ray through a general optical element in cylindrical geometry.

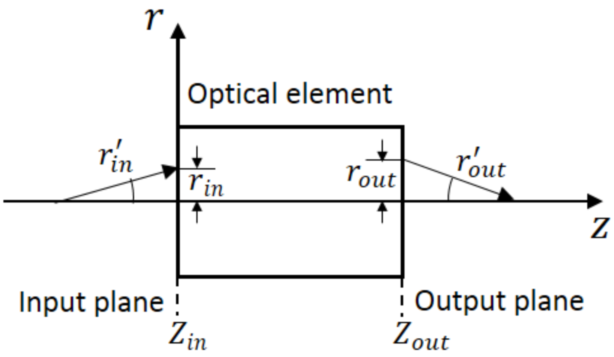

Figure 2.1. Propagation of a ray through a general optical element. Z_{in} and Z_{out} define input and output planes, respectively. The ray at the input plane is characterized by radial displacement (r_{in}) and angular displacement (r'_{in}). Similarly, the ray at the output plane is represented by (r_{out}, r'_{out}).

The ray at the input plane is characterized by two parameters - radial displacement (r_{in}) and angular displacement (r'_{in}). Similarly, the ray at the output plane is represented by (r_{out}, r'_{out}). Each optical element transforms the ray according to

$$\begin{vmatrix} r_{out} \\ r'_{out} \end{vmatrix} = \begin{vmatrix} A^* & B^* \\ C^* & D^* \end{vmatrix} \begin{vmatrix} r_{in} \\ r'_{in} \end{vmatrix} \tag{2.1.1}$$

where the $A^*B^*C^*D^*$ matrix is a transfer matrix that is characteristic to the specific optical element intersected by the ray. It should be noted that the ray transfer matrix analysis is only valid under the Paraxial Approximation. Thus, the angular displacements must stay small to enable this approximation.

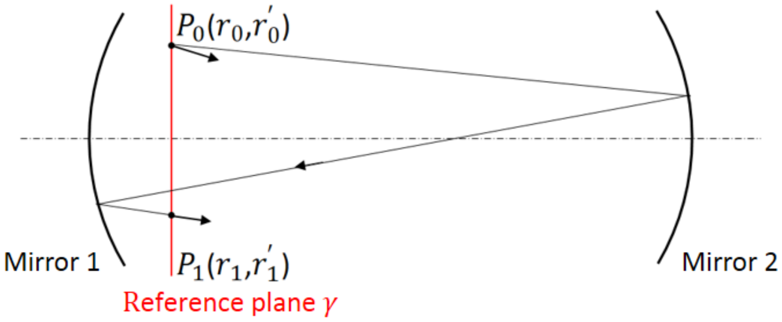

Figure 2.2. A general two-mirror laser cavity. The cavity consists of two mirrors (Mirror 1 and 2). γ defines a reference plane inside the cavity. An intracavity ray intersects the reference plan γ at $P_0(r_0, r_0')$ and $P_1(r_1, r_1')$.

For a generic two-mirror cavity with no limiting aperture shown in Figure 2.2, there is a ray leaving point $P_0(r_0, r_0')$ of a reference plane γ and propagating to the right. After reflection from mirrors 2 and 1, the ray will intersect the reference plane at point $P_1(r_1, r_1')$. This process can be described with the ray transfer matrix by considering the entire laser cavity as an optical element. According to Equation (2.1.1), the radial and angular displacements of the ray at point P_1 are given by

$$\begin{vmatrix} r_1 \\ r_1' \end{vmatrix} = \begin{vmatrix} A & B \\ C & D \end{vmatrix} \begin{vmatrix} r_0 \\ r_0' \end{vmatrix} \tag{2.1.2}$$

where the $ABCD$ matrix is the cavity round trip matrix [11].

In the case of a resonator which consists of two curved mirrors M$_1$ and M$_2$ with radii of curvature R_1 and R_2 and spacing L, the corresponding $ABCD$ matrix can be obtained from the product of matrices of the individual optical elements. Thus, the cavity round trip matrix of this two-mirror resonator is given by

$$\begin{vmatrix} A & B \\ C & D \end{vmatrix} = \begin{vmatrix} 1 & 0 \\ -2/R_1 & 1 \end{vmatrix} \begin{vmatrix} 1 & L \\ 0 & 1 \end{vmatrix} \begin{vmatrix} 1 & 0 \\ -2/R_2 & 1 \end{vmatrix} \begin{vmatrix} 1 & L \\ 0 & 1 \end{vmatrix} \tag{2.1.3}$$

If the wavefront curvature of the Gaussian beam matches the mirror curvature at each mirror, the optical resonator can support both the lowest-order Gaussian mode and higher-order Hermite-Gaussian or Laguerre-Gaussian modes.

The complex beam parameter denoted by q is used to specify the properties of the Gaussian beam. The q parameter of a beam is defined as

$$\frac{1}{q}=\frac{1}{R}-i\frac{M^2\lambda}{\pi w^2} \tag{2.1.4}$$

where R is the radius of curvature, M^2 is the beam quality factor, λ is the wavelength of the beam, w is the waist size of the beam. If a Gaussian beam is a mode of an optical cavity, the beam must reproduce itself and its q parameter must be unchanged after one round trip. According to the $ABCD$ law of Gaussian beam [64], the requirement is given by

$$q_1=\frac{Aq_0+B}{Cq_0+D}=q_0 \tag{2.1.5}$$

where q_0 and q_1 are the complex beam parameters at the reference plane γ. A, B, C and D are the components of the cavity round trip matrix given by Equation (2.1.3). According to Equation (2.1.5), the complex beam parameter q_0 must satisfy the following equation

$$C{q_0}^2-(A-D)q_0-B=0 \tag{2.1.6}$$

The solution of the above quadratic equation is given by

$$q_0=\frac{(A-D)\pm\sqrt{(A+D)^2-4(AD-BC)}}{2C} \tag{2.1.7}$$

where $(AD-BC)$ is the determinant of the $ABCD$ matrix. The determinant of a product of square matrices is the product of the determinants of elementary matrices, and each of the elementary matrices has unity determinant, so $AD-BC=1$. Because the q parameter (q_0) always has an imaginary part, the expression under the square root in Equation (2.1.7) has to be negative, which gives

$$\frac{1}{4}(A+D)^2 < 1 \tag{2.1.8}$$

Equation (2.1.8) is the stability condition for the two-mirror resonator, which means a Gaussian beam can only be sustained by stable resonators. This condition can also be written as

$$0 < \frac{1}{4}(A+D+2) < 1 \tag{2.1.9}$$

From the cavity round trip matrix (Equation (2.1.3)), the stability condition (Equation (2.1.9)) can be expressed as

$$0 < \left(1-\frac{L}{R_1}\right)\left(1-\frac{L}{R_2}\right) < 1 \tag{2.1.10}$$

It is customary to introduce the g parameters of the cavity. The parameters are defined as

$$g_1 = 1-\frac{L}{R_1} \quad \text{and} \quad g_2 = 1-\frac{L}{R_2} \tag{2.1.11}$$

With Equation (2.1.11), the stability condition of Equation (2.1.10) transforms to a simple relation given by [65]

$$0 < g_1\, g_2 < 1 \tag{2.1.12}$$

The stability condition can then be conveniently translated into the cavity stability diagram shown in Figure 2.3.

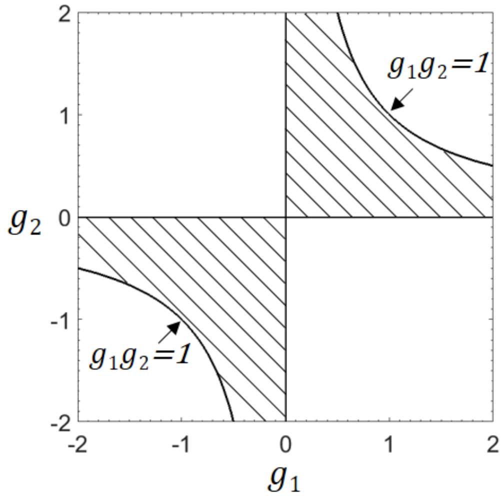

Figure 2.3. Stability diagram for a two-mirror optical resonator. The shaded area corresponds to the stable region.

The hyperbola in the diagram corresponds to the boundary condition of $g_1g_2 = 1$. The other boundary condition $g_1g_2 = 0$ (either $g_1 = 0$ or $g_2 = 0$) is automatically represented by the horizontal and vertical axes. The shaded area enclosed by these boundaries corresponds to the stable region. Every two-mirror optical resonator can be represented by a point (g_1, g_2) on the stability diagram. Resonators will be marginally stable if the point (g_1, g_2) lies on the boundary lines. If the point (g_1, g_2) falls in the unstable region outside the shaded area, the two mirrors will form an unstable optical resonator.

Practically, laser resonators are often used with internal lenses for mode control. Interestingly, the gain medium itself can act as an intracavity lens due to thermal lensing. Therefore, the majority of laser cavities investigated in this work can be approximated to follow the design shown in Figure 2.4. This cavity consists of two curved mirrors M_1^* and M_2^* with radii of curvature R_1^* and R_2^* and an intracavity lens of focal length f. The lens is spaced a distance L_1 away from M_1^* and L_2 away from M_2^*.

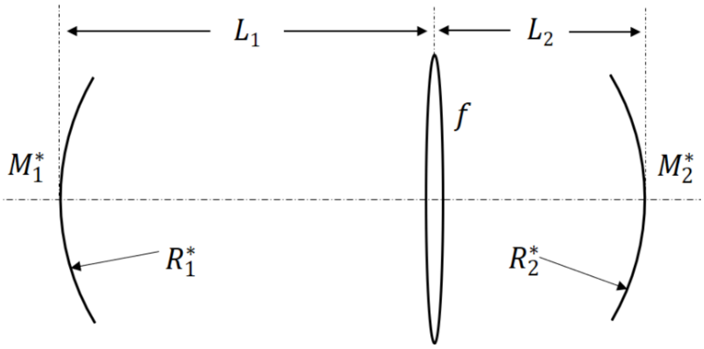

Figure 2.4. Two-mirror laser resonator with an internal lens of focal length f. The radii of curvature of mirrors are R_1^* and R_2^*. The distances between the mirrors and the lens are L_1 and L_2.

The g parameters of this optical resonator are given by

$$g_1^* = 1 - \frac{L_2}{f} - \frac{L'}{R_1^*} \text{ and } g_2^* = 1 - \frac{L_1}{f} - \frac{L'}{R_2^*} \tag{2.1.13}$$

Where $L' = L_1 + L_2 - L_1 L_2 / f$ is an effective length used to simplify the equations. The stability condition for this case is consistent with that for a two-mirror resonator, and given by

$$0 < g_1^* \, g_2^* < 1 \tag{2.1.14}$$

The beam radii on the resonator mirrors (w_1 & w_2) are given by [64,66]

$$w_1 = \sqrt{\frac{\lambda|L'|}{\pi}} \left[\frac{g_2^*}{g_1^*(1 - g_1^* g_2^*)}\right]^{1/4} \tag{2.1.15}$$

$$w_2 = \sqrt{\frac{\lambda|L'|}{\pi}} \left[\frac{g_1^*}{g_2^*(1 - g_1^* g_2^*)}\right]^{1/4} \tag{2.1.16}$$

where λ is the laser wavelength. The beam radius is defined as the distance from the beam axis to where the optical intensity drops to $1/e^2$ of the value on the beam axis ($1/e^2$ intensity). The beam radius on the lens (w_3) can be obtained by propagating the Gaussian beam from M_1^* (or M_2^*) for a distance L_1 (or L_2), which gives

$$w_3 = \sqrt{\frac{\lambda}{\pi}}\left[\frac{4u_1u_2 g_1^* g_2^* + (u_1 - u_2)^2}{g_1^* g_2^* (1 - g_1^* g_2^*)}\right]^{1/4} \tag{2.1.17}$$

where $u_1 = L_1(1 - L_1/R_1^*)$ and $u_2 = L_2(1 - L_2/R_2^*)$ are two variables introduced for simplifying the analysis [67].

2.1.2 Thermal Lensing

For most solid-state lasers, the pump wavelength is shorter than the laser wavelength, which means the energy of pump photons is larger than that of laser photons. The so-called quantum defect is defined as the energy difference between pump and laser photons. The energy difference (ΔE) is expressed as

$$\Delta E = h\nu_{\text{pump}} - h\nu_{\text{laser}} = h\nu_{\text{pump}}\left(1 - \frac{\lambda_{\text{pump}}}{\lambda_{\text{laser}}}\right) \tag{2.1.18}$$

During the pumping process, this difference in energy (ΔE) is lost and released as heat in the gain medium [68]. The quantum defect causes inevitable energy loss and sets an upper limit on the power efficiency.

The quantum defect heating is the main origin of heat generation in solid-state lasers. In addition, there are many other mechanisms (e.g. excited-state absorption and up-conversion) which can also lead to heat generation. The heat generated in the gain medium results in the thermal lensing effect. To explain this, it should first be noted that the refractive index of a gain medium is temperature-dependent, which is quantified with the thermo-optic coefficient (dn/dT). The gain medium is hotter on the beam axis as compared to the outer region, which gives rise to some transverse gradients of the refractive index and thus a lensing effect. The temperature gradients generate mechanical stresses in the gain medium. The stresses lead to further refractive index changes via the photo-elastic effect, which results in additional lensing effect. Thermally induced stresses can also lead to the deformation of the end faces of the gain medium. In an end-pumping configuration, this effect turns the crystal into a thick lens due to differential expansion [69].

In the case of end-pumped lasers with rods of cylindrical symmetry, the combined effects of the temperature- and stress-dependent variation of the refractive index and the deformation of the end faces give the expression for the focal length of the thermal lens [7]

$$f = \frac{K_C A}{P_h}\left(\frac{1}{2}\frac{dn}{dT} + n_0^3 \alpha C_{r,\phi} + \frac{\alpha r_0 (n_0 - 1)}{l}\right)^{-1} \tag{2.1.19}$$

where K_C is the thermal conductivity of the gain medium, A is the pumped area, P_h is the total heat power dissipated in the rod which is proportional to the absorbed pump power, n_0 is the refractive index at the center of the rod, α is the thermal expansion coefficient, $C_{r,\phi}$ is the photo-elastic coefficient, r_0 is the radius of the rod and l is the length of the rod. The first term on the right side of Equation (2.1.19) corresponds to thermal lensing caused by the temperature variation, the second item denotes the stress-dependent effect, and the last term is due to the deformation of the pump face. Hence, the dioptric power $(1/f)$ of the thermal lens induced by temperature gradients and stresses can be numerically analyzed using this equation.

Thermal lensing leads to the degradation of both laser beam quality and output power. In extreme cases, stress fracture could occur if the thermally induced stress exceeds the ultimate tensile strength of the gain medium. Obviously, the presence of thermal lensing poses challenges to the cavity design. In principle, thermal lensing can be compensated by adjustments of the laser system design. Therefore, it is necessary to analyze a number of factors including the pumping geometry, the heat-sinking arrangement, and the properties of the gain medium [70].

2.1.3 Cavity Modes

A mode of a resonator is defined as a self-consistent distribution of the electromagnetic field. The field distribution reproduces itself after one round trip. Stable modes of oscillation can be sustained, and their transverse intensity profile and phase must be unchanged after multiple traverses in the resonator. Laser modes are typically divided into two categories: transverse modes and longitudinal modes.

Transverse Modes

Transverse modes are found through solving the paraxial wave equation with spherical cavity boundaries. The Solutions in rectangular coordinates give the Hermite-Gaussian modes. Within the paraxial approximation, the electric and magnetic fields of the modes are approximately transverse to the propagation direction, so they are designated TEM_{mn} (Transverse Electric Magnetic). The indices m and n refer to the form of the transverse field distribution.

The lowest order mode (TEM_{00}) is the fundamental transverse mode of the resonator and has circular symmetry. The field distribution is defined by a Gaussian function. The width of the Gaussian mode changes as the beam propagates along its axis. All other modes with more complicated intensity distributions are termed higher-order transverse modes and have symmetry in Cartesian coordinates. Their electric field distributions are described by the product of Hermite and Gaussian functions and given by

$$E_{mn}(x,y,z) = \frac{w_0}{w(z)} H_m\left(\frac{\sqrt{2}x}{w(z)}\right) H_n\left(\frac{\sqrt{2}y}{w(z)}\right) exp\left(-\frac{(x^2+y^2)}{w(z)^2} - \frac{ik(x^2+y^2)}{2R(z)} - i[kz-(1+m+n)\phi(z)]\right) \tag{2.1.20}$$

where $H_m(p)$ is the Hermite polynomial with non-negative integer index m. The indices m and n are the transverse mode numbers and determine the shape of the profile in the x and y direction respectively. $k = 2\pi/\lambda$ is the wavenumber, and w_0 is the radius of the beam waist (at $1/e^2$ intensity cut-off). $w(z)$, $R(z)$ and $\phi(z)$ are the beam radius, radius of curvature and Gouy phase shift, respectively. These parameters evolve in the z direction just as for a Gaussian beam, and their expressions are

$$w(z) = w_0\sqrt{1+(z/z_R)^2} \tag{2.1.21}$$

$$R(z) = z + {z_R}^2/z \tag{2.1.22}$$

$$\phi(z) = \tan^{-1}(z/z_R) \tag{2.1.23}$$

where $z_R = \pi {w_0}^2/\lambda$ is the Rayleigh range. The cross-sectional intensity profiles of the Hermite-Gaussian modes are shown in Figure 2.5. It can be seen that the mode numbers also indicate the number of zero fields in the corresponding axis [11,65].

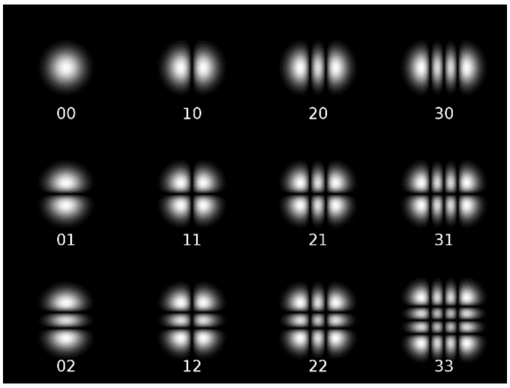

Figure 2.5. Intensity profiles of the Hermite-Gaussian modes (TEMmn modes). Starting with TEM_{00} (upper left-hand side) and going up to TEM_{33} (low right-hand side). All profiles generated with Matlab.

For $m = n = 0$, Equation (2.1.20) reduces to the Gaussian solution as the Hermite polynomial of zeroth order is a constant. The Gaussian beam (fundamental transverse mode) with a circularly-symmetric spatial profile is the preferred output from a laser cavity since it can be focused down to a very small spot size to achieve a high-power density.

It is worthwhile to mention that the electric field distributions of the Hermite-Gaussian modes form a set of functions which are complete and mutually orthogonal, so every arbitrary field distribution can be decomposed using Hermite-Gaussian modes.

Longitudinal Modes

A longitudinal mode is a standing wave pattern formed by waves confined in a cavity. The cavity not only give rise to a transverse mode structure but also imposes a mode structure on the longitudinal frequencies. The frequencies have a dependence on the transverse modes because of different phase shifts for different order modes. In fact, transverse and longitudinal modes can be viewed as different facets of an electric field distribution.

According to Equation (2.1.20) and (2.1.23), the phase of the field for an mn-th order Hermite-Gaussian mode is given by

$$\Phi(z) = kz - (1 + m + n)\tan^{-1}(z/z_R) \qquad (2.1.24)$$

The condition for a resonator mode requires the field distribution to be self-reproducing, which implies the phase can only change by an integer multiple of 2π after one round trip, or the one-way phase shift must be an integer multiple of π. Therefore, the phase shift from one end of cavity to the other is given by

$$k(z_2 - z_1) - (1 + m + n)[tan^{-1}(z_2/z_R) - tan^{-1}(z_1/z_R)] = \pi q \qquad (2.1.25)$$

where q is an integer and represents the longitudinal mode number. It has been shown that the Guoy phase shift (the expression in the square brackets) is equivalent to $\cos^{-1}(\pm\sqrt{g_1 g_2})$ [71]. Writing the frequency of the mode as $\nu_{mnq} = c/\lambda$ and using Equation (2.1.25), the frequencies of the allowed modes are given by

$$\nu_{mnq} = \frac{c}{2L}\left(q + \frac{1}{\pi}(1 + m + n)\cos^{-1}(\pm\sqrt{g_1 g_2})\right) \qquad (2.1.26)$$

where $L = (z_2 - z_1)$ is the optical path length, and the g parameters of the cavity are defined by Equation (2.1.11). The positive sign is for the point (g_1, g_2) in the positive quadrant of the stability diagram, while the negative sign is for the point in the negative quadrant.

2.1.4 Mode Analysis

In general, laser applications require specific laser modes. Therefore, the analysis of the laser modes is of practical significance. Diagnostic techniques are needed to analyse transverse and longitudinal modes. The measurement and characterization of the transverse mode profiles are usually discussed using a single parameter – beam quality factor (or M^2 factor). The observation and analysis of the longitudinal modes are performed using a Fabry–Pérot interferometer.

Beam Quality Measurement

The M^2 factor is a parameter introduced to quantify the beam quality of laser beams. It is defined as the ratio of the beam parameter product (BPP) of the measured beam to that of a diffraction limited Gaussian beam with the same wavelength. The BPP is the product of a laser beam's divergence angle and the radius of the beam waist. The definition of M^2 is thus given by

$$M^2 = \frac{w\theta}{w_0\theta_0} = \frac{\pi w\theta}{\lambda} \tag{2.1.27}$$

where w is the radius at the beam waist, θ is the beam's divergence angle, w_0 and θ_0 are the beam waist radius and beam's divergence angle of an ideal Gaussian beam, λ is the wavelength. Therefore, the parameter M^2 indicates the degree of variation of a beam from an ideal Gaussian beam which has an M^2 factor of 1. For a real laser beam, M^2 is greater than 1.

According to ISO 11146 standards, the M^2 factor can be obtained from the evolution of the beamwidth along the propagation direction (z). The beamwidth is defined based on second-order moments of the intensity distribution $I(x, y)$. The second-moment beam radius in the x-direction is defined as

$$W_x = 2\sqrt{\frac{\iint (x-\bar{x})^2\, I(x,y)\, dxdy}{\iint I(x,y)\, dxdy}} \tag{2.1.28}$$

where $\bar{x}$ is the centroid coordinates of the intensity distribution. The beam radius W_y in the y direction can be defined in a similar manner by replacing $(x-\bar{x})^2$ with $(y-\bar{y})^2$ in the upper integral. This way of defining the beamwidth is also known as D4σ method, as the beam diameter is 4 times the standard deviation of the intensity distribution. For an ideal Gaussian beam (TEM_{00} mode), the second-moment beam radius W_x is consistent with the Gaussian beam radius $w(z)$ defined in Section 2.1.2. The second-moment beam radius propagates in free space in the same way as the ideal Gaussian beam spot size, so the second-moment radii for an arbitrary beam are given by

$$W_x(z) = W_{0x}\sqrt{1 + \left(\frac{M_x^2 \lambda (z - z_{0x})}{\pi W_{0x}}\right)^2} \tag{2.1.29}$$

and

$$W_y(z) = W_{0y}\sqrt{1 + \left(\frac{M_y^2 \lambda \left(z - z_{0y}\right)}{\pi W_{0y}}\right)^2} \tag{2.1.30}$$

where M_x^2 and M_y^2 are the beam quality factor in the x & y directions, W_{0x} and W_{0y} are second-moment radii of the beam waist, z_{0x} and z_{0y} are the locations of the beam waist along the z-axis in the respective directions.

To determine the M^2 factor, the second-moment beam radius is measured at multiple transverse planes along the beam propagation axis. Using Equation (2.1.29) and (2.1.30), a fitting algorithm is applied to determine M_x^2 and M_y^2 if the wavelength is known. In an actual measurement, a laser beam is normally focused with a lens of known focal length fixed in position, as shown in Figure 2.6. A CCD or CMOS camera in conjunction with a translation stage is used to record the beam's two-dimensional intensity profile and hence measuring the characteristics of the beam.

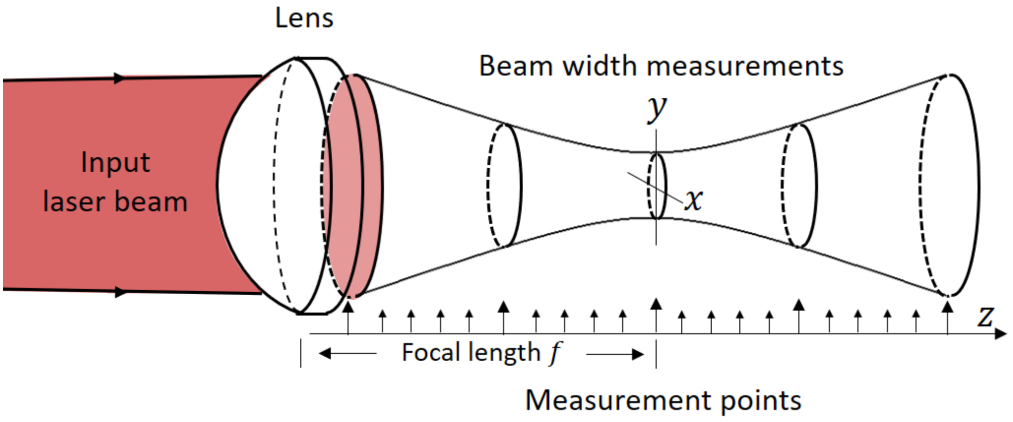

Figure 2.6. Characteristics of a laser beam as it passes through a converging lens. Multiple beamwidth measurements are taken in the near field and far field.

A Hermite-Gaussian beam related to a TEM$_{mn}$ mode has an M^2 factor of $(2m + 1)$ in the x direction and $(2n + 1)$ in the y direction. In practice, a laser oscillates on a mixture of transverse modes rather than a pure mode. For an incoherent superposition of the lowest and higher-order Hermite-Gaussian modes, the beam quality factor is given by a weighted sum of all the modes present, hence

$$M_x^2 = \sum_{m,n} |P_{mn}|^2 \times (2m+1) \tag{2.1.31}$$

$$M_y^2 = \sum_{m,n} |P_{mn}|^2 \times (2n+1) \tag{2.1.32}$$

where $|P_{mn}|^2$ is a normalized power coefficient for a Hermite-Gaussian mode TEM_{mn}. Therefore, the value of the beam quality factor depends on the distribution of the total power over transverse modes [72]. The M^2 factor quantifies the beam quality with a single number and predicts the evolution of the beamwidth. However, this single number alone cannot be considered as a complete characterization of beam quality, as there are different combinations of modes that could result in the same M^2 factor.

Frequency Measurement

Commercial spectrometers with nanometer accuracy are not suitable for resolving fine spectral features of lasers due to their resolution limitations. Instead, a Fabry–Pérot (FP) interferometer can be used as a spectrum analyser to resolve the fine structure of longitudinal modes. A FP interferometer is typically made of a plane-parallel transparent plate with two surfaces of high reflectivity R. The transparent plate has a thickness of d and a refractive index of n'. If a beam of light is incident on the FP interferometer at an angle of θ. The transmission T_{FP} of the FP interferometer is given by

$$T_{FP} = \frac{1}{1 + 4R/(1-R)^2 * \sin^2(2\pi\nu n' d \cos\theta / c)} \tag{2.1.33}$$

where ν is the frequency of the incident beam [11]. The transmission achieves its maximum value (100%) when $2\pi\nu n' d \cos\theta / c = l\pi$, where l is a positive integer and represents the interference fringe order. The frequencies of these maxima are thus given by

$$\nu = \frac{lc}{2n'd\cos\theta} \tag{2.1.34}$$

The free spectral range of the interferometer is defined as the frequency shift between adjacent order of fringes. The value is hence given by the frequency difference between two consecutive maxima. From Equation (2.1.34), the free spectral range $\Delta\nu_{fsr}$ can be written as

$$\Delta\nu_{fsr} = \frac{c}{2n'dcos\theta} \tag{2.1.35}$$

The width (FWHM) of a transmission peak can be obtained by calculating the frequency difference between two 'half-intensity ($T_{FP} = 1/2$)' points. According to Equation (2.1.33), the width $\Delta\nu_c$ is given by

$$\Delta\nu_c = \frac{c}{2n'd\cos\theta}\frac{1-R}{\pi\sqrt{R}} \tag{2.1.36}$$

The finesse of the interferometer is defined as the ratio of the free-spectral range $\Delta\nu_{fsr}$ to the width $\Delta\nu_c$. With the help of Equation (2.1.35) and (2.1.36), the expression of the finesse (F) is written as

$$F = \frac{\Delta\nu_{fsr}}{\Delta\nu_c} = \frac{\pi\sqrt{R}}{1-R} \tag{2.1.37}$$

The finesse intuitively depends on the reflectivity of the mirrors and is used to specify the resolving power of the interferometer. A high finesse gives a high spectral resolution. $\Delta\nu_c$ is considered as the minimum frequency interval that can be resolved by the interferometer. The resolution of a FP interferometer is typically in the range of tens to hundreds of MHz.

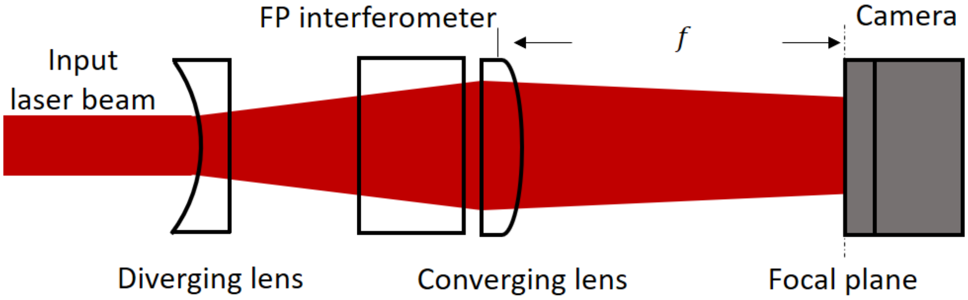

Figure 2.7. Schematic of the experimental apparatus for longitudinal frequency measurement including a FP interferometer, a diverging lens, a converging lens and a Camera.

To observe several orders of interference fringes, the output beam of a laser is diverged and propagated into a Fabry–Pérot interferometer with a negative lens, as shown in Figure 2.7. This will give a range of incident angles θ and therefore a range of orders l. The beam passing through the interferometer is then focussed by a converging lens, the interference fringes could be observed at the focal plane of the lens using a camera. The interference pattern takes the appearance of a set of concentric rings. The longitudinal mode separation $\Delta\nu_q$ can be measured using the diameters (D) of the circular fringes according to [73]

$$\Delta\nu_q = \nu_{q+1} - \nu_q = \Delta\nu_{fsr}\left(\frac{D^2_{(q+1)l} - D^2_{ql}}{D^2_{q(l-1)} - D^2_{ql}}\right) \tag{2.1.38}$$

where ν_{q+1} and ν_q represent frequencies of two adjacent longitudinal modes, while l and $l-1$ refer to two adjacent orders of interference, for example, D^2_{ql} is the diameter squared of the lth order fringe formed by the longitudinal mode ν_q. The longitudinal mode separation of a laser beam can be measured using a Fabry–Pérot interferometer with an appropriate resolution. This technique provides an efficient way of analysing the longitudinal frequency structure.

2.2 Continuous Wave Laser

Optical amplification in laser media arises from stimulated emission, where the input signal induces transitions of laser-active ions from an upper laser level to a lower laser level. In this section, theoretical background required to describe the continuous wave (CW) laser behaviour is developed, and idealized models are used to introduce the underlying mechanism of the lasing action. An expression for the output power at optimum coupling is obtained through theoretical analysis. Methods for constraining a laser to oscillate on a single transverse and/or longitudinal mode are also discussed in detail.

2.2.1 Three- and Four-level Lasers

Lasers are usually classified into two broad categories – ‘three level’ or ‘four level’ lasers. Figure 2.8 shows an idealized model of a four-level laser. One main feature of this laser is that the energy separation between the lower laser level (level 1) and the ground state (level 0) is large enough at the laser operating temperature, $E_1 \gg KT$. This guarantees that the thermal equilibrium population of the lower laser level is negligible. If the lifetime of atoms in the lower laser level is shorter than that in the upper laser level (level 2), the population density of level 1 (N_1) can be neglected compared to that of level 2 (N_2). The threshold condition is satisfied by pumping when

$$N_2 \approx N_t \tag{2.2.1}$$

Therefore, the laser starts to oscillate when the population density of level 2 reaches the threshold value N_t.

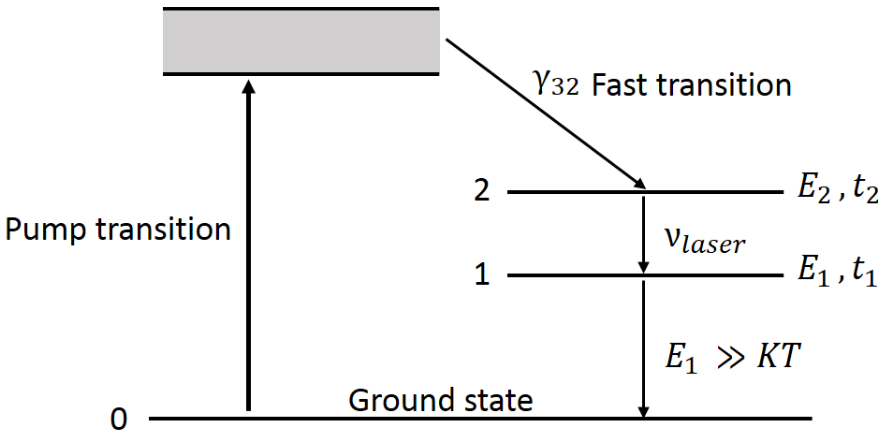

Figure 2.8. Energy level diagram of a four-level laser.

Figure 2.9 shows an idealized model of a three-level laser. The lower laser level for a three-level laser is either the ground state or a level which has a small energy difference to the ground state $E_1 < KT$. Therefore, the majority of the total population occupies the lower laser level at thermal equilibrium.

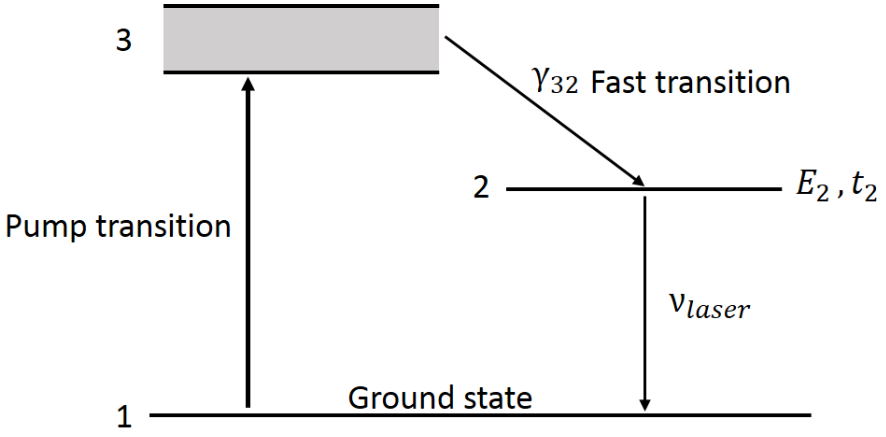

Figure 2.9. Energy level diagram of a three-level laser.

To meet the oscillation condition, the pump rate needs to be increased until the population density of the upper and lower laser levels satisfies the following conditions

$$N_2 = \frac{N_0}{2} + \frac{N_t}{2} \tag{2.2.2}$$

$$N_1 = \frac{N_0}{2} - \frac{N_t}{2} \tag{2.2.3}$$

Where $N_0 = N_1 + N_2, N_0$ is the density of the active atoms. We therefore have $N_2 - N_1 = N_t$. In most laser systems $N_0 \gg N_t$, it is found that the pump rate at threshold of a three-level laser is much higher than that of a four-level laser by comparing Equation (2.2.1) with (2.2.2). The ratio is given by

$$\frac{N_{2\,(3-level)}}{N_{2\,(4-level)}} \sim \frac{N_0}{2N_t} \tag{2.2.4}$$

Therefore, approximately N_t atoms need to be maintained in the upper laser level for a four-level laser, which corresponds to a minimum expenditure power of

$$p_{s(4-level)} = \frac{N_t V h v}{t_2} \tag{2.2.5}$$

For a three-level, the power is given by

$$p_{s(3-level)} = \frac{N_0 V h v}{2t_2} \tag{2.2.6}$$

Where V is the volume, h is the Planck constant, v is the photon's frequency, and hv represents the photon energy per transition.

2.2.2 Power in Laser Oscillator

In the case of an ideal four-level laser as shown in Figure 2.8, the population of level 1 is neglected as $E_1 \gg KT$.

The rate equations that describe the population of all levels are given by

$$\frac{dN_3}{dt} = P_{03}N_0 - \gamma_{32}N_3 \tag{2.2.7}$$

$$\frac{dN_2}{dt} = \gamma_{32}N_3 - w_{st}(v)(N_2 - N_1) - \gamma_{21}N_2 \tag{2.2.8}$$

$$\frac{dN_1}{dt} = -\gamma_{10}N_1 + w_{st}(v)(N_2 - N_1) + \gamma_{21}N_2 \tag{2.2.9}$$

$$\frac{dN_0}{dt} = -P_{03}N_0 + \gamma_{10}N_1 \tag{2.2.10}$$

where N_i is the population density of level i, γ_{ij} is the decay rate of a single atom from level i to j, thus $\gamma_{ij}N_i$ is the density of atoms decayed from level i to j per second. $w_{st}(\nu)$ is the probability per second (transition rate) that an atom transits from level 2 to 1 due to stimulated emission induced by a monochromatic field of frequency ν (or vice versa). P_{03} is the rate of atoms pumped per second from the ground state to level 3. We assume that the relaxation from level 3 to the upper laser level is instantaneous, which means $\gamma_{32} \to \infty$ and $N_3 \to 0$.

Then, the total population density N is given by

$$N = N_0 + N_1 + N_2 \tag{2.2.11}$$

In a steady state, we have

$$\frac{dN_3}{dt} = \frac{dN_2}{dt} = \frac{dN_1}{dt} = \frac{dN_0}{dt} = 0 \tag{2.2.12}$$

In this case, using Equation (2.2.7) – (2.2.12) we can obtain the population inversion

$$\varDelta N = N_2 - N_1 = \frac{NP_{03}(\gamma_{10} - \gamma_{21})}{w_{st}(\nu)(2P_{03} + \gamma_{10}) + \gamma_{21}P_{03} + \gamma_{10}P_{03} + \gamma_{21}\gamma_{10}} \tag{2.2.13}$$

We define the stimulated emission probability per second at the saturation state as

$$w_{sat}(\nu) = \frac{\gamma_{21}P_{03} + \gamma_{10}P_{03} + \gamma_{21}\gamma_{10}}{2P_{03} + \gamma_{10}} \tag{2.2.14}$$

Equation (2.2.13) can then be rewritten as

$$\varDelta N = \left(\frac{NP_{03}(\gamma_{10} - \gamma_{21})}{\gamma_{21}P_{03} + \gamma_{10}P_{03} + \gamma_{21}\gamma_{10}}\right)\left(\frac{1}{w_{st}(\nu)/w_{sat}(\nu) + 1}\right) \tag{2.2.15}$$

where the stimulated transition rate ($w_{st}(\nu)$) is further discussed in Ref. [74]

$$w_{st}(\nu) = \frac{A_{21}c^3}{8\pi n^3 h\nu^3}\rho(\nu)g(\nu) \tag{2.2.16}$$

where A_{21} is the spontaneous emission rate, c is the velocity of light in vacuum, n is the refractive index of the medium, $\rho(\nu)$ is the energy density of the monochromatic electromagnetic field that induces the transitions, $g(\nu)$ is lineshape function.

Equation (2.2.16) can be rewritten in terms of the intensity of the optical wave $\mathrm{I}(\nu) = \mathrm{c}\rho(\nu)/n$ as

$$w_{st}(\nu) = \frac{A_{21}c^2}{8\pi n^2 h\nu^3}\mathrm{I}(\nu)g(\nu) = \frac{\sigma(\nu)}{h\nu}\mathrm{I}(\nu) \tag{2.2.17}$$

where $\sigma(\nu)$ is the gain cross section and given by

$$\sigma(\nu) = \frac{A_{21}c^2}{8\pi n^2\nu^2}g(\nu) \tag{2.2.18}$$

Equation (2.2.17) indicates that the stimulated transition rate $w_{st}(\nu)$ is proportional to the incident light intensity $\mathrm{I}(\nu)$, so Equation (2.2.15) can be rearranged as

$$\varDelta N = \left(\frac{NP_{03}(\gamma_{10} - \gamma_{21})}{\gamma_{21}P_{03} + \gamma_{10}P_{03} + \gamma_{21}\gamma_{10}}\right)\left(\frac{1}{{}^{I(\nu)}\!/_{I_{sat}(\nu)} + 1}\right) \tag{2.2.19}$$

Where

$$I_{sat}(\nu) = \frac{h\nu}{\sigma(\nu)}w_{sat}(\nu) \tag{2.2.20}$$

is the incident light intensity at saturation state.

With the help of Equation (2.2.18) and (2.2.19), the gain coefficient of the four-level laser system is given by

$$\alpha(\nu) = \sigma(\nu)\varDelta N = \frac{\alpha_0(\nu)}{{}^{I(\nu)}\!/_{I_{sat}(\nu)} + 1} \tag{2.2.21}$$

Where

$$\alpha_0(\nu) = \sigma(\nu)\left(\frac{NP_{03}(\gamma_{10} - \gamma_{21})}{\gamma_{21}P_{03} + \gamma_{10}P_{03} + \gamma_{21}\gamma_{10}}\right) \tag{2.2.22}$$

is the gain coefficient in the absence of significant intracavity radiation, or it is often called the 'small signal gain coefficient'. For most practical 4 level lasers, $P_{03} \ll \gamma_{21} \ll \gamma_{10}$, we then have

$$\alpha_0(\nu) = \sigma(\nu)\left(\frac{NP_{03}}{\gamma_{21}}\right) \tag{2.2.23}$$

Thus, the small gain coefficient $\alpha_0(\nu)$ is proportional to the pump rate P_{03}.

The intracavity intensity in the gain medium can be obtained by transforming Equation (2.2.21) to

$$I(\nu) = I_{sat}(\nu)\left(\frac{\alpha_0(\nu)}{\alpha(\nu)} - 1\right) \tag{2.2.24}$$

It is noted that the gain coefficient $\alpha(\nu)$ of a continuous wave laser is clamped at the threshold gain coefficient $\alpha(\nu)_{thr}$ for steady-state operation.

The output power of the four-level laser can be obtained by multiplying the intracavity power by the transmission of the output coupler.

$$P(\nu)_{out} = (1 - R_1)P(\nu)_{cavity} = (1 - R_1)AI(\nu) \tag{2.2.25}$$

where A is the area of the beam in the gain medium, R_1 is reflectance of the output coupler. Therefore, substituting Equation (2.2.24) into (2.2.25) gives

$$P(\nu)_{out} = (1 - R_1)AI_{sat}(\nu)\left(\frac{\alpha_0(\nu)}{\alpha(\nu)_{thr}} - 1\right) \tag{2.2.26}$$

Because the small gain coefficient is proportional to the pump rate, Equation (2.2.26) can also be written as

$$P(\nu)_{out} = (1 - R_1)AI_{sat}(\nu)\left(\frac{P_{03}}{P_{03_{thr}}} - 1\right) \tag{2.2.27}$$

The above expression shows the linear relationship between the output power and the pump power for a CW four-level laser operated in a steady state. It is noted that a necessary condition for this equation to hold is that $P_{03} \geq P_{03_{thr}}$.

2.2.3 Optimum Output Coupling

The losses involved in a laser system mainly come from two sources: 1. the inevitable losses due to absorption, scattering and diffraction in the laser cavity; 2. the loss due to imperfect coupling of output power via partially reflecting mirrors. The first type of loss needs to be reduced as much as possible to lower the laser threshold. The second type may actually be useful. The laser threshold will be at its minimum value when the coupling loss is zero, but there is no output available. Conversely, increasing the coupling loss raises the laser threshold, and the output power will again become zero when the actual pump power is less than the threshold value. Therefore, for a fixed pump rate, there exists an optimal value for the transmission of the output coupler that maximizes the output power [75].

For a CW four-level laser in a steady state, the net round trip gain is clamped to 1, thus we obtain

$$R_1 R_2 e^{2(\alpha(\nu)-s)L} = 1 \tag{2.2.28}$$

where R_1 is the reflectance of the output coupler mirror, R_2 is the reflectance of the high reflectivity mirror, s is the attenuation coefficient, $\alpha(\nu)$ is the gain coefficient, in the steady state, $\alpha(\nu) = \alpha(\nu)_{thr}$, L is the gain medium length.

Let $Z = 1 - l_i = R_2 e^{-2sL}$, where l_i represents the fractional losses excluding the output coupler transmission. Equation (2.2.28) can be rewritten as

$$e^{2\alpha(\nu)_{thr} L} R_1 Z = 1 \tag{2.2.29}$$

Take the logarithms of both sides of Equation (2.2.29), the threshold gain coefficient is given by

$$\alpha(\nu)_{thr} = \frac{1}{2L}(-\ln(R_1 Z)) \tag{2.2.30}$$

Using the Taylor expansion, for $1 - R_1 Z \ll 1$, Equation (2.2.30) can be expressed as

$$\alpha(\nu)_{thr} = \frac{1}{2L}(1 - R_1 Z) \tag{2.2.31}$$

Substituting Equation (2.2.31) into the expression for the output power (Equation (2.2.26)), we have

$$P(\nu)_{out} = (1 - R_1) A I_{sat}(\nu) \left(\frac{\alpha_0(\nu)}{\frac{1}{2L}(1 - R_1 Z)} - 1 \right) \tag{2.2.32}$$

Maximizing $P(\nu)_{out}$ with respect to R_1 by setting ${\partial P(\nu)_{out}}/{\partial R_1} = 0$ yields the optimum value of the reflectance of the output coupler

$$R_1 = \frac{1 - \sqrt{2L\alpha_0(\nu)(1 - Z)}}{Z} \tag{2.2.33}$$

The optimum value of the transmission is thus given by

$$T_1 = 1 - R_1 = \frac{1}{Z}\left(\sqrt{2L\alpha_0(\nu)(1 - Z)} - (1 - Z) \right) \tag{2.2.34}$$

For typical values of R_2 and s, $Z = 1 - l_i = R_2 e^{-2sL} \approx 1$. Using $Z \approx 1$ & $l_i = 1 - Z$, the optimum output coupling is obtained as

$$T_1 = 1 - R_1 \approx \sqrt{2L\alpha_0(\nu) l_i} - l_i \tag{2.2.35}$$

Substituting Equation (2.2.35) into (2.2.32) gives an expression for the output power at optimum output coupling

$$P(\nu)_{out-opt} = A I_{sat}(\nu) \left(\sqrt{2L\alpha_0(\nu)} - \sqrt{l_i} \right)^2 \tag{2.2.36}$$

Figure 2.10 shows theoretical plots of the output power as a function of the transmission of the output coupler with l_i as a parameter for a He-Ne laser (632.8 nm). The experimental data (solid circles) are also presented in the figure.

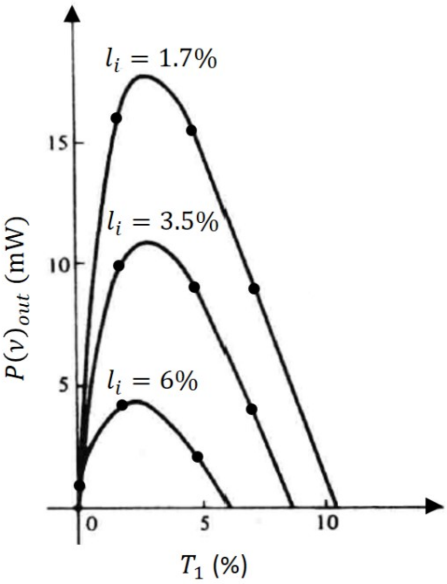

Figure 2.10. Laser output power ($P(\nu)_{out}$) against output coupler transmission (T_1) for different cavity losses (l_i) for a He-Ne laser [76].

It is apparent from Figure 2.10 that the optimal output coupling for each l_i corresponds to the maximum output power.

2.2.4 Single-mode Selection

Single-transverse-mode Selection

Transverse-mode selection is important for most laser applications. The most common method for selecting the fundamental TEM_{00} mode is to insert an aperture of suitable size into a laser cavity. This method was first used in a ruby laser resonator to restrict oscillation to one or a few low-order transverse modes [77]. In this case, the aperture introduces high loss to the higher-order modes but very little loss to the lower-order ones to achieve mode selection, since the higher-order modes tend to have a larger lateral spread in intensity than the lower-order ones. The effective restraint of higher order modes also requires their losses to be greater than the gain [78].

To quantify the ability of the aperture to select the TEM_{00} mode, the transverse mode discrimination (TMD) is introduced and defined by the ratio of L_{10} to L_{00}, where L_{10}

and L_{00} are the round-trip losses of TEM_{10} and TEM_{00} modes, respectively. Their values depend on the aperture size and the geometry of the resonator [79]. For an aperture with a radius of a, the Fresnel number of the cavity is given by $N = a^2/L\lambda$, where L is the cavity length, λ is the optical wavelength. The Fresnel number is a measure of the effect of an aperture at both cavity mirrors. As the Fresnel number decreases, the value of TMD will increase [80]. A large value of TMD indicates a good selectivity of the resonator. However, this mode-selection method inevitably introduces loss for the TEM_{00} mode itself.

The selectivity is greatest for confocal resonators and least for plane-parallel resonators [81]. Modified plane-parallel resonators have been reported to have better selectivity by using a prism reflector which has high reflectivity for a very narrow angular range [82] or shaping the reflector to match the field distribution shape of the desired mode [83]. Since the confocal resonators have the smallest fundamental mode volume of any resonator geometries, a 'cat's-eye' resonator has been used to achieve mode volume enhancement and fundamental transverse mode operation [84]. Figure 2.11 shows a schematic diagram of the 'cat's-eye' resonator. The mode volume can be enhanced to fill the gain medium by narrowing the aperture size at the mirror M_2. The mode selectivity of this system is equivalent to a conventional confocal resonator.

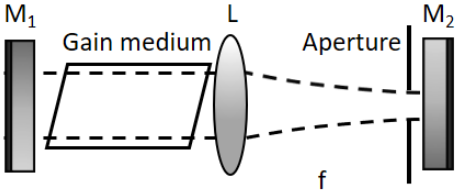

Figure 2.11. The 'cat's-eye' resonator. M_1 and M_2 are resonator mirrors. L is an antireflection coated lens with focal length f.

On the other hand, unstable resonators which can also have large mode volumes have been used for large diameter active medium to achieve fundamental mode oscillation. The use of this kind of unstable resonators for transverse mode selection was first proposed by Siegman in 1964 [85]. Previously, unstable resonators were mainly used in high-gain laser systems and have been studied both theoretically and experimentally [86–89]. Figure 2.12 shows two typical unstable resonators used in laser systems. One or both of the cavity mirrors have divergent spherical surfaces.

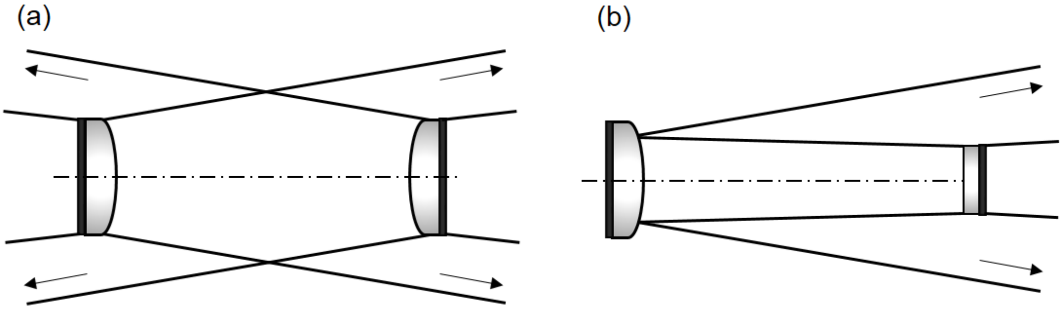

Figure 2.12. Unstable laser resonators. (a) Unstable. (b) Cassegrainian unstable.

Unstable resonators have significant diffraction losses. The diffraction losses become higher for higher order modes. The intrinsic mode discrimination is the key to achieve single transverse mode operation. The diffracted energy can be employed as a useful laser output rather than a loss via diffraction coupling [85,90].

Single-longitudinal-mode Selection

Even when a laser operates with a single transverse mode, its oscillation can still occur on several longitudinal modes. The longitudinal-mode frequency spacing in a cavity is given by $\Delta\nu = c/2L$, where c is the velocity of light, and L is the cavity length. For some cases, the single-longitudinal-mode operation can be achieved by using a short cavity length to meet the following condition

$$\Delta\nu \geq \Delta\nu_0/2 \tag{2.2.37}$$

where $\Delta\nu_0$ is the gain linewidth. In this case, the frequency spacing between longitudinal modes is relatively large, if a longitudinal mode is tuned to coincide with the center of the gain curve, the adjacent modes are far away enough from the center that they cannot lase. The required condition for this technique can be rewritten as

$$L \leq c/\Delta\nu_0 \tag{2.2.38}$$

For a practical laser, the mode tuning is achieved by fine control of the cavity length using a cavity mirror with a piezo-electric transducer. This method is effectively applied to lasers with small gain linewidths. For instance, a He-Ne laser has an inhomogeneously Doppler-broadened gain curve with a linewidth $\Delta\nu_0$ of 1.5 GHz (at 632.8 nm). According to Equation (2.2.38), this corresponds to a maximum cavity length of 20 cm. A number of single-frequency He-Ne lasers have been developed in this manner [91–94]. For solid-state lasers, the gain linewidths are usually much larger (typically a few hundred GHz). To fulfil Equation (2.2.38), the cavity length becomes too small (3mm for 100 GHz) to be practical for some application scenarios. For this reason, single-longitudinal-mode selection can be realized by other techniques discussed below.

Fabry–Pérot Etalons

Internal mode-selection techniques have been extensively used since great selectivity can be obtained with a device that is placed inside the resonator. The device introduces losses that are greater than the gain to suppress unwanted modes. A Fabry–Pérot Etalon is an example of such devices and was first used in a ruby laser for longitudinal mode selection [95]. One or more FP etalons can be inserted into the laser cavity to achieve single-longitudinal-mode selection. Figure 2.13 shows the configuration for single-longitudinal-mode selection using a FP etalon. The FP etalon is inclined at a small angle θ_0 to the z-axis, and the refraction angle of the beam within the etalon is θ.

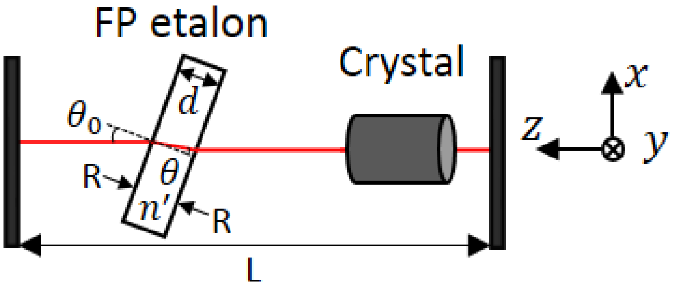

Figure 2.13. Single-longitudinal-mode operation of a solid-state laser using a Farbry-Pérot etalon.

The width ($\Delta\nu_c$) of an etalon transmission peak is given by Equation (2.1.35), and the free-spectral range ($\Delta\nu_{fsr}$) of the etalon is given by Equation (2.1.34). According to Equation (2.1.36), the free-spectral range can also be written as

$$\Delta\mathrm{v}_{fsr} = F\Delta\mathrm{v}_c \tag{2.2.39}$$

where F is the finesse of the etalon.

The angle θ needs to be fine-tuned such that a transmission peak of the etalon coincides with the longitudinal mode closest to the peak of the gain curve. If the longitudinal-mode frequency spacing $\Delta\nu = c/2L$ is larger than or equal to half of the width of the transmission peak $\Delta\nu_c$, the mode closest to the line center will be selected. Thus, the discrimination between adjacent modes requires that

$$\Delta\nu \geq \Delta\nu_c/2 \tag{2.2.40}$$

According to Equation (2.2.39), this can be rewritten as

$$\Delta\nu \geq \Delta\mathrm{v}_{fsr}/2F \tag{2.2.41}$$

To achieve single-longitudinal mode operation, it is also required that the free-spectral range $\Delta\mathrm{v}_{fsr}$ of the etalon to be larger than or equal to half of the gain linewidth $\Delta\nu_0$, which gives

$$\Delta\mathrm{v}_{fsr} \geq \Delta\nu_0/2 \tag{2.2.42}$$

Otherwise, the two adjacent transmission peaks of the etalon will allow the corresponding modes to lase.

Combining Equation (2.2.41) and (2.2.42) gives the condition for achieving single-longitudinal-mode operation using the FP etalon

$$2F\Delta\nu \geq \Delta\mathrm{v}_{fsr} \geq \Delta\nu_0/2 \tag{2.2.43}$$

According to the equation above and $\Delta\nu = c/2L$, a necessary condition is given by

$$L \leq 2Fc/\Delta\nu_0 \tag{2.2.44}$$

By comparing Equation (2.2.38) and (2.2.44), it is noticed that the cavity length can now be increased by a factor of $2F$ compared to a cavity without using an etalon.

Two or more etalons can be used to achieve single-longitudinal-mode operation if the cavity length still does not meet Condition (2.2.44). In the case of using two etalons, the thicker one is used to discriminate against adjacent longitudinal modes of the laser cavity, whereas the thinner one is responsible for discriminating against adjacent transmission peaks of the thicker etalon. Denoting the free spectral ranges of the thicker and thinner are $\Delta\nu_{fsr}$ and $\Delta\nu'_{fsr}$ respectively; assuming they have the same finesse F, then the condition for achieving single-longitudinal mode operation is given by

$$4F^2\Delta\nu \geq 2F\Delta\nu_{fsr} \geq \Delta\nu'_{fsr} \geq \Delta\nu_0/2 \tag{2.2.45}$$

For a laser system using two etalons, the cavity length needs to satisfy the following condition

$$2Fc/\Delta\nu_0 \leq L \leq (2F)^2c/\Delta\nu_0 \tag{2.2.46}$$

Therefore, the cavity length can be further increased by another factor of $2F$ compared to a cavity with using only one etalon.

Unidirectional Ring Resonators

Diode-pumped solid-state lasers can also be forced to operate on a single longitudinal mode using a unidirectional ring laser design. This approach has been widely promoted for diode-pumped solid-state lasers [96–101]. In this case, higher output power is achievable because the entire active material rather than just those regions around the maxima of the standing-wave pattern contribute to the laser output.

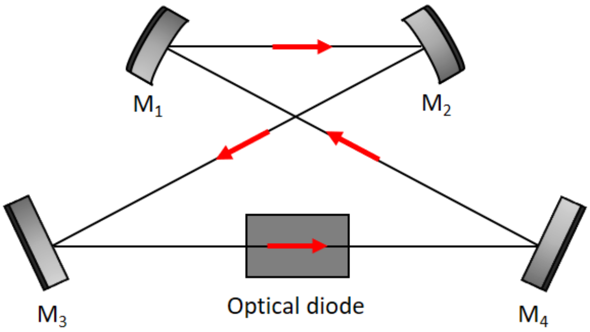

Figure 2.14. Folded unidirectional ring resonator using an optical diode.

A typical example of a folded ring configuration is shown in Figure 2.14. The resonance frequencies are obtained by imposing the condition that the total phase accumulation along the ring path to be a multiple of 2π. The expression for the resonance frequencies are given by

$$\nu = n\frac{c}{L_r} \tag{2.2.47}$$

where L_r is the effective optical path length of the ring resonator, and n is an integer. The longitudinal mode spacing in a ring resonator is therefore given by

$$\Delta\nu = \frac{c}{L_r} \tag{2.2.48}$$

To achieve unidirectional operation, a unidirectional device (or an optical diode) is inserted in the ring cavity to allow for only one propagation direction of the intracavity light. Otherwise, a standing wave pattern will be formed in the resonator and hence cause the spatial hole burning effect. This effect limits the single-frequency characteristics of a laser and reduces the laser efficiency.

In many cases, directionality control is achieved via introducing different losses for the two possible propagation directions with the unidirectional device. Conventionally, the device is a Faraday rotator combined with polarizing elements [97,100–102] For example, for the forward propagating wave (represented by the red arrow in Figure 2.14), the Faraday rotator alters the polarisation by an angle, and the polarisation-rotating element rotates the polarisation back. Therefore, these two rotations cancel each other out, and there is no net effect. For the counter-propagating light wave, these rotations are cumulative and lead to a net loss [102]. For a low gain laser, a total rotation of only a few degrees introduces enough loss discrimination to ensure unidirectional operation.

Unidirectional operation and SLM output for ring resonators have also been obtained using an intracavity acousto-optic modulator [98,99,103–106]. With radio-frequency power input and careful alignment of the modulator, a loss difference between the counter-propagating waves can be achieved. The use of the acousto-optic modulator has the advantage of low insertion loss. Alternatively, unidirectional ring resonators with no intracavity elements have been shown to achieve SLM operation [96,107] in this case the gain medium itself (Nd:YAG) within a magnetic field was used as a Faraday rotator, since it exhibits a significant Verdet constant. The Faraday rotation in one direction was thus compensated using a non-planar resonator design. This approach allows a compact system to efficiently achieve single-longitudinal-mode output.

2.3 Q-switching Operation

Q-switching is a technique used to generate laser pulses of high peak power and short pulse duration. This technique involves modulating the intracavity losses and thus switching the cavity ‘Q factor’. The Q factor is defined as the ratio of the energy stored in the cavity to the energy loss per round-trip. The lower the Q factor, the higher the losses. The dynamics of the Q-switching process and typical methods of realizing Q-switched operations are presented in this section.

2.3.1 Q-switching Theory

Conventional Q-switching involves frustrating the lasing action by decreasing the Q factor such that the population inversion increases significantly beyond the threshold value. The population inversion approaches its maximum value on a time scale comparable to the upper state lifetime of the gain medium. In this process, energy is stored in the gain medium by the pumping. Once the population inversion is close to its maximum value, the Q factor can be switched to a higher value such that the lasing action is initiated. Since the population inversion and the gain coefficient have built up while lasing has been frustrated, the excess excitation is discharged in an extremely short time. Therefore, Q-switching produces high peak power pulses of duration on the order of nanoseconds.

The Q-switching operation of a four-level laser is considered here. For the sake of simplicity, it is assumed that the switching of the Q factor from low to high values is instantaneous. If the laser cavity has a length of L and the gain medium is of length l, a fraction l/L of photons is undergoing amplification. The rate of change of the photon density is given by [74]

$$\frac{d\varphi}{dt} = \varphi\left(\frac{\alpha cl}{nL} - \frac{1}{t_c}\right) \tag{2.3.1}$$

where φ is the photon density in the cavity, c/n is the speed of light in the gain medium, t_c is the photon lifetime which is the characteristic time constant describing the decay of energy in a cavity, α is the gain coefficient and proportional to the total population inversion ΔN, as given by Equation (2.2.21). The term $\alpha cl/nL$ is the average growth constant, whilst the term $-\varphi/t_c$ represents the decrease in the number of photons per unit time caused by losses.

According to the definition of the photon lifetime, t_c can be written as

$$t_c = \frac{t_r}{\varepsilon} \tag{2.3.2}$$

where t_r is round-trip time and the ε is the fractional loss per round trip. The losses in the cavity can be expressed as

$$\varepsilon = \varepsilon_1 + \varepsilon_2 + \varepsilon_3 = -\ln R_1 - \ln R_2 + \delta \tag{2.3.3}$$

The term ε_1 represents the output coupling loss which is dependent on the reflectance R_1 of the output coupler, the term ε_2 represents a loss for the other cavity mirror (normally the value of R_2 is very close 1, so this term can be neglected), and the term ε_3 stands for the intrinsic losses due to absorption, dispersion and scattering.

Multiplying Equation (2.3.1) by t_c and defining $\tau = t/t_c$ as a normalized time variable results in

$$\frac{d\varphi}{d\tau} = \varphi\left(\frac{\alpha}{\alpha_t} - 1\right) \tag{2.3.4}$$

where $\alpha_t = nL/clt_c$ is the minimum value of the gain coefficient. As α is proportional to ΔN, the Equation (2.3.4) can be written as

$$\frac{d\varphi}{d\tau} = \varphi\left(\frac{\Delta N}{\Delta N_t} - 1\right) \tag{2.3.5}$$

where $\mathit{\Delta} N_t$ is the population inversion density at threshold. The term $\varphi \mathit{\Delta} N/\mathit{\Delta} N_t$ indicates the number of photons generated by stimulated emission per unit volume on the normalized time scale. A single transition leads to a single photon generation, which corresponds to a decrease of 2 in the inversion density, which gives

$$\frac{d\mathit{\Delta} N}{d\tau} = -2\varphi \left(\frac{\mathit{\Delta} N}{\mathit{\Delta} N_t}\right) \tag{2.3.6}$$

Dividing Equation (2.3.5) by (2.3.6) results in

$$\frac{d\varphi}{d\mathit{\Delta} N} = \frac{\mathit{\Delta} N_t}{2\mathit{\Delta} N} - \frac{1}{2} \tag{2.3.7}$$

Since the initial number of photons (φ_i) per unit volume is negligible, integrating Equation (2.3.7) gives [108]

$$\varphi = \frac{1}{2}\left[\mathit{\Delta} N_t \ln \frac{\mathit{\Delta} N}{\mathit{\Delta} N_i} - (\mathit{\Delta} N - \mathit{\Delta} N_i)\right] \tag{2.3.8}$$

The peak power of the laser pulse through the output coupler is given by

$$P_p = \left(\frac{\varepsilon_1}{t_r}\right) \mathrm{h}\nu \varphi_p V \tag{2.3.9}$$

where φ_p is the photon density in the cavity at the peak of the laser pulse, h is Planck's constant, ν is the photon frequency, and the term ε_1/t_r gives the rate of photon loss due to transmission through the output coupler. Setting ${}^{\partial\varphi}/_{\partial \mathit{\Delta} N} = 0$, it is found that the maximum photon density occurs when $\mathit{\Delta} N = \mathit{\Delta} N_t$. Putting $\mathit{\Delta} N = \mathit{\Delta} N_t$ in Equation (2.3.8) results in φ_p. Substituting the expression of φ_p into Equation (2.3.9) gives the expression for the peak power (P_p) of the pulse

$$P_p = \frac{\varepsilon_1 \mathrm{h}\nu V}{2t_r}\left[\mathit{\Delta} N_t \ln \frac{\mathit{\Delta} N_t}{\mathit{\Delta} N_i} - (\mathit{\Delta} N_t - \mathit{\Delta} N_i)\right] \tag{2.3.10}$$

If the initial inversion is well above the threshold value, *i.e.* $\mathit{\Delta} N_i \gg \mathit{\Delta} N_t$, the peak power can be approximated as

$$P_{p\,(\Delta N_i \gg \Delta N_t)} \simeq \frac{\varepsilon_1 \mathrm{h}\nu \Delta N_i V}{2t_r} \tag{2.3.11}$$

Equation (2.3.11) indicates that if $\Delta N_i \gg \Delta N_t$, the maximum number of photons stored inside the cavity is $\Delta N_i V/2$. The build-up of the pulse to its peak value occurs on a time scale shorter than the cavity photon lifetime. Therefore, at the peak of the pulse, when $\Delta N = \Delta N_t$, most of the photons (roughly $\Delta N_i V/2$) generated by stimulated emission remains in the cavity, and the energy stored in the cavity reaches its maximum value. Thereafter, the stimulated transitions continue to decrease the inversion to a final value ΔN_f ($\Delta N_f < \Delta N_t$). Figure 2.15 shows a typical numerical solution of Equation (2.3.5) and (2.3.6).

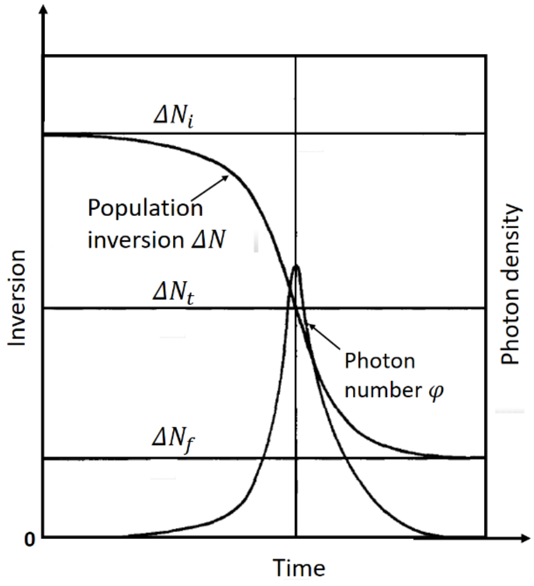

Figure 2.15. Inversion and photon density during the evolution of a giant pulse [108].

Q-switched laser pulses are widely used in applications (e.g. remote sensing, material machining and drilling, range finding and tattoo removal) which require high peak power and relatively short pulse duration. In most cases, regular pulse trains are generated using repetitive Q-switching, the pulse repetition rate is very system dependent, which typically ranges from Hz to MHz in frequency. The first Q-switched operation of a ruby optical maser was demonstrated in 1961 [109]. Since then, a variety of methods have been developed to achieve Q-switching. Generally, they are divided into two categories: active and passive Q-switching, which will be discussed separately for clarity in the following section.

2.3.2 Active Q-switching

Active Q-switching is realized with an active control device, typically either an acousto-optic or electro-optic modulator. Mechanical devices such as spinning prisms have also been used historically for Q-switching [110]. These active Q-switches all need to be driven by external sources.

Acousto-optic Q-switching

In acousto-optic Q-switching, a transparent optical material (usually fused quartz) acts as a phase grating when an ultrasonic wave passes through it. The ultrasonic wave is launched by a piezoelectric transducer driven by a radiofrequency oscillator. The strain field of the ultrasonic wave leads to changes in the local refractive index due to the photoelastic effect [111]. The resultant phase grating has an amplitude proportional to that of the acoustic wave and a period the same as the acoustic wavelength.

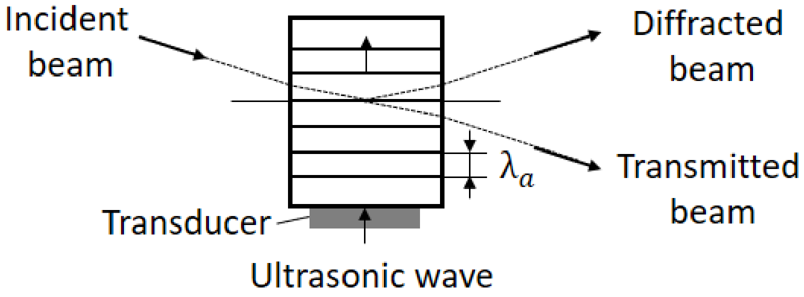

Figure 2.16. Schematic setup of an acousto-optic modulator.

If a light beam is incident on the grating, as shown in Figure 2.16, a fraction of the beam will be diffracted out of the incident beam direction. Thus, when a proper driving voltage is applied to the transducer, an acousto-optic modulator in a laser resonator provides an additional loss (due to beam diffraction) to frustrate lasing. The laser is then returned to the high Q-state by switching off the driving voltage [7].

Acousto-optic modulators possess the advantage of having low insertion loss, and they can be operated at high repetition rates for repetitive Q-switching. However, the loss introduced into a cavity in the low Q-state is rather limited. Compared with electro-optic modulators, the switching speed is rather slow, which is limited by the transit time of the acoustic wave through the laser beam.

Electro-optic Q-switching

Electro-optic modulators are the most widely used active devices for Q-switched lasers. They exploit an electro-optic effect, usually the Pockels effect, to produce Q-switching. The Pockels effect is the phenomenon manifested when the refractive index of a medium is modified in proportion to the strength of an applied electric field. A Pockels cell that comprises a nonlinear crystal is a typical electro-optical device that is used to modulate the intracavity losses of lasers. The nonlinear crystal exhibits birefringence under the influence of an external electric field. The birefringence in the crystal is typically characterized using two orthogonal directions – ‘fast’ and ‘slow’ axes. The refractive indices in the ‘fast’ and ‘slow’ axes are defined as [112]

$$n_f = n_0 - \frac{1}{2} n_0^3 r E, \qquad n_s = n_0 + \frac{1}{2} n_0^3 r E \tag{2.3.12}$$

where n_0 is the nominal refractive index, r is the electro-optic coefficient, and E is the electric field applied to the nonlinear crystal. If a linearly polarized beam is incident on the crystal at 45° to both the ‘fast’ and ‘slow’ axes, the beam will split into two orthogonal components, and each component will experience a different refractive index. For a crystal of length l, this leads to a phase difference between the two components after traversing the Pockels cell. The phase difference $\Delta\varphi$ is given by

$$\Delta\varphi = \left(\frac{2\pi}{\lambda}\right) \Delta n l \tag{2.3.13}$$

where

$$\Delta n = n_0^3 r E \tag{2.3.14}$$

is the value of the induced birefringence, which is obtained according to Equation (2.3.12). As can be seen from the equations listed above, the phase difference is dependent on the voltage applied to the Pockels cell.

Pockels cells have two types of geometries concerning the direction of the applied electric field: longitudinal and transverse devices. The former have the electric field in the direction of the light beam (see Figure 2.17 (a)), whereas the transverse devices have the electric field perpendicular to the light beam (see Figure 2.17 (b)).

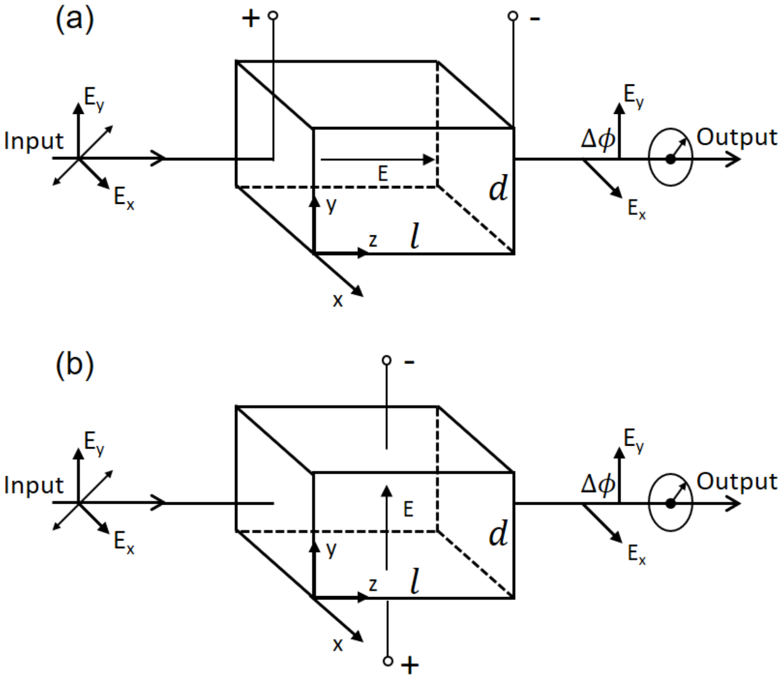

Figure 2.17. (a) Pockels cell with longitudinal electric field. (b) Pockels cell with transverse electric field.

For a longitudinal Pockels cell, the voltage is applied along the crystal length l. According to Equation (2.3.13) and (2.3.14), the phase difference between the orthogonal electric field vectors (E_x and E_y) after passing through a longitudinal device is given by

$$\Delta\phi_l = \frac{2\pi}{\lambda} {n_o}^3 r V \tag{2.3.15}$$

where V is the applied voltage ($V = El$). From this equation, it can be concluded that the voltage is independent of the crystal dimensions. However, the phase difference of light passing through a transverse Pockels cell is given by

$$\Delta\phi_t = \frac{2\pi}{\lambda} {n_o}^3 rV \frac{l}{d} \tag{2.3.16}$$

where l is the crystal length, and d is the dimension of the crystal along the direction of the applied voltage. The phase difference $\Delta\phi_t$ is proportional to the applied voltage V and the crystal aspect ratio (l/d). For a certain phase difference, a large crystal aspect ratio means a low switching voltage.

Figure 2.17 shows a common arrangement that involves a Pockels cell and a polarizer to realise Q-switching operation. The Pockels cell is oriented such that the birefringence axes are both orthogonal to the axis of the resonator. The transmission axis of the polarizer is at an angle of 45° to the birefringence axes.

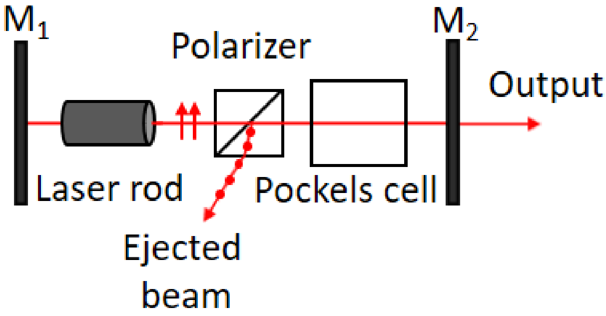

Figure 2.18. Schematics illustrating a Q-switched laser using an electro-optic device, i.e. Pockels cell.

If the voltage applied to the Pockels cell is set to produce a phase difference $\Delta\varphi = \pi/2$, the Pockels cell functions as a quarter-wave plate, so the linearly polarized light passing through it becomes circularly polarized. After being reflected at the Mirror (M_2), the radiation again passes through the Pockels cell and its two orthogonal components acquire an additional $\pi/2$ phase difference. Thus, the total phase difference is π. The radiation becomes linearly polarized again but orthogonal to its original polarisation axis. As a result, the radiation is ejected from the cavity by the polarizer (see Figure 2.18), thus creating a high intracavity loss. When the voltage on the Pockels cell is switched off, the induced birefringence disappears, and the linearly polarized light passes through the Pockels cell without any change of polarisation. Oscillation inside the cavity will build up, and a Q-switched pulse will be generated after a short delay [11].

The required voltage for operating the Pockels cell as a quarter-wave plate is called the quarter-wave voltage. For Q-switching, the half-wave voltage leading to a half-wave retardation ($\Delta\varphi = \pi$) is also of some interest, since a combination of a Pockels cell and two crossed polarizers can also be used to achieve Q-switching. Therefore, a Pockels cell can be used as a voltage-controlled waveplate by applying a constant voltage. For active Q-switching, the pulse energy and duration depend on the laser gain, which is related to the pump power and the pulse repetition rates. The pulse repetition rates of an active Q-switched laser can be controlled via the pockels cell.

2.3.3 Passive Q-switching

For passive Q-switching, the losses are modulated with a saturable absorber. The switching operation is automatically achieved by the optical nonlinearity of the saturable absorber. Semiconductor saturable absorber mirrors (SESAMs) are typical saturable absorbers widely used for passive Q-switching.

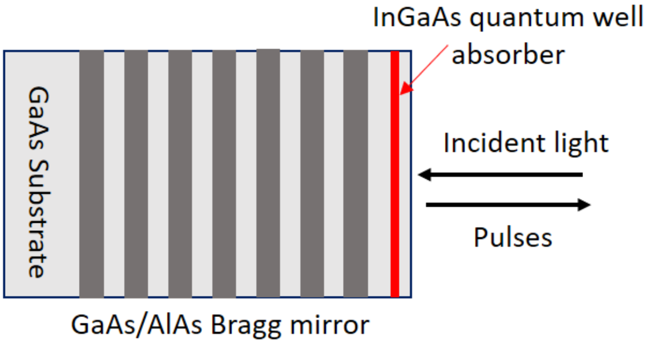

Figure 2.19. Structure of a typical SESAM for passive Q-switching operation.

A SESAM consists of a single quantum well absorber layer and a semiconductor Bragg mirror, as shown in Figure 2.19. The material of the Bragg mirror has relatively large bandgap energy, so absorption does not occur in this region. A thicker absorber layer can be used to obtain a large modulation depth. The saturable absorption of a SESAM is related to an intraband transition, the energy of the absorbed photons is transferred to electrons, which are then excited from the valence band to the conduction band. The absorption of the device remains unsaturated at low incident optical intensity because only a small number of electrons are excited from the valence band to the conduction band. Laser action starts when the gain exceeds the sum of the loss of the saturable absorber and the unsaturable cavity losses. The intracavity optical intensity builds up quickly from the noise arising from spontaneous emission. At relatively high intensity, the excited electrons accumulate until the states in the conduction band are fully occupied. Therefore, the absorption is reduced due to saturation. After the generation of a very powerful pulse, the absorption recovers on a time scale of picoseconds level.

Typical parameters of a SESAM includes the operation wavelength, saturation intensity, modulation depth, and absorption recovery time, which can be designed for certain operation by varying the material compositions and design parameters [113]. There are also other types of saturable absorbers with very different parameters for a variety of applications, including saturable absorber crystals (e.g. Cr^{4+}:YAG) [114], Gallium arsenide (GaAs) [115], thin layers of carbon nanotubes [116,117], quantum dots dopped glasses [118], single or multiple graphene layers [119,120], alcohol [121] and even pure water [122].

Compared to active Q-switching with a Pockels cell, pulse energy and pulse duration are fixed for passive Q-switching with a SESAM at a certain pump level. Passive Q-switches using SESAMs provide a simple method of Q-switching with which implementation will benefit from a penetration depth of several micrometers. The increase of the cavity length is negligible, thus maintaining the original cavity length. Whereas, active Q-switching requires a bulky modulator to be placed inside the cavity.

Chapter 3

Diode-pumped Alexandrite Lasers

The suitability of a crystal as a laser gain medium is dependent on several factors, including crystal growth methods, physical properties of the host crystal and spectroscopic properties of the dopant. This chapter analyses the physical and spectroscopic properties of Alexandrite that make it suitable as a gain medium for high power lasers. The physical properties of Alexandrite are also compared with several common laser crystals to demonstrate its advantages. Interestingly, Alexandrite lasers can operate as either a 3-level or a 4-level system, and the corresponding laser mechanisms in both cases are explained. This thesis work focuses on the characteristics of Alexandrite as a vibronic 4-level laser. Moreover, the 4-level model can be used to predict the temperature-dependent characteristics, which are necessary to consider to access the full potential laser wavelength tuning range of Alexandrite [46]. The wavelength tuning limits are explained by combining absorption and emission processes. Due to the special energy level structure of Alexandrite with broad absorption bands, the choice of pump source is diverse, which enables different requirements for various applications.

3.1 Alexandrite Physical Properties

Alexandrite is the common name for Chromium-doped chrysoberyl (Cr^{3+}:$BeAl_2O_4$). Natural Alexandrite gemstones first discovered in 1830 in the Ural Mountains were highly prized because of its unique colouring. The observed colour of Alexandrite changes from greenish blue under daylight to red under incandescent illumination. As a laser medium, synthetic Alexandrite crystals can be produced by the Czochralski growth method in large boules [49].

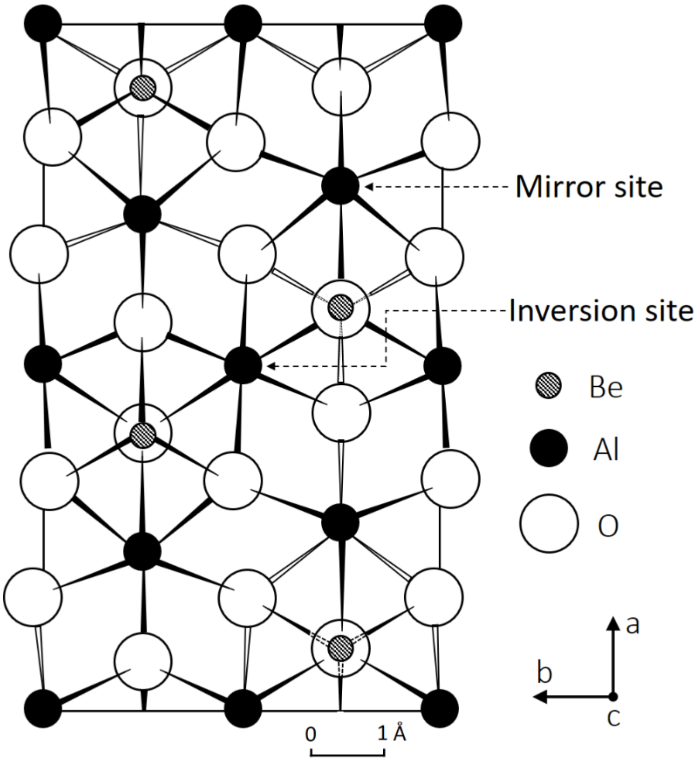

Figure 3.1. C-axis view of chrysoberyl structure. Adapted from [123]. Examples of a mirror site and an inversion site are indicated.

The host material chrysoberyl has an orthorhombic structure with $BeAl_2O_4$ forming a unit cell. The c-axis view of the chrysoberyl unit cell is illustrated in Figure 3.1. The dimensions of the unit cell are $a = 0.9404$ nm, $b = 0.5476$ nm, $c = 0.4425$ nm [123]. There exist two types of aluminium ions sites in the lattice, one with mirror symmetry and the other with inversion symmetry. The mirror sites can better accommodate the Cr^{3+} ions. Therefore, when Al^{3+} are replaced by Cr^{3+}, approximately 78% of the total Chromium ions depositing into the mirror sites [49]. The ions on the mirror sites dominate the optical properties and are crucial for laser emission [45,124]. The dopant concentration of Cr^{3+} is expressed in terms of the percentage of Al^{3+} ions that have been substituted by Cr^{3+} ions. Typical Cr^{3+} doping concentrations of Alexandrite laser crystals ranges from 0.05 at. % to 0.3 at. %, where the optimum concentration depends on the crystal dimensions, pump source, and the practical applications [49].

Table 3**.** Comparison of material parameters of Alexandrite, Ruby and Nd:YAG [7,45,125–127].

Gain Medium	Alexandrite	Ruby	Nd:YAG
Doping concentration (at. %)	0.05-0.3	0.05	1.0
Density (g/cm^3)	3.7	4.0	4.6
Refractive index (Avg.)	1.74 (750 nm)	1.76 (694 nm)	1.82 (1064 nm)
Nonlinear refractive index (x10^{-20} m^2/K)	2.0 ± 0.3	2.5 ± 0.35	7.23 ± 1.4
dn/dT (x10^{-6} K^{-1})	8.0	12.6	7.3
Hardness (kg/mm^2)	2000	1.7	1215
Thermal conductivity (W/(cm*K))	0.23	0.42	0.14
Thermal expansion coefficient (x10^{-6}/K) (Avg.)	6.2	5.8	7.9
Thermal fracture limit (W/cm)	600	1000	120
Melting point (°C)	1870	2040	1970

The physical properties of Alexandrite compared to Ruby (Chromium-doped sapphire) and Nd:YAG (Neodymium-doped Yttrium Aluminium garnet) are summarized in Table 3. Ruby is one of the most robust solid-state laser materials in terms of hardness. It is interesting as a comparison to Alexandrite as they are both Chromium-doped crystals. Ruby is also mechanically and optically similar to Alexandrite. Nd:YAG is one of the most commonly used solid-state laser materials in real-world applications. It possesses a combination of properties favourable for laser operation, such as substantial laser gain and good optical quality. For these reasons Ruby and Nd:YAG are good examples of typical laser material properties, although Ruby being a three-level laser has high inversion requirement limiting its practicality for commercial use.

Alexandrite has many superior properties, including relatively high strength, high thermal conductivity and high thermal fracture limit, which enables it to be pumped with high power/energy, both CW and pulsed, without thermal fracture. The thermal conductivity of a laser material is an important parameter as it is a measure of its ability to conduct heat. Higher thermal conductivity allows for faster heat dissipation and results in less heat-induced effects, such as thermal lensing and thermally induced depolarisation. The high thermal conductivity (0.23 Wcm^{-1}K^{-1}) of Alexandrite is roughly twice that of Nd:YAG and two-thirds that of Ruby. The thermal fracture limit is also of significance as it determines the maximum power loading per unit length that can be tolerated without fracture. This parameter is proportional to the thermal conductivity and inversely proportional to the square root of the thermal expansion coefficient. Alexandrite's high thermal fracture limit (600 W/cm) is five times that of Nd:YAG and sixty percent that of Ruby.

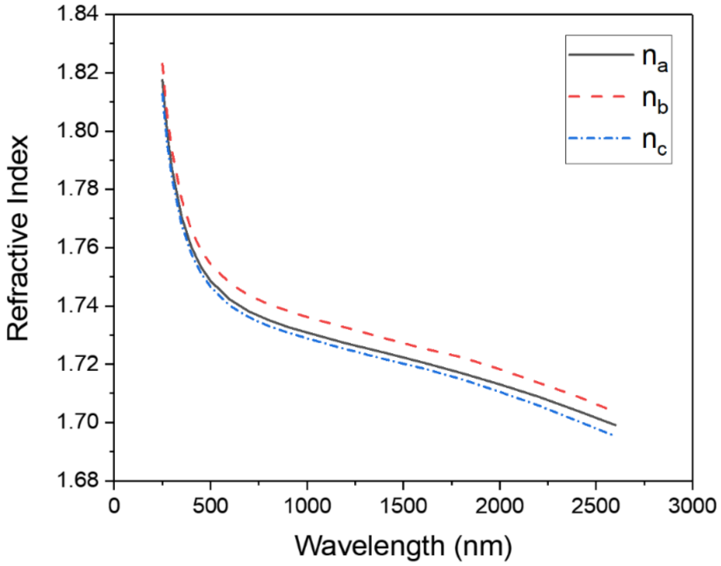

Figure 3.2. Refractive indices (n_a, n_b and n_c) of Alexandrite versus wavelength for the E∥a, E∥b and E∥c polarisations. Adapted from [45].

Alexandrite is optically biaxial because of its orthorhombic symmetry. The refractive indices for the wavelength range 0.25-2.5 µm are shown in Figure 3.2. The nonlinear refractive index coefficient of Alexandrite is more than 3 times lower than that of Nd:YAG; therefore, Alexandrite is less susceptible to self-focusing at extreme power levels.

The optical damage threshold for both surface and bulk of Alexandrite has been reported to exceed power densities of 23 GW/cm^2 and fluences of 270 J/cm^2, which was obtained using a focused beam with 12 ns pulse duration and 16 µm diameter spot size [49]. However, optical damage has also been shown to occur at 1.5 GW/cm^2 in experiments with Alexandrite oscillators. The substantially decreased optical damage threshold was attributed to randomly distributed surface defects [49].

3.2 Alexandrite Laser Properties

Alexandrite is of great interest as a solid-state laser material since it has a broad emission band (701-858 nm) [45,46] and a high intrinsic slope efficiency of 65% [48]. The lasing mechanisms and spectroscopic properties of Alexandrite are studied in detail in this section as they provide vitally important information for understanding the lasing characteristics.

3.2.1 Lasing Mechanisms

Alexandrite can be operated as a 3-level system or a 4-level vibronic laser. Two theoretical models have been well developed for describing the different kinetics. As a 3-level laser system, the energy level structure of Alexandrite lasers is similar to that of Ruby lasers.

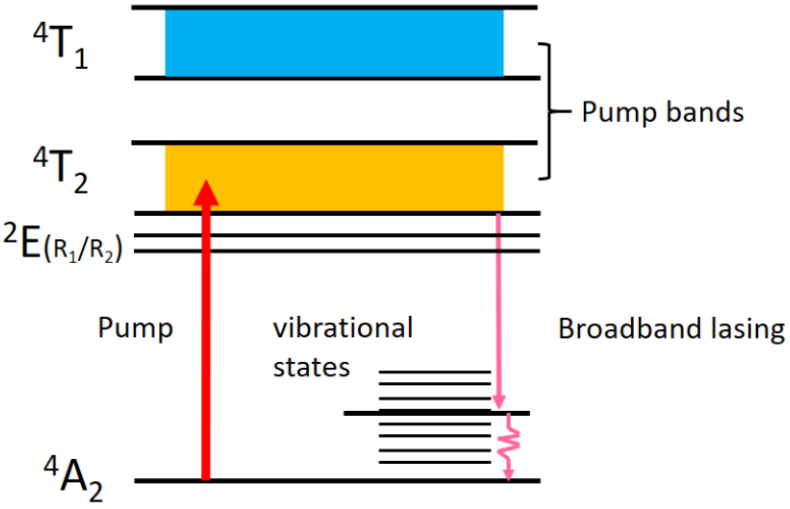

Figure 3.3. Simplified energy level structure for Chromium ions in Alexandrite. The transition occurring between the vibronically broadened $^4T_2$ and $^4A_2$ levels corresponds to a 4-level laser system.

The simplified energy level diagram of Chromium ions in Alexandrite is shown in Figure 3.3. The $^4A_2$ level is the ground state. The vibronically broadened $^4T_1$ and $^4T_2$ levels, arising from the strong coupling between the outmost unshielded electrons of the transition ions Cr^{3+}, are two adjacent absorption state energy continua. Similar to

Ruby, Alexandrite has a metastable level ^2E, which acts as a storage level and lies 800 cm^{-1} below the $^4T_2$ level [7]. Ions excited to the $^4T_1$ and $^4T_2$ states rapidly decay to the ^2E state, and the lifetime of the ^2E state (~1.5 ms) is much longer than that of the $^4T_1$ and $^4T_2$ states (the lifetime of the $^4T_2$ state is ~6.6 μs) [49]. The ^2E level is actually a doublet that consists of R_1 (680.4 nm) and R_2 (678.5 nm) lines. The emission cross section at 680.4 nm is significantly larger than that at 678.5 nm. Therefore, lasing at the vicinity of the 680.4 nm wavelength can be obtained utilizing the transition from the ^2E level to the $^4A_2$ ground level, which corresponds to the R-line emission lasing at 694.3 nm of the Ruby laser [6]. In the 3-level mode, the metastable ^2E state is regarded as the upper laser level, whereas the $^4A_2$ level is viewed as the lower laser level. As a 3-level system, Alexandrite has a high laser threshold, low efficiency and fixed output wavelength of 680.4 nm at room temperature [7].

Alexandrite is of interest primarily because of its vibronic nature. For the 4-level mode, transitions from the upper laser level $^4T_2$ to vibrationally excited states within $^4A_2$ results in vibronic lasing. Then, the immediate emission of the phonon enables the whole system to recover equilibrium. The vibrational states are higher than the ground level. The upper laser level $^4T_2$ is always in thermal equilibrium with the ^2E level since the energy difference (800 cm^{-1}) between $^4T_2$ and ^2E corresponds to only a few KT at room temperature. A considerable population will be present in the $^4T_2$ state when the ^2E state has been populated. By contrast, the energy difference between the $^4T_2$ and ^2E levels in Ruby is 2300 cm^{-1} [37]. Hence, effectively all the excited populations are stored in the ^2E level in Ruby. The laser wavelength of Alexandrite depends on which vibrational state acts as the terminal level of the transition. Therefore, the transition occurring between two broad energy bands results in broadly tunable radiation of Alexandrite lasers. During the lasing process, because of Alexandrite's vibronic nature, the emission of photons is accompanied by the emission of phonons. Due to strong coupling, ions with remnant energy in the vibrational states (the lower laser level) return to the ground level $^4A_2$ via non-radiative phonon relaxation. In other words, the remnant energy is carried off by the vibrational phonons. Additionally, the fact that the

^2E and $^4T_2$ levels are in thermal equilibrium in Alexandrite is a critical reason why the performance of Alexandrite laser is temperature-dependent [46,128].

3.2.2 Spectroscopic Characteristics

The room-temperature absorption spectra of Alexandrite for Cr^{3+} doping concentration of 0.063 at.% are shown in Figure 3.4. The spectra arise from absorption mostly due to the mirror-site ions which dominate the spectroscopic properties of Alexandrite under non-cryogenic conditions [45].

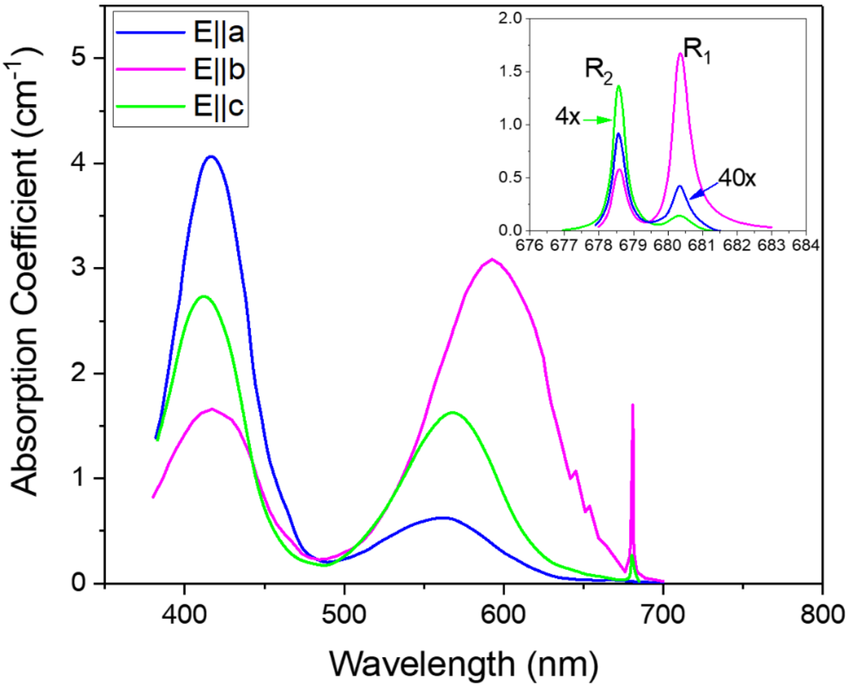

Figure 3.4. Alexandrite absorption spectrum for Cr^{3+} dopant concentration of 0.063 at.%. Inset: R-line absorption spectra. The E∥a and E∥c polarisations have been amplified by the amounts indicated. Adapted from [45].

The absorption spectra effectively cover the entire visible spectral region. The sharp structure appearing at 680 nm is associated with R line absorption. The two broad bands centered at 410 nm and 590 nm are transitions from $^4A_2$ to the vibrational states of $^4T_1$ and $^4T_2$, which are vibrationally broadened. Absorption from the $^4A_2$ to the $^4T_2$ level is weaker and shifted to higher energies for the E∥a and E∥c compared to E∥b. This is partly due to the fine structure of the degenerate $^4T_2$ level [129]. The crystal field and spin-orbit interactions split the $^4T_2$ level into three states denoted as T_1, T_2 and T_3 in order of low to high energy. The transition from $^4A_2$ to the higher energy level T_3 is dominant in E∥a and E∥c polarisations, so the vibronic absorption occurs with higher energy (shorter wavelength) photons.

The sharp lines are associated with transition from the $^4A_2$ state to the ^2E level (R-lines). Since the absorption spectra have a relatively low resolution at R-lines, it is difficult to ascertain the change of the absorption coefficient with different polarisations. The data of R-line absorption are given in the inset of Figure 3.4. The intensity of the transition to the R_1 line is significantly larger than the transition to the R_2 line for the E∥b polarisation.

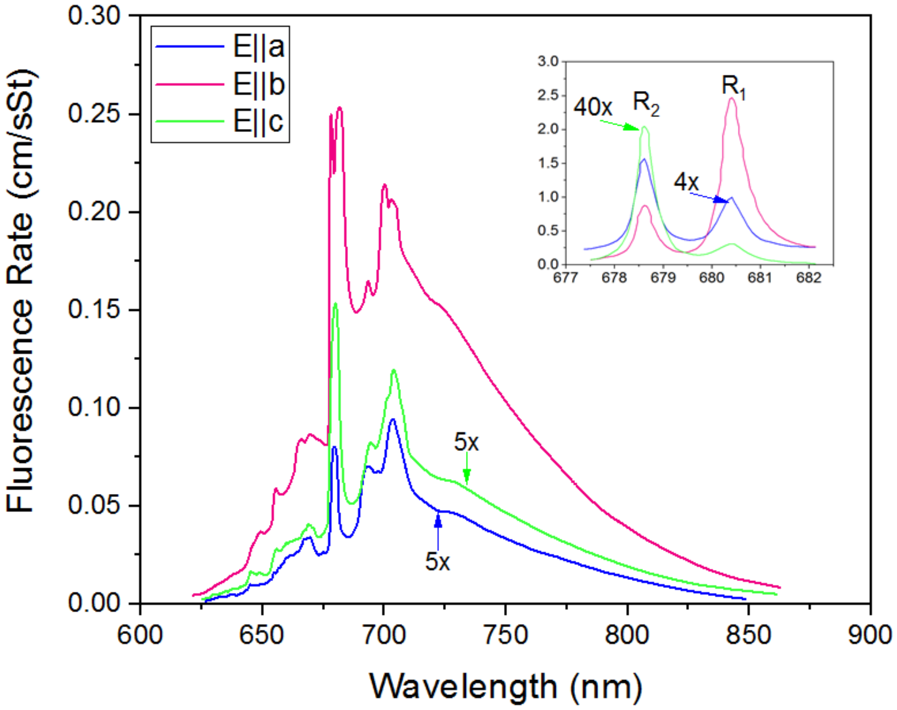

Figure 3.5. Alexandrite fluorescence rate spectra at 300 K. The **E∥a** and **E∥c** polarisations have been amplified by the amounts indicated. Inset: High-resolution spectra at R-lines. Adapted from [45,130].

The fluorescence spectra of Alexandrite at room temperature are shown in Figure 3.5. The inset shows the high-resolution spectra around the R-lines. The fluorescence spectrum for the E∥b polarisation shows strong emission at R-lines. The sharp lines are accompanied with a broad background fluorescence spectrum. The broad spectrum that arises from the vibronic transitions ($^4T_2 \rightarrow {}^4A_2$) is responsible for the tunable vibronic laser gain. The fluorescence in the E||b polarisation is an order of magnitude larger than the fluorescence in the E||a and E||c polarisations. The reduced vibronic fluorescence intensity for the E||a and E||c polarisations is partly due to a lower occupancy of the T_3 level of the $^4T_2$ triplet, and partly because of a weaker vibronic strength [45]. This results in polarised vibronic laser emission from Alexandrite because of the relationship between the laser gain and fluorescence intensity [131]. The gain along the b-axis polarisation is approximately 10 times that along the a- or c-axis polarisation.

3.2.3 Lasing Temperature Dependent Characteristics

Fluorescence Lifetime

The fluorescence lifetime of Alexandrite has a strong temperature dependence. In the 4-level laser model, the vibronic level $^4T_2$ is in thermal equilibrium with the long-lived state ^2E. The effective lifetime of the upper laser level at room temperature can be calculated by assuming that the upper level consists of these two strongly coupled levels in a Boltzmann distribution with energy spacing of ΔE=800 cm^{-1}. Therefore, a two-level model can be used to predict the fluorescence lifetime of Alexandrite. The fluorescence lifetime is dependent on the relative populations of these two levels. In this case, the effective lifetime (τ_{eff}) is given by

$$\frac{1}{\tau_{eff}} = \frac{f_E}{\tau_E} + \frac{f_T}{\tau_T} \tag{3.2.1}$$

where f_E is the fractional population of the ^2E state, f_T is the fractional population of the $^4T_2$ level, and $f_E = 1 - f_T$. The ^2E and $^4T_2$ levels have a lifetime of $\tau_E = 1.54$ ms and $\tau_T = 6.6$ μs, respectively. The population of each level will obey the Boltzmann distribution, thus,

$$f_T = \frac{e^{-\frac{\Delta E}{k_b T}}}{1 + e^{-\frac{\Delta E}{k_b T}}} \tag{3.2.2}$$

where ΔE is the energy spacing between the $^4T_2$ and ^2E levels, k_b is the Boltzmann constant. Substituting Equation (3.2.2) into (3.2.1) gives the expression of the effective fluorescence lifetime,

$$\tau_{eff} = \tau_E \left[\frac{1 + e^{-\frac{\Delta E}{k_b T}}}{1 + \left(\frac{\tau_E}{\tau_T}\right) e^{-\frac{\Delta E}{k_b T}}} \right] \tag{3.2.3}$$

It can be seen from Equation (3.2.3) that the effective fluorescence lifetime of Alexandrite is temperature dependent. It can be viewed as a combination of the lifetime of the $^4T_2$ level and that of the storage ^2E level. The fluorescence lifetime over a temperature range of 4 - 500 K was successfully predicted by Walling et. al. using the two-level model [45], as shown in Figure 3.6. The fluorescence lifetime of Alexandrite is approximately 260 µs at room temperature and 130 µs at 100 °C.

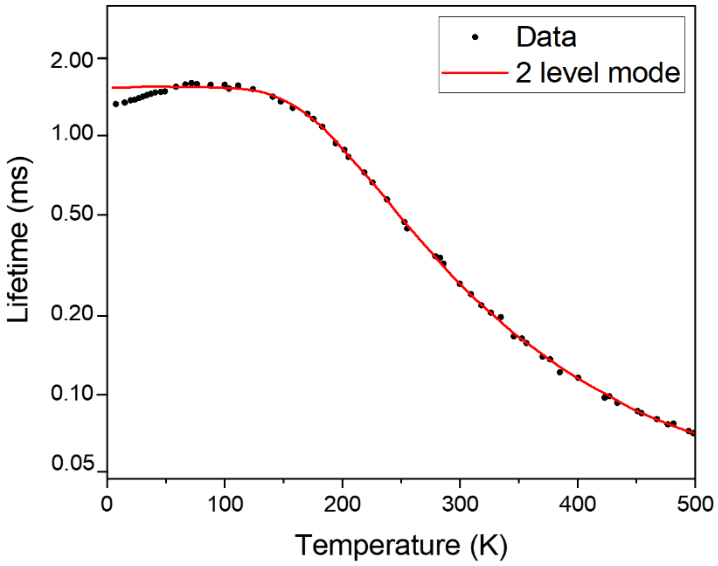

Figure 3.6. The fluorescence lifetime of Alexandrite as a function of temperature. The experimental data (discrete black points) and the simulation curve (red solid line) are indicated. Adapted from [45].

In the range of 4 to 70 K, the lifetime increases with increasing temperature, due to thermal excitation of ions from the lower ^2E level to the longer lifetime upper ^2E level. The reduced lifetime with temperatures greater than 70 K is caused by thermal excitation to the higher lying $^4T_2$ triplet levels with a higher decay rate [45,129].

Another study on the fluorescence lifetime of Alexandrite was conducted in the range of 293 to 973 K. It found the two-level model could not predict the rapid reduction in the fluorescence lifetime at higher temperatures. The study suggested that when the temperature exceeds approximately 673 K, nonradiative transitions will prevail and be responsible for the rapid relaxation of the excited ions [132]. Whereas, the nonradiative transitions of the excited ions are negligible at lower temperatures.

Alexandrite's long fluorescence lifetime is a particular advantage over widely wavelength-tunable Ti:sapphire lasers that possess a fluorescence lifetime of only 3.2 μs at room temperature. The long fluorescence lifetime of Alexandrite indicates a great potential for energy storage and thus Q-switching operation.

Stimulated Emission Cross Section

As the temperature of Alexandrite increases, the effective emission cross section of Alexandrite increases. The effective emission cross section $\sigma_e(\mathrm{E})$ is related to the fluorescence, which is given by [45]

$$\sigma_e(\mathrm{E}) = f_\Omega^*(\mathrm{E})\frac{h^3c^2}{E^2n_\Omega^2} \tag{3.2.3}$$

where $f_\Omega^*(\mathrm{E})$ is the total emission rate at energy E for photons with polarisation Ω, h is the Planck's constant, c is the speed of light, n_Ω is the refractive index for light polarized along Ω. $f_\Omega^*(\mathrm{E})$ is proportional to the measured fluorescence spectrum, and the proportionality factor can be determined from the fluorescence lifetime τ_{eff} by the following relation [45]

$$\frac{1}{\tau_{eff}} = \frac{8\pi}{3h}\sum_{\Omega}\int_0^\infty dE f_\Omega^*(\mathrm{E}) \tag{3.2.4}$$

The effective emission cross section $\sigma_e(\mathrm{E})$ increasing with temperature has been experimentally confirmed by Shand *et al.* [133]. This is mainly because the fluorescence lifetime τ_{eff} decreases with increasing temperature, as discussed earlier.

The temperature dependence of the effective emission cross section can also be explained using the 4-level model. The ^2E level act as a storage level for the $^4T_2$ level. As the temperature rises, the occupation fraction of the $^4T_2$ level increases compared to that of the lower lying ^2E level due to thermal excitation. The increased population in the upper laser level ($^4T_2$) will increase the probability of stimulated emission.

Ground State Absorption

Ground state absorption (GSA) arises from transitions from vibrational states of the ground level to the $^4T_2$ level. The ground state absorption cross section in the lasing wavelength region is orders of magnitude smaller than that in the pump bands. It was determined over a lasing wavelength range from 690 to 830 nm by Shand *et al.* both theoretically and experimentally [124]. By extending the McCumber theory [131] and applying it to Alexandrite, the formula for determining the GSA cross section is given by [45,124]

$$\sigma_a(E) = \sigma_e(E) exp\left[\frac{(E - E^*)}{k_b T}\right] \tag{3.2.5}$$

where $\sigma_a(E)$ is the GSA cross section, $\sigma_e(E)$ is the effective emission cross section, E is the photon energy, E^* is the effective non-phonon energy level energy, k_b is the Boltzmann constant, and T is the temperature of the Alexandrite crystal. The theoretical value of $\sigma_a(E)$ is in good agreement with experimental data, as shown in Figure 3.7. The figure also shows the comparison between $\sigma_a(E)$ and $\sigma_e(E)$. GSA is insignificant at the long-wavelength part of the gain region since $\sigma_a(E)$ is many orders of magnitude smaller than $\sigma_e(E)$. However, $\sigma_a(E)$ is relatively large at high energies and hence acts as a limit to the shortest lasing wavelength. This results in the shortest wavelength that has been demonstrated of 701 nm.

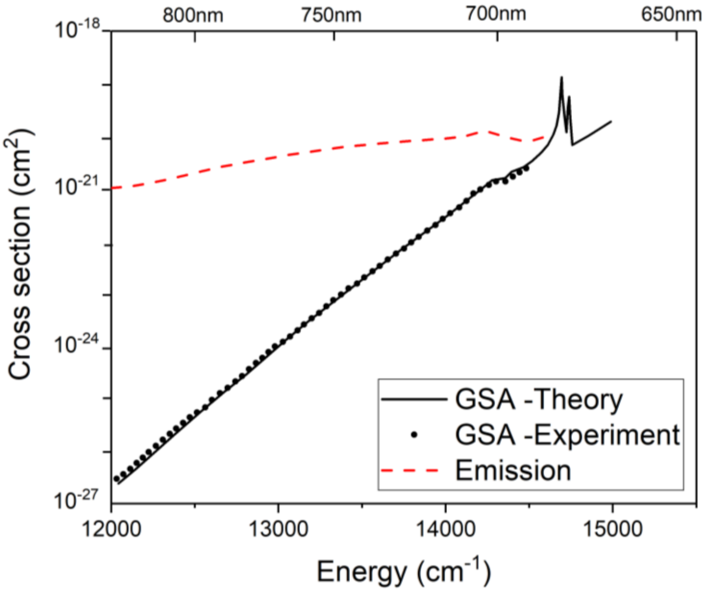

Figure 3.7. The GSA and emission cross sections of Alexandrite. The solid curve is the theoretical value of the GSA cross section. The dotted curve represents the experimental data of the GSA cross section. The red dashed curve shows the value of the emission cross section. Adapted from [124].

Excited State Absorption

Excited state absorption (ESA) occurs when the pump or laser radiation is absorbed by laser ions in the upper laser level. The ions are excited to a higher-lying energy level and then decay back to the upper laser level non-radiatively in Alexandrite. This constitutes a loss mechanism since the optical energy is converted into heat after absorption. The additional loss leads to an increase in the lasing threshold and a reduction of the slope efficiency. In Alexandrite, ESA initiates from both the ^2E and $^4T_2$ levels. The ESA cross section from $^4T_2$ is seven times larger than that from ^2E [134]. Therefore, it can be assumed that ESA mainly initiates from $^4T_2$, which is consistent with other studies [133,135,136].

ESA occurs at wavelengths throughout the pump and laser bands. Figure 3.8 shows the ESA cross section in the pump band (420-680 nm) of Alexandrite. The ESA cross section is of the same order of magnitude as the GSA cross section, which means a relatively large portion of the pump energy can be directly lost at high population inversion due to the existence of ESA [135].

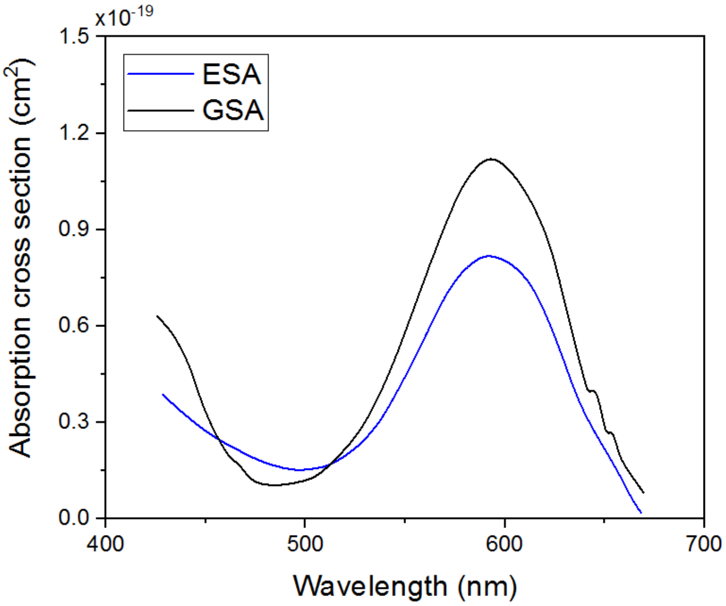

Figure 3.8. The ESA cross section compared with the GSA cross section for light polarized along the b-axis of Alexandrite. Adapted from [135].

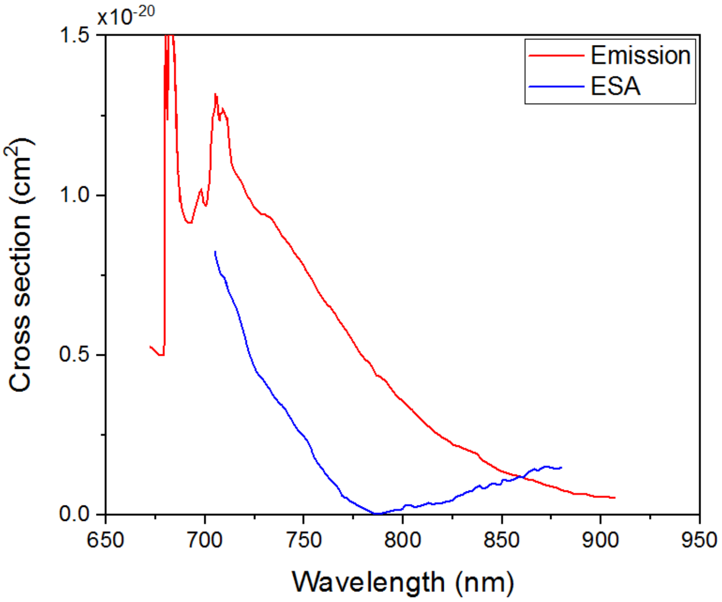

Figure 3.9. The ESA cross section in the lasing wavelength region compared with the emission cross section. Adapted from [136].

Figure 3.9 shows the ESA cross section compared with the emission cross section in the lasing region (700-850 nm). ESA in the lasing wavelength region has a substantial impact on the laser performance as it competes with the laser emission process. It will reduce the gain and even prevent lasing when the ESA and emission cross sections are equal. The extreme case occurs at 818nm (at 28 °C), which limits the long wavelength side of the tuning range [133]. Kuper *et al.* have demonstrated this limit can be pushed to 858 nm by operating the Alexandrite laser at an extremely high temperature of 513 °C [46]. The ESA cross section increases with increasing temperatures at a rate equal to that of the emission cross section [133]. The increase in ESA cross section can also be explained by the increased population of the $^4T_2$ level at elevated temperature.

3.3 Optical Pumping of Alexandrite Lasers

Lasing mechanisms of Alexandrite have been discussed with reference to the simplified energy level diagram (Figure 3.3) in Section 3.2.1. Transitions from the ground level $^4A_2$ to $^4T_1/^4T_2$ create two broad absorption bands peaking at around 410 and 590 nm. Furthermore, the $^4A_2 \rightarrow R_{1/2}$ transitions generate two narrow bands peaking at 678.5 and 680.4 nm. These different excitation bands offer diverse pump source options for Alexandrite, such as arc lamps [137–140], flashlamps [45,128,133,135,136,141,142], krypton ion lasers [143], dye lasers [48], frequency-doubled Nd-doped lasers [144–147], laser diodes [37,48,148–159], LEDs [160] and even visible solar radiation [161].

Historically, lamp pumping has been the most popular and prolific scheme mainly because extremely high pump powers can be generated by lamps (often with average powers of several kilowatts). Laser output power in excess of 50 W has been achieved with a Xenon arc Lamp-pumped Alexandrite laser; however, lamp pumping leads to low slope efficiency (maximum 2.5%) [139]. Krypton ion gas laser pumping was used primarily to characterize the laser parameters of Alexandrite, but it has also proven to be an effective way to generate tunable emission. Although a slope efficiency of 51% was obtained with Krypton laser pumping, the overall system was limited by the high cost and complexity of the pump source [143]. Similarly, dye laser pumping achieved a very high slope efficiency of 64% but also resulted in a high cost and practicality issues of the pump system [48]. Frequency-doubled Nd:YVO$_4$ laser (532 nm) pumping provided a relatively high output power of 1.4 W with 36% slope efficiency, however, the complicated pump system and high quantum defect limites its usability for the Alexandrite laser [145]. Since the performance of LEDs has experienced improvement and their cost has dropped sharply since the early 2000s, LEDs have been reconsidered for laser pumping in the visible spectral range. Although LED pumping offers a low-cost option, the low irradiance of LEDs needs to be improved using additional luminescent concentrator . A LED pumped Ce:YAG concentrator has been used as a pump source for Alexandrite, but the overall efficiency is still low (with optical efficiency of 1.7%) [160].

The potential of red-diode-pumping Alexandrite, which leads to simplicity and high efficiency, has been recognized by the academic community since the early 1990s. Scheps *et al.* demonstrated the first diode-pumped Alexandrite laser in 1990 [152] and then achieved 25 mW output power with 28% slope efficiency in 1993 [48]. Through diode-bar-pumping, Peng *et al.* obtained 1.3W output power with 24.5% slope efficiency in 2005 [153]. Then, Beyatli *et al.* utilized a high-brightness tapered diode laser (TDL) as the pump laser and achieved 200 mW output power with a slope efficiency of 38% in 2013 [37]. In the same year, Teppitaksak *et al.* demonstrated that diode-end-pumped Alexandrite laser can be operated to achieve multi-ten watt (>26 W) output power with a slope efficiency of 49% [154]. Using a fiber-coupled diode module, Kerridge-Johns *et al.* obtained a slope efficiency of 54% in 2018, which is the highest slope efficiency diode-pumped Alexandrite laser to date [148]. Early studies on diode pumping of Alexandrite lasers were limited by the brightness of the laser diodes. In contrast, the remarkable progress made in diode-pumped Alexandrite lasers in recent years has benefited from significant advances in high-brightness visible laser diodes. These and other studies have shown that diode-pumping of Alexandrite lasers is a promising route to high efficiency, low cost and compactness.

3.4 Applications of Alexandrite Lasers

Application for Alexandrite lasers are emerging in many areas, including remote sensing, dermatology, spectroscopy and nonlinear optics. These use the attractive properties of Alexandrite, such as the broad tunability and capability of pulsed operations (both Q-switching and mode-locking).

Despite having low efficiency, lamp-pumped Alexandrite lasers have played a leading role. Due to the superior thermo-mechanical properties of the material, high powers and energies were obtained using extremely high pump power [49,137,138]. The broad wavelength emission could be extended by nonlinear optical processes like frequency doubling. Therefore, lamp-pumped Alexandrite lasers have been widely applied in scientific research and industrial applications. PAL^{TM} pulsed Alexandrite laser system designed by Light Age, Inc. is a typical example. Based on a flashlamp pumped scheme, the PAL^{TM} is a tunable and versatile laser system that can produce pulse energy up to 1 J. It can be operated at any fixed wavelength between 720 and 800 nm. Pulses with durations as short as 100 ps can be generated under mode-locked operation. This sophisticated product can be used in the fields of illumination, spectroscopy, metrology and material processing [162].

Alexandrite lasers are used for treating skin disorders (e.g. pigmented lesions) [163,164] and cosmetic skin surgery (e.g. hair removal [165,166] and tattoo removal [167–169]). They were found to treat pigmented lesions well due to its ability to target melanin [163]. They are also effective in the treatment of unwanted hair, as the laser energy is absorbed specifically by the hair follicle rather than any other target on or within the skin surface [165]. Tattoo removal treatment is used to remove black, blue and green pigment since these colours can effectively absorb the wavelength emitted by Alexandrite lasers. The application of Q-switched Alexandrite lasers has remarkably improved the process of tattoo removal. Previous treatment methods including surgical removal, cryosurgery and dermabrasion require tissue destruction and hence leaving scars. Commercial Alexandrite lasers allow the energy to be precisely confined to the tattoo pigments and significantly reduce the risk of scarring [167]. They can precisely destroy the target lesion or pigment and ensure tissue in the surrounding area remains undamaged.

LIDAR (Light Detection and Ranging) is an optical remote sensing technology that performs measurements by illuminating a target with pulsed laser light and measuring the reflected signals with a sensor. LIDAR systems are powerful tools for a range of remote sensing applications. These include investigating physical attributes of the atmosphere (e.g. temperature and wind speed), measuring atmospheric composition (e.g. clouds, aerosols and ozone), and characterizing the Earth environment (e.g. vegetation and water cover) [170]. Such information is of significance for meteorology and atmospheric research and allows scientists to investigate natural and artificial environments with precision and flexibility. For LIDAR systems, highly stable pulsed lasers with high energy, narrow linewidth, and near diffraction limited beam quality are often required to guarantee measurement accuracy. For example, for a backscatter LIDAR, it requires specifications as follows: pulse energy - multi-tens of mJ (singal-to noise ratio), pulse duration <100 ns (vertical resolution), pulse repetition rate - 100 Hz (lateral resolution), spectral width >50 MHz (spectral resulation), spatial beam quality $M^2<1.5$ (spatial resolution). Flashlamp-pumped Q-switched Alexandrite lasers have been developed for differential absorption LIDAR systems to measure atmospheric humidity and temperature since the tuning range of Alexandrite covers high absorption lines of species of interest (water vapor for humidity (720-730 nm) and oxygen for temperature (760-770 nm) [171–175]. Pulsed Alexandrite lasers have also been employed by potassium LIDAR systems for mesopause temperature profiling, which is based on measuring the Doppler broadened line width of potassium at 770 nm [176,177].

The development of diode-pumped Alexandrite lasers has been of great interest since the early 1990s because the advancement of high power, cost-efficient and visible wavelength laser diodes can result in efficient, compact and low-cost formats. Therefore, diode-pumped Alexandrite lasers can address remote sensing applications as a more efficient and compact laser approach [170,178]. They are also suitable for laser-based altimetry, which can measure the height of the terrain to provide a topography mapping with high spatial resolution.

It is worth mentioning that diode-pumped Nd:YAG lasers are established systems for LIDAR applications [179–182]. However, Nd:YAG lasers that lack wavelength tunability can only deliver a fixed wavelength of 1064 nm. Although other wavelengths can be achieved via harmonic generation or optical parametric conversion, the overall efficiency is relatively low. Diode-pumped Alexandrite lasers with broad tunability are versatile laser sources for LIDAR applications as compared with Nd:YAG lasers. The broad spectral range of Alexandrite overlaps the Red-Edge of vegetation, where the reflectance of vegetation changes steeply from low to high reflection in the near infrared range [183]. This makes Alexandrite a suitable laser source for monitoring vegetation. The frequency-doubled Alexandrite laser, operating as a tunable UV source, provides simplification and efficiency advantages over Nd:YAG where third-harmonic generation is required. The tunable UV Alexandrite laser can be used for Doppler LIDAR in detection of wind shear [184]. Recent work on Q-switched diode-pumped Alexandrite lasers for LIDAR applications has achieved significant progress [157,185,186] which also demonstrates exciting prospects of Alexandrite lasers as a wavelength-tunable source for addressing remote sensing applications.

This chapter has presented an overview of the properties of Alexandrite and its suitability as a gain medium for high power lasers. Laser kinetics for Alexandrite operated as either a 3-level or a 4-level system have been explained in depth. To better understand the behaviour of Alexandrite and to optimize the laser performance, the temperature-dependent characteristics have been investigated. Multiple pump source options and the versatility of the Alexandrite lasers have resulted in a broad range of applications.

Chapter 4

Actively Q-switched Alexandrite Lasers

Laser sources with short-pulse output capability are beneficial in many applications, for example in remote sensing where high temporal resolution is required or multi-photon microscopy where high peak power is needed. Alexandrite is an attractive gain medium for these applications. It has a long upper-state lifetime of 260 μs at room temperature which enables great energy storage in Q-switched operation. In the previous work of our group, the first diode-pumped Q-switched Alexandrite laser was demonstrated in 2014. The pump module was operated in quasi continuous wave mode [154]. Subsequent studies have also shown the potential for short-pulse (femtosecond level) operation of Alexandrite lasers [146,187].

This chapter aims to describe the developments of diode-pumped Q-switched Alexandrite lasers. It starts with the introduction of the pump sources used in this thesis work. The design and experimental results of the first Q-switched Alexandrite laser under CW pumping are shown. The Q-switching was achieved via loss modulation through the use of a BBO Pockels cell. The Q-switched operation was demonstrated at repetition rates up to 10 kHz, which is an order of magnitude higher than that of the previous study. Due to the low gain characteristics of Alexandrite, a pulse duration of a few nanoseconds, for example as required for altimetry LIDAR, can hardly be achieved with the standard Q-switching method. In order to obtain short pulses with high peak power, a cavity-dumped Q-switched Alexandrite laser was developed, and the experimental results are given at the end of this chapter. Some of the results in this chapter have contributed to the published work [157].

4.1 Laser-diode Pump Source

High power red diode lasers have become commercially available in recent years. Two commercial laser diode modules were used as pump sources in this work: a tailored free-space laser module (see Figure 4.1 (a)) and a fiber-coupled one (see Figure 4.1 (b)). The free-space laser-diode module provides high output power, high polarisation purity, but low beam quality as compared with the fiber-coupled one. The high-power free-space module was used in actively Q-switching (Chapter 4) and unidirectional single-frequency operation (Chapter 6) of Alexandrite lasers, whereas the fiber-coupled diode module was employed in passively Q-switched Alexandrite laser (Chapter 5). The properties of these two pump modules are depicted below.

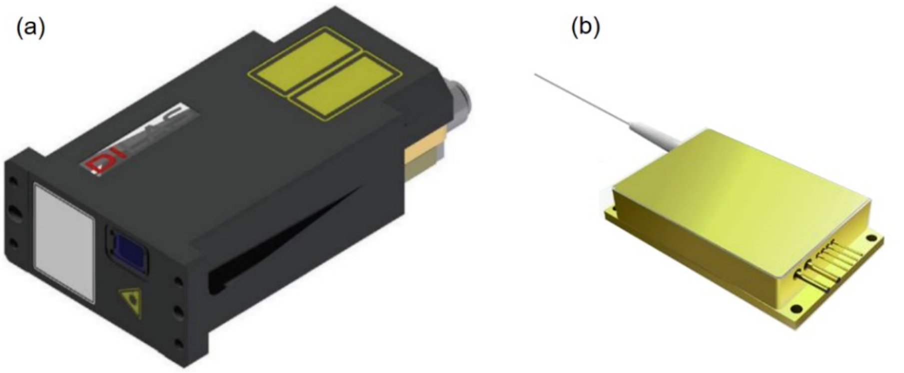

Figure 4.1. Two commercial laser-diode modules used as pump lasers in this work. (a) Free-space laser-diode module. (b) Fiber-coupled laser-diode module.

4.1.1 Free-space Laser Diode Module

The free-space laser diode module consists of 7 red conduction-cooled diode bars operating nominally at the central wavelength of 638 nm with a bandwidth (FWHM) of 1.5 nm. Cooled with a water chiller the diode module is capable of providing 66 W optical power in CW mode at 16°C with beam quality factor $M^2_x = 265$ in horizontal and $M^2_y = 30$ in vertical. Beam quality measurement throughout this thesis was made using ISO standard D4σ method, which has been explained in section 2.1.4. The overall package has dimensions 90 x 150 x 40 mm.

The optical output of each bar has both fast and slow axis collimation optics. The collimated outputs of the 7 bars are re-assembled by a set of turning mirrors such that the outputs are optically stacked one above the other with a bar-to-bar separation of 0.8 mm. The output emission is emitted through a rectangular window, and the overall effective size is nominally 5 x 5 mm at the window. An image of the output directly onto a CMOS camera is shown in Figure 4.2.

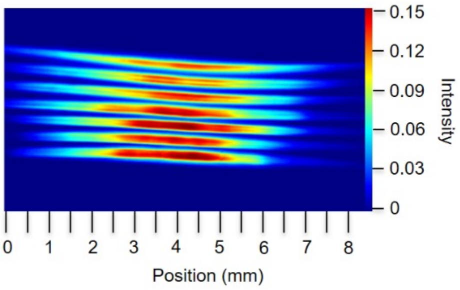

Figure 4.2. Beam profile of 7-bar diode module showing the individual bars.

The output of the diode module is controlled by a constant current diode driver. Adjustment of the driving current controls the output power. The module has external electrical connection points for attaching the cabling for current drive. A water-cooling manifold beneath the module is used to provide heat dissipation and temperature control of the diodes via the thermal base plate under the bars.

Figure 4.3 (a) shows the output power and compliance voltage of the diode module against the drive current at a water temperature of 16°C. Figure 4.3 (b) depicts the corresponding peak wavelength of the output versus drive current.

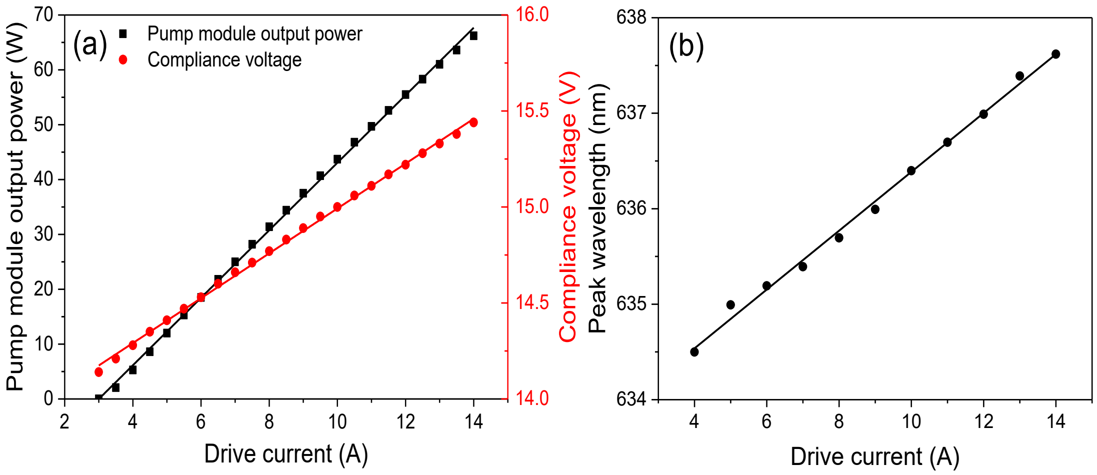

Figure 4.3. (a) The output power and compliance voltage of the 7-bar diode pump module against drive current. (b) The peak wavelength against drive current at water temperature of 16°C.

The diode pump module had a threshold of 3.0 A. The power-current slope efficiency was 6.2 W/A. 66 W pump power was obtained at the maximum drive current of 14 A (with 15.4 V voltage) resulting in a wall-plug efficiency (the ratio of optical output to consumed electrical input power) of 30.6%. The output of the module was near-linearly polarized with polarisation purity of 99%. The power curve is approximately linear with drive current, but there is a small rollover at higher drive currents. This is because increasing drive current leads to heat generation and temperature rise in the laser diode chip, and the efficiency of the diode drops at higher temperatures. The peak wavelength of the output is not fixed but experiences a redshift as the temperature increases, as shown in Figure 4.3 (b).

4.1.2 Fiber-coupled Laser Diode Module

The fiber-coupled red diode laser operates at the central wavelength of 636 nm with a bandwidth (FWHM) of 1.5 nm. This module consisting of multiple single emitter diodes was mounted on a water-cooled copper block. The output of the diode module was coupled into a multi-mode fiber with a core diameter of 105 µm and a numerical aperture of 0.22. The output of the multimode fibre had a measured beam quality $M^2_x = 45$ and $M^2_y = 46$. This module has a relatively small footprint with dimensions 43 x

74 x 13 mm, which can enable the compactness of the entire system. It was driven by a DC power supply and provided 5.3 W of optical power in CW mode at a drive current of 0.7 A. The fiber-coupled diode module had been shown previously to produce watt-level laser power with a TEM_{00} beam from Alexandrite lasers [156,188].

An aspheric fiber collimator with a focal length of 35 mm was used to collimate the output of the fiber-coupled diode module. As the fiber delivery partially scrambles the polarisation of the pump laser, the maximum polarisation axis of the pump laser contained only 70% of the pump power. The output power of the diode module was measured as a function of drive current at three different coolant temperatures (16, 20 and 24 °C), as shown in Figure 4.4 (a). The results show that the threshold decreases while the slope efficiency increases at lower temperatures.

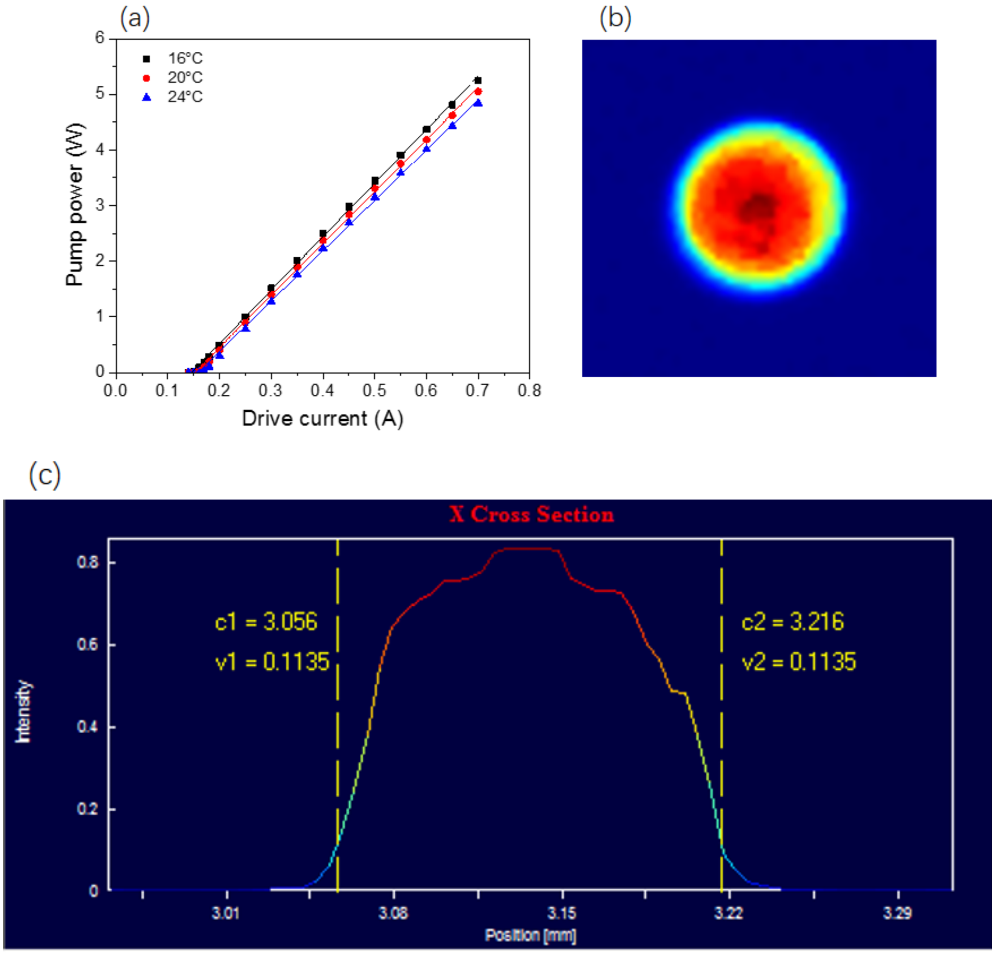

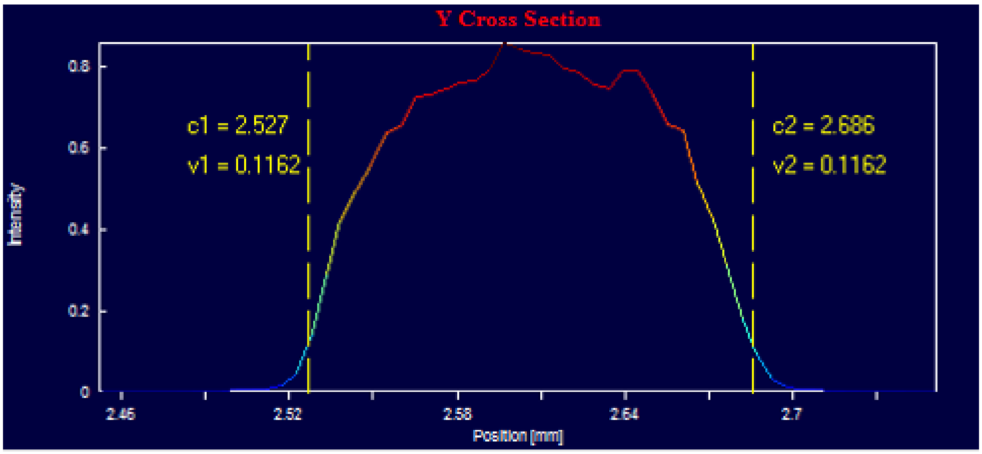

Figure 4.4. (a) The pump power of the diode module against drive current for three different coolant temperatures. (b) Spatial mode profile of the pump beam with M^2_x = 45 and M^2_y = 46 at 5.3 W pumping power. (c) Cross sections and beam width measurements ($1/e^2$) of the spatial mode profile in X and Y directions.

At 16 °C, the diode module had a threshold current of 0.14 A. The power-current slope efficiency was 9.6 W/A. An output power of 5.3 W was achieved at the recommended maximum drive current (0.7 A). Although a higher output power is achievable at lower temperatures, the lowest temperature used was 16°C to avoid condensation in the diode module. Figure 4.4 (b) shows the spatial profile of the pump beam waist at 16°C, which had an approximately super Gaussian beam shape. Figure 4.4 (c) shows the beam cross sections and beam width measurement. The laser beam has a diameter ($1/e^2$) of 160 µm (x) by 159µm (y).

Figure 4.5 shows the central wavelength of the pump module against drive current for three different coolant temperatures (16, 20 and 24 °C). The central wavelength shifts to longer wavelengths at higher temperatures and higher drive current due to the heating effect.

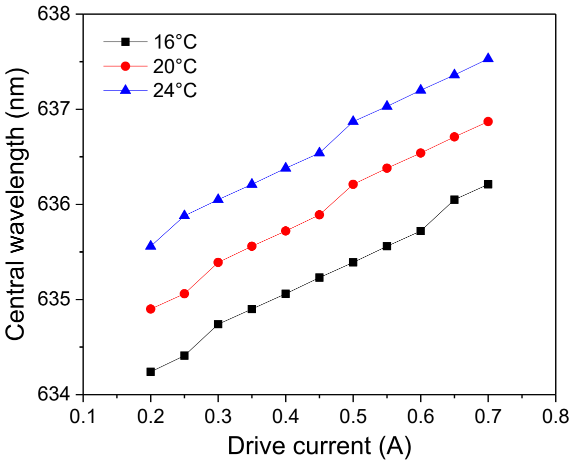

Figure 4.5. The central wavelength of the pump module against drive current for three different coolant temperatures.

By comparison, it is found each of the two red diode modules has its own advantages and disadvantages. The free-space diode module with high power and high polarisation purity can facilitate high power operation of Alexandrite laser, whereas the fibre-coupled device can produce a better beam quality and achieve a more compact footprint of the overall system.

4.2 High Efficiency Diode-end-pumped Alexandrite Laser

A compact cavity was developed and investigated to assess the power and efficiency potential of the diode-end-pumped Alexandrite laser. Figure 4.6 shows the schematic of the laser configuration. The laser system consisted of a pump module, a pump beam shaping system, a compact cavity and an Alexandrite rod.

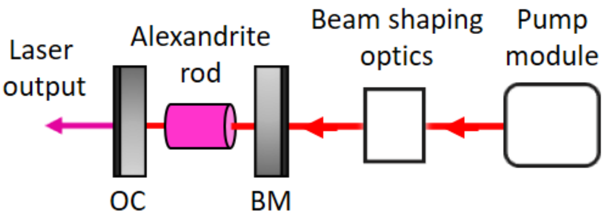

Figure 4.6. Schematic of the diode-end-pumped compact cavity Alexandrite laser.

The pump module used was the high-power free-space diode laser discussed in Section 4.1.1. Due to the highly-multimode spatial output of the pump module in the horizontal direction, the output was spatially redistributed using a beam shaping system to improve the M^2 in the horizontal slow axis. The beam shaping system is described in greater detail in Section 4.2.1.

The end-pumped Alexandrite rod with a length of 10 mm, a diameter of 4 mm and 0.22 at.% Cr^{3+}-doping concentration was embedded in a water-cooled copper heat-sink for temperature control. The end faces of the Alexandrite rod were plane-parallel and anti-reflection coated at laser wavelength (~755 nm). The absorption coefficient of the alexandrite rod was measured to be 6.0 cm^{-1} with a He-Ne laser (633 nm) for light polarized parallel to the b-axis of the crystal. Approximately 5% of the incident pump was reflected by the coated plane surface of the Alexandrite rod, and the remaining 95% was almost completely absorbed by the crystal.

The compact cavity was formed of two plane mirrors: a dichroic back mirror (BM) which was highly-transmitting (R<0.2%) for the pump (~638 nm) and highly-reflecting (R>99.9%) at laser wavelength (~755 nm) and an output coupler (OC). The compact cavity was investigated with three output couplers with reflectances of 99%, 98% and 97%, respectively. The cavity length was kept at 16mm.

4.2.1 Pump Beam Shaping

The pump beam was spatially redistributed with a beam shaping system to improve the horizontal beam quality but at the expense of worsening the vertical one. The highly-multimode spatial output of the diode module was reshaped by the optical system shown in Figure 4.7.

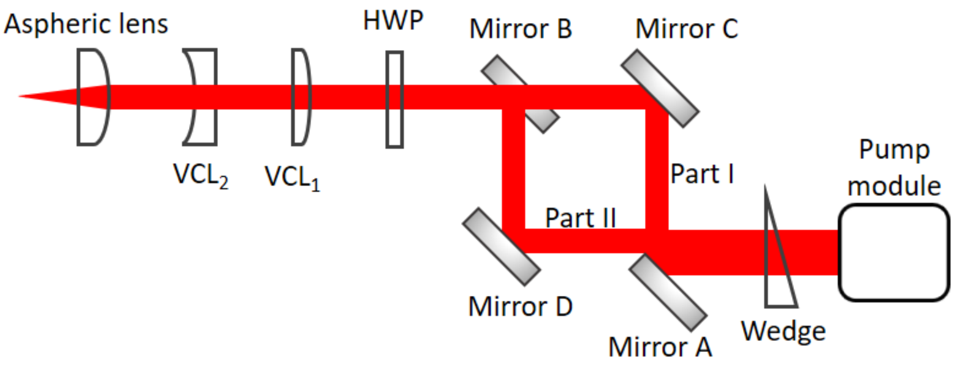

Figure 4.7. Schematic of the beam shaping system (top view). Mirror A and B are edge coated mirrors (HR at pump wavelength at 45°). Mirror C and D are HR mirrors at visible wavelengths at 45°. VCL$_1$ and VCL$_2$ are vertical cylindrical lenses with focal length of 150 and -50 mm, respectively. HWP is a half-wave plate.

The pump beam firstly hits a wedge that deflects the beam at a small downward angle (4°). The concept of using four mirrors to split and re-stack the pump beam through the wedge is shown in Figure 4.8. Two edge coated mirrors (Mirror A and B) are highly-reflecting (HR) at the pump wavelength (~638 nm) at 45°, and the other two mirrors (Mirror C and D) are HR at visible wavelengths at 45°. Mirror A horizontally splits the beam into two parts - Part I and II. At the point of splitting, the height of Part I is the same as that of Part II. Part II continues downwards until it reaches Mirror D, whereas Part I that reflected by Mirror A remains the same height. Part I and Part II, respectively reflected by Mirror C and D, were re-combined one above the other in the vertical direction at Mirror B.

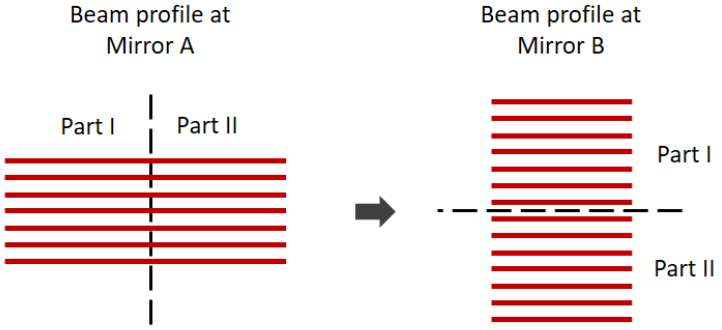

Figure 4.8. Schematic diagram of splitting and re-stacking the pump beam.

The re-stacked beam then passed through a Galilean telescope system formed of two vertical cylindrical lenses (VCL$_1$ & VCL$_2$) with focal lengths of 150 and -50mm, respectively. This system was used to narrow the pump beam in the vertical direction. A half-wave plate (HWP) was used to alter the polarisation state of the pump beam to be parallel with the b-axis of the Alexandrite rod for high absorption. The pump beam was finally focused by an aspherical lens with 40 mm focal length to a spot with a waist diameter of 350 µm (x) by 250 µm (y). The confocal parameters of the pump laser in the horizontal (2.0 mm) and in the vertical (3.8 mm) were both longer than the absorption depth (1.7 mm) of the Alexandrite rod.

After passing through the beam shaping system, the beam quality factor M^2_x decreased from 265 to 231, whilst M^2_y increased from 30 to 68. Although the beam quality M^2_y in the vertical direction degrades, the pump beam became more circular at focus. The more circular the pump beam at focus, the better the mode matching, since the laser cavity was designed for circular geometry. The improved beam quality M^2_x in the horizontal direction resulted in a longer confocal parameter, which allowed a better overlap of the pump and laser modes resulting in higher extraction efficiency.

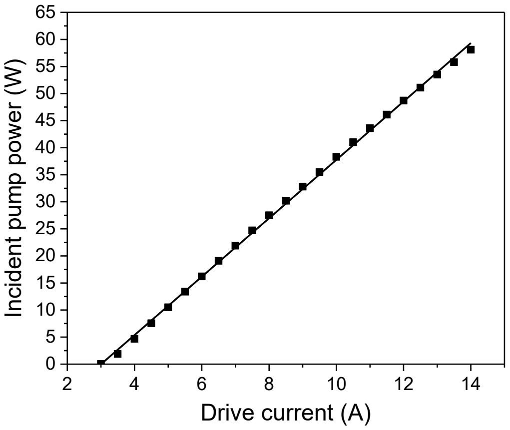

Figure 4.9. The power of the reshaped pump beam incident on the crystal against drive current at water temperature of 16°C.

Figure 4.9 shows the incident pump power of the reshaped beam on the crystal as a function of the drive current. An incident pump power of 58 W was obtained at 14 A drive current. The threshold was 3.0 A, and the power-current slope efficiency was 5.4 W/A. In comparison with the power curve shown in Figure 4.3 (a), the maximum power dropped by 8 W, due to the reflection losses of the beam shaping optics.

4.2.2 Results of Continuous-wave Operation

Figure 4.10 shows the results of the output power of the compact cavity Alexandrite laser against incident pump power for different output couplers. The crystal was cooled with a water chiller, and the temperature was set as 18°C.

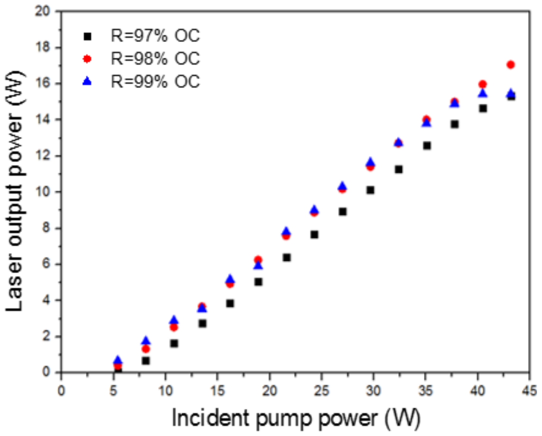

Figure 4.10. The laser output power against incident pump power for the compact cavity Alexandrite laser with three output couplers with reflectances of 99%, 98% and 97%, respectively.

The highest slope efficiency was 45.6% for the R=98% OC. The laser produced 17.1 W output power at a pump level of 43.1 W, corresponding to an optical-to-optical conversion efficiency of 39.7%. For the R=99% OC, the power curve at higher pumping level tends to roll over. The overall slope efficiency was 42.8% for the R=99% OC, but the value was 44.5% when the pump power was under 40 W.

Increasing the cavity mirror reflectance decreases the laser threshold as expected from 4-level laser theory. In terms of slope efficiency, there was an optimum reflectance at approximately 98% for the compact cavity. Decreasing the reflectance to 97% decreased the slope efficiency. This is due to the pump ESA effect, the higher laser threshold achieved with lower reflectance increased the population inversion and the pump ESA loss.

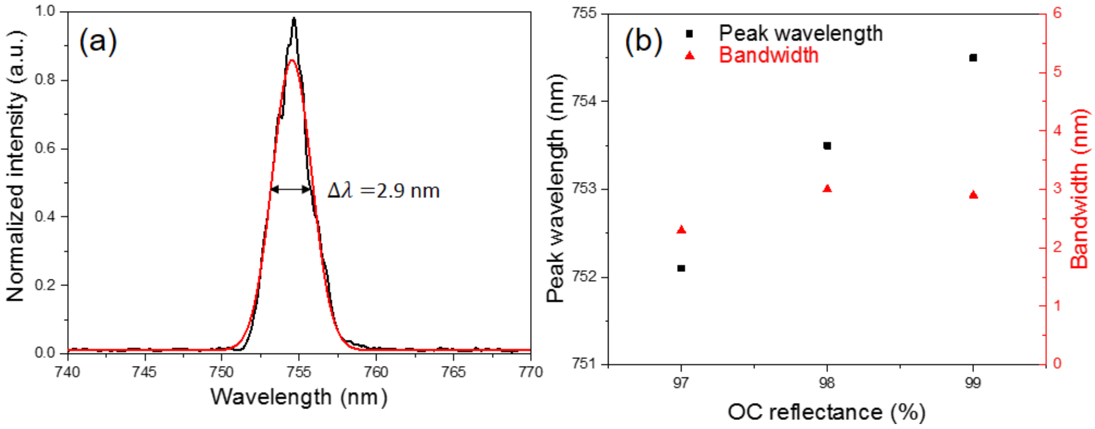

Figure 4.11. (a) The spectrum of the Alexandrite laser with R=99% OC at 43.1 W incident pump power with a peak wavelength of 754.5 nm and a bandwidth of 2.9 nm (FWHM). The red curve is the Gaussian fit to the spectrum. (b) The lasing peak wavelength and bandwidth (FWHM) against OC reflectance at 43.1 W incident pump power.

The spectra of the Alexandrite laser were measured using a spectrometer (Thorlabs CCS200, wavelength range: 200-1000 nm, resolution: < 2 nm FWHM @633 nm). At an incident pump power of 43.1 W, the laser with R=99% OC had a peak wavelength of 754.5 nm with a bandwidth of 2.9 nm (FWHM) deduced from a Gaussian fit to the spectrum, as shown in Figure 4.11 (a). The lasing peak wavelength and bandwidth as a function of OC reflectance under 43.1 W pumping are shown in Figure 4.11 (b). As there were no wavelength control elements in the compact cavity, the peak wavelength was determined by the properties of the Alexandrite crystal and the optical coatings of the cavity elements. The laser GSA is stronger at shorter wavelengths, so the thresholds at these wavelengths are higher. The laser GSA is also stronger at lower population inversions. The peak wavelength increases with the increasing reflectance, as illustrated in Figure 4.11 (b), since the reduced population inversions push the operation to longer wavelength. The CW lasing bandwidth varied from 2.3 to 3.0 nm.

4.3 Actively Q-switched Operation with Diode Pumping

Q-switching is a method for generating energetic laser pulses by modulating the intracavity losses. This section describes the first study of a Q-switched Alexandrite laser under CW diode end-pumping. Previous diode-pumped Q-switched operation of Alexandrite lasers prior to this thesis work was achieved by pulsed pumping [154,187] A motivation for developing such a pulsed laser source with Q-switched and TEM_{00} operation is to address space-borne remote sensing applications, including laser-based LIDAR and altimetry at high pulse rate where CW pumping would be necessary.

A diode-end-pumped Q-switched Alexandrite laser was investigated in this section. For the purpose of achieving the Q-switched operation, the compact cavity of Figure 4.6 was developed into an extended cavity design with the same end mirrors (plane mirrors) and shown in Figure 4.12. The cavity length was 193 mm. A BBO Pockels cell (from Eksma Optics, model: PCB3D) driven by a variable electric voltage was employed to alter the polarisation state of the intracavity radiation and together with a thin film polarizer (from Optida) to provide Q-switching. The rise and fall time (20% and 80% points) of quarter-wave voltage to the BBO pockels cell was measured to be 1.7 ns and 2.4 ns, respectively. The contrast ratio of the thin film polariser is > 200:1. A plano-convex intracavity lens with 100 mm focal length was used to optimise TEM_{00} operation and control cavity stability in the presence of the rod's thermally-induced lensing. The Pockels cell was operated at 2 kV near its quarter-wave voltage. It acts as a quarter-wave plate when the drive voltage is switched on.

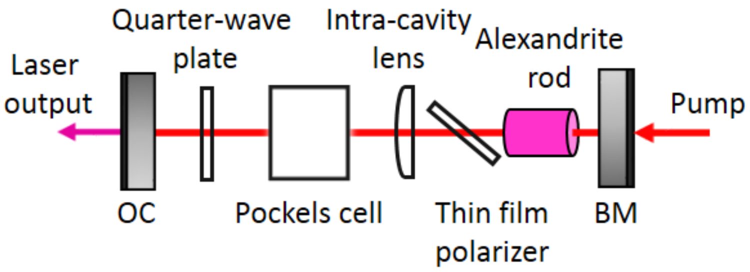

Figure 4.12. Schematic of diode-end-pumped extended Alexandrite laser cavity design for Q-switched operation.

A thin film polarizer was placed in the cavity at the Brewster angle to eliminate the S polarisation component of intracavity radiation and hence improving the polarisation purity. The thin film polarizer was highly reflecting (R>99.5%) for S-polarised light and highly transmitting for P-polarized light at the laser wavelength. The quarter-wave plate was incorporated into the cavity to address the issue of having the voltage on the Pockels cell for a long period. Lasing was inhibited when no voltage was applied to the Pockels cell. Therefore, the high voltage was only needed to be applied for a short period when Q-switching was required, which effectively extended the Pockels cell's lifetime. The quarter-wave plate was designed for 780 nm but capable of meeting requirements at the lasing wavelength. The thin film polarizer and the quarter-wave plate solved the problems mentioned above but at the expense of introducing additional intracvity losses. The inevitable losses reduced the laser output power and extended the build-up time [142]. An output coupler with a reflectance of 97% was used with the intention of reducing the intra-cavity flux, so the laser-induced damage could be avoided at high peak power Q-switched operation.

4.3.1 Realization of Q-switched Operation

A Pockels cell can be used as a voltage-controlled wave plate. It consists of an electro-optic (nonlinear) crystal and electrodes. There are different types of Pockels cells, such as potassium dihydrogen phosphate (KDP) and potassium dideuterium phosphate (KD*P) for the visible-to-near infrared region, or cadmium telluride (CdTe) for the middle-infrared [11], and beta barium oxide (BBO) for the near infrared to the deep ultraviolet.

BBO Pockels cells have many attractive advantages over other crystal based Pockels cells. They have a broad transmission spectral band ~210-2000 nm allowing a wide spectral range. The low piezo-electric ringing enables BBO Pockels cells to effectively handle high repetition rate [189]. Fast switching time in conjunction with low capacitance make them particularly suitable for the Q-switching and cavity dumping. Moverover, BBO crystals have a high threshold for laser damage and a low thermo-optic coefficient. Therefore, a BBO Pockels cell was selected as an electro-optical modulator in our system.

The BBO Pockels cell used is a transverse device – the applied electric field E is perpendicular to the light propagation direction. According to Equation (2.3.16), the quarter-wave voltage is obtained by equating the phase difference $\Delta\phi$ to $\pi/2$, which is given by

$$V_{\frac{\lambda}{4}} = \frac{\lambda d}{4{n_o}^3 r_{22} l} \tag{4.3.1}$$

where n_o is the ordinary refractive index, r_{22} is the electro-optic coefficient, l is the length of the BBO crystal, d is the dimension of the crystal along the direction of the applied voltage. The quarter-wave voltage $V_{\lambda/4}$ is inversely proportional to the crystal aspect ratio (l/d). The transverse design with a large crystal aspect ratio allows the use of a low quarter-wave voltage.

Q-switched operation is achieved via loss modulation. Initially, a BBO Pockels cell and a polarizing beamsplitter were placed in a laser cavity, as shown in Figure 4.12. The BBO Pockels cell had a quarter-wave voltage of < 2.3 kV at 760 nm. The optical transmission at 760 nm was greater than 97%. The cell had a diameter of 2.54 mm and a length of 37.2 mm. An extra quarter-wave plate was introduced in the laser cavity to protect the Pockels cell from long-term working. Without applying the voltage to the Pockels cell, the polarisation is rotated by 90° in a double pass due to the additional quarter-wave plate. The thin film polarizer then rejects the radiation and thus introducing losses into the cavity. With turning the quarter-wave voltage on, the Pockels cell acts as a quarter-wave plate. Under the combined action of Pockels cells and the quarter-wave plate, the polarisation of the intracavity radiation is rotated by 180° (or 0°), which means there is no substantial change in the polarisation state. Thus, the losses are reduced, and the laser action is initiated.

4.3.2 Results of CW Diode-pumped Q-switched Operation

In this study, the Q-switched pulses were demonstrated with pulse repetition rate ranging from 1 to 10 kHz. The frequency range was only limited by the drive electronics. This was the first demonstration of a Q-switched Alexandrite laser under CW diode pumping at the time of the thesis work. Stable Q-switched pulses were obtained throughout this pulse repetition rate range.

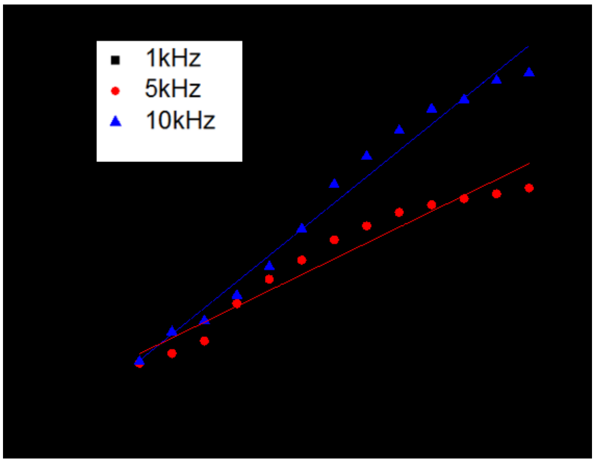

Figure 4.13. The pulse average power against CW diode pump power for Q-switched Alexandrite laser with R=97% output coupler at different pulse repetition rates (1 kHz, 5 kHz and 10 kHz). Lines are linear fits to the power curves.

Figure 4.13 shows the variation of the pulse average power with CW diode pump power for different pulse repetition rates (1 kHz, 5 kHz, and 10 kHz). The highest slope efficiency was 8.24% obtained at 10 kHz producing 1.1 W average output power at 24.8 W incident pump power. For repetition rates of 1 and 5 kHz, the slope efficiencies were 0.95% and 4.97%, respectively. The pump power of the diode module was not fully utilized, because the power curves tended to roll over after increasing the pump power above 24.8 W. In order to evaluate the results of Q-switched operation more intuitively, the pulse average output power was converted to the pulse energy.

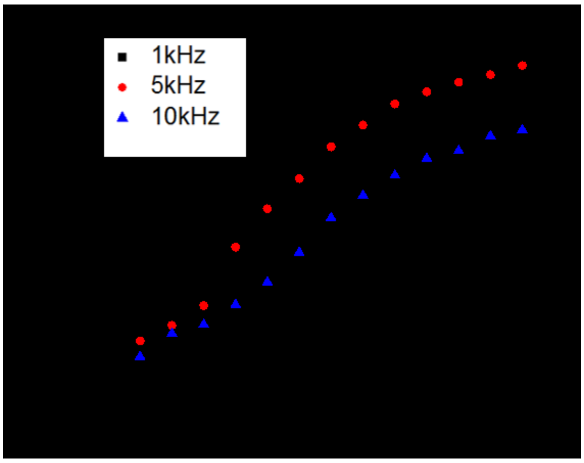

Figure 4.14. The pulse energy against CW diode pump power for Q-switched Alexandrite laser at different pulse repetition rates (1 kHz, 5 kHz and 10 kHz).

Figure 4.14 shows the corresponding pulse energy against CW diode pump power for different pulse repetition rates (1 kHz, 5 kHz and 10 kHz). At 5 kHz, the highest pulse energy of 133.6 µJ with 128 ns pulse duration (FWHM) was obtained at 24.8 W incident pump power, corresponding to a peak power of 1.04 kW. At 10 kHz, 106.0 µJ pulse energy with 177 ns pulse duration was achieved, resulting in a peak power of 0.60 kW. At higher incident pump power (>18 W), the curves for 1 kHz and 5 kHz almost overlap with each other.

As the incident pump power increases, the pulse energy increases but has a tendency to roll over at higher pumping level, which is due to thermal lensing and cavity stability issues; whilst the pulse duration decreases because of the growth of the gain. These lead to a rapid increase in pulse peak power as incident pump power increases, after reaching a characteristic point, the peak power starts to be limited as the energy curve rolls over.

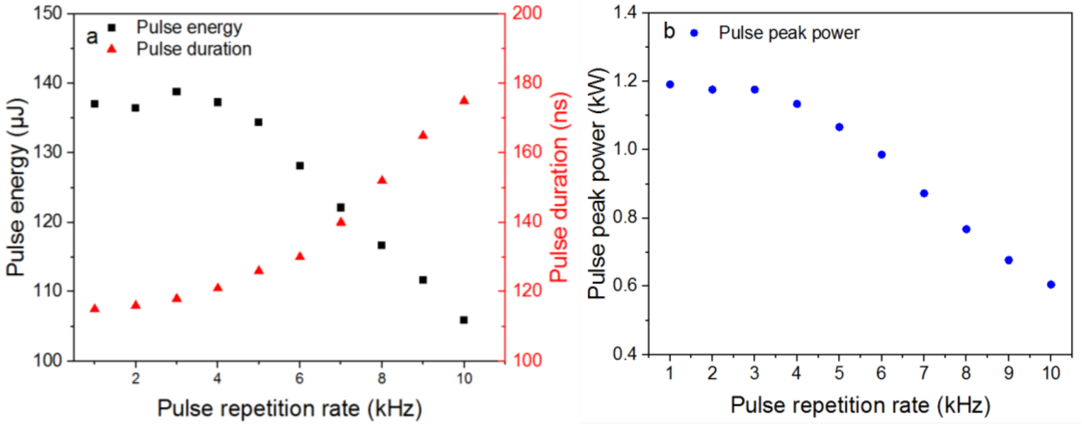

Figure 4.15. (a) The pulse energy and pulse duration against pulse repetition rate for CW diode-pumped Q-switched pulses. (b) The pulse peak power against pulse repetition rate for CW diode-pumped Q-switched pulses.

The pulse energy and pulse duration against pulse repetition rate (from 1 kHz to 10 kHz) is shown in Figure 4.15 (a). The repetition rate was progressively reduced from 10 kHz to 1 kHz, and the data were recorded at the same incident pump power (24.8 W) for each repetition rate. The pulse peak power at different repetition rates can be calculated from the corresponding pulse energy and pulse duration. The pulse energy reduces with the elevated repetition rate above approximately 3 kHz, whilst the pulse duration increases with the elevated repetition rate [157]. Therefore, as the repetition rate increases, the pulse peak power has a tendency to decrease, as shown in Figure 4.15(b). The maximum peak power was 1.19 kW (137.0 μJ pulse energy and 115 ns pulse duration) achieved at 1 kHz, while the minimum one was 0.60 kW (106.0 μJ pulse energy and 177 ns pulse duration) obtained at 10 kHz.

The reason why pulse energy rapidly drops with the elevated pulse repetition rate after 3 kHz is stated as follows: The energy storage is limited to the upper state lifetime (~260 μs at room temperature) of Alexandrite, which corresponds to ~3.8 kHz in the frequency domain. Therefore, the Q-switched pulse repetition frequency can be increased to ~3.8 kHz without significantly reducing the pulse energy. When the pulse repetition frequency exceeds this characteristic frequency (~3.8 kHz), the pulse energy decreases as the repetition frequency increases. Due to the high frequency, the population inversion cannot recover to its maximum possible value between each pulse emission.

The spatial beam quality M^2 parameter for the Q-switched output mode was measured at different repetition rates, as listed in Table 4 below,

Table 4. M^2 for the Q-switched output at various pulse repetition rates.

Pulse repetition rate	M^2_x (Horizontal)	M^2_y (Vertical)
1 kHz	1.04	1.03
5 kHz	1.15	1.15
10 kHz	1.18	1.32

The results illustrate that the beam quality is very good but there is some degradation as the repetition rate increases. At 1 kHz, both the M^2_x and M^2_y are close to unity, which indicates an almost ideal TEM_{00} mode. Figure 4.16 (a) shows the focused caustic for the Q-switched output at 5 kHz repetition rate and 24.8 W incident pump power. Figure 4.16 (b) shows the spatial mode profile at 5 kHz repetition rate. The beam had a near-diffraction-limited TEM_{00} mode with M^2 of 1.15 in both x and y directions. Astigmatism presented in the laser beam was caused by the asymmetric pump size. Figure 4.16 (c) shows beam cross sections and beam width measurements of the spatial mode profile in X and Y directions, the beam has a diameter ($1/e^2$) of 120µm and 132µm.

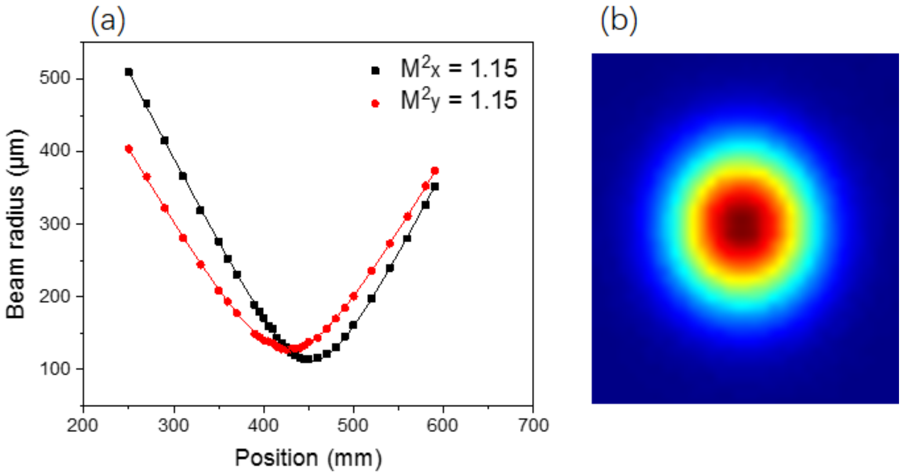

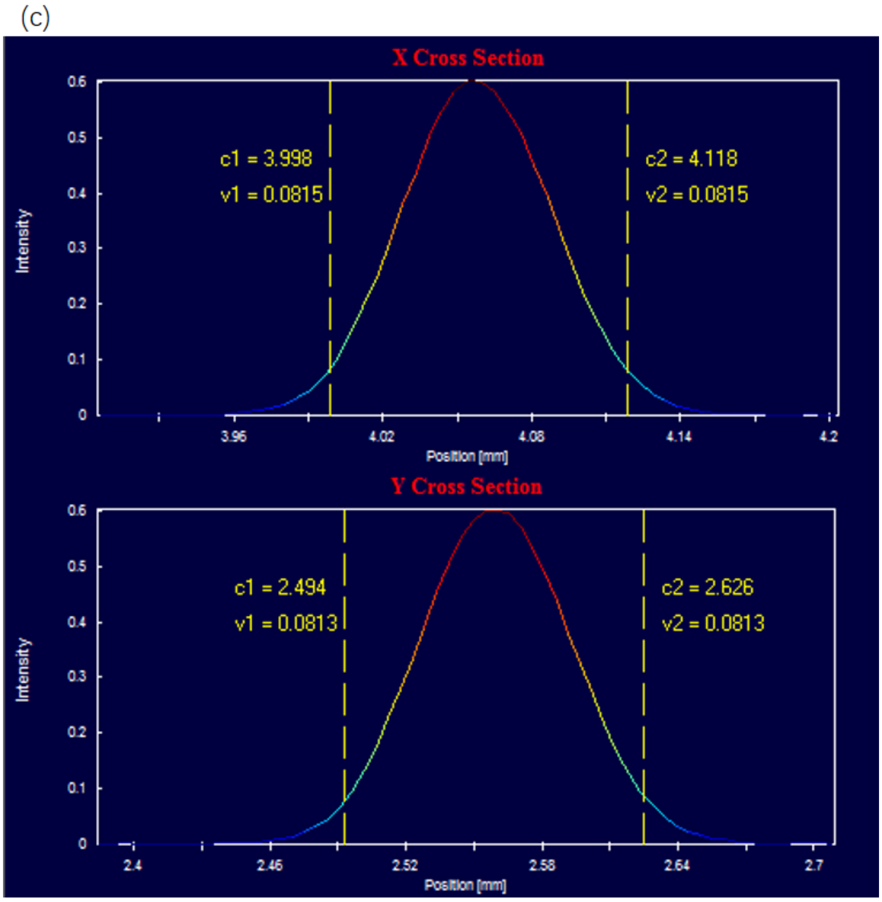

Figure 4.16. (a) M^2 caustic fit for the Q-switched output at 5 kHz repetition rate and 24.8 W incident pump power. (b) Spatial mode profile of the Q-switched output at 5 kHz and 133.6 μJ pulse energy. (c) Cross sections and beam width measurements ($1/e^2$) of the spatial mode profile in X and Y directions.

4.4 Cavity-dumped Q-switched Operation

Cavity dumping is a method for producing short laser pulses involving Q-switching the laser with cavity mirrors that are highly-reflecting at the laser wavelength. The output coupling is set to the maximum between pulses to frustrate lasing. Then the cavity is completely closed, and the intracavity radiation builds up in a low-loss resonator. The output coupling is switched again to maximum when the intracavity Q-switched pulse has reached its maximum intensity, which allows rapid dumping of the entire optical energy from within the cavity [190]. Cavity dumping allows the energy stored in the cavity to be coupled out in a time scale in principle equal to a single round-trip time.

Therefore, providing the switching process is fast enough, the pulse duration is primarily related to the cavity length rather than the gain characteristics of the laser medium [7].

Shorter pulses would be beneficial for applications requiring high precision. For example, altimetry requires short pulses to offer high-resolution measurements. Furthermore, pulses with shorter duration possess higher peak power for given pulse energy, which is useful for improving the efficiency of nonlinear optical processes. The motivation for developing a cavity-dumped Q-switched Alexandrite laser source is to generate short laser pulses with few nanoseconds duration at high repetition rates for harmonic generation and LIDAR applications requiring high ranging precision.

The performance of a cavity-dumped Q-switched Alexandrite laser under CW diode pumping was investigated in this section. Figure 4.17 shows an extended diode-end-pumped laser cavity used for the cavity-dumped operation. It is a modified version of the Q-switched Alexandrite laser cavity (see Figure 4.12). The output coupler in this configuration is replaced by a highly reflecting mirror at laser wavelength (~755 nm). Output coupling is time-varying and provided by cavity-dumping from the thin film polarizer. The cavity length was 190 mm, corresponding to a cavity round-trip time of 1.3 ns.

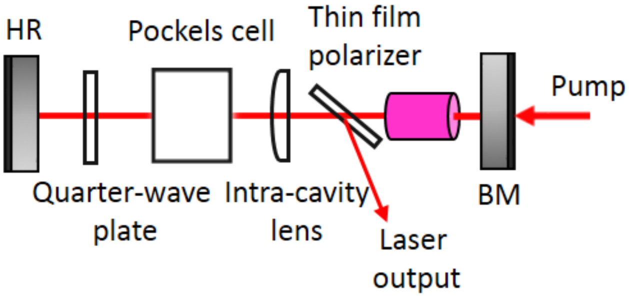

Figure 4.17. Schematic of a cavity-dumped Q-switched Alexandrite laser under CW diode pumping.

4.4.1 Realization of Cavity-dumped Q-switched Operation

The idea for realizing cavity-dumped Q-switched operation is to keep the optical losses of the cavity as low as possible for a short time, allowing a Q-switched laser pulse rapidly build up, and then dump the energy contained in the cavity by extracting a pulse within about one cavity round-trip time [7,190,191]. Specifically, in combination with a quarter-wave plate, the BBO Pockels cell is initially kept in the voltage-off state where most of the intracavity flux is coupled out by the thin film polarizer. Lasing is inhibited since the population inversion is below the threshold level. The Pockels cell is then switched to the voltage-on state, so radiation circulates in the cavity and experiences low losses, which results in the fast build-up of the intracavity flux. Finally, the Pockels cell is rapidly switched to the voltage-off state (cavity-dumped state), ideally when the intracavity flux reaches its maximum value. If the switch is fast enough, the cavity radiation will be extracted within around one round-trip time in the form of a short pulse. In practice, the pulse duration is dependent on both the cavity round-trip time and the switching time of the Pockels cell.

4.4.2 Results of Cavity-dumped Q-switched Operation

Initially, a mirror with a reflectance of 97% was employed as one of the cavity mirrors to protect the optics from damage caused by high intracavity flux. The laser system was operated in Q-switched mode under CW pumping and progressively transitioned to cavity dumped operation by reducing the voltage-on time of the Pockels cell. There were considerable outputs from both the R=97% cavity mirror and the thin film polarizer. However, the output from the R=97% cavity mirror is considered to be a loss for the cavity-dumped Q-switched operation.

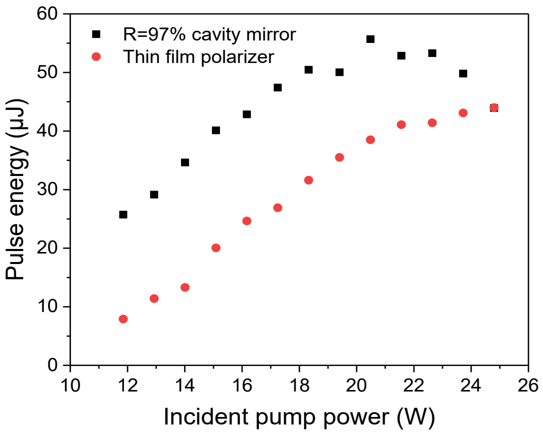

Figure 4.18. The cavity-dumped Q-switched pulse energy against incident pump power for pulses from the thin film polarizer and the R=97% cavity mirror, at 5 kHz repetition rate.

Figure 4.18 shows the results of cavity-dumped Q-switched pulse energy as a function of incident pump power for pulses from the thin film polarizer at 5 kHz repetition rate and simultaneously from the R=97% cavity mirror. For the pulses obtained from the R=97% mirror, the pulse energy increases until reaching a peak of 55.7 μJ at 20.5 W incident pump power, since then the pulse energy drops down. As the incident pump power increases, the pulse energy of the pulses extracted from the thin film polarizer steadily increases and then tends to roll over at higher pumping levels. The highest pulse energy was 44.0 μJ obtained at 24.8 W incident pump power. The pulse duration was 2.9 ns measured using a 70 ps rise-time photodiode. Therefore, pulses of 15.2 kW peak power were achieved at 5 kHz repetition rate for the cavity-dumped Q-switched Alexandrite laser with R=97% cavity mirror. The peak power is more than ten times that of the standard Q-switched pulses.

The repetition rate was then increased to 10 kHz to investigate laser performance at higher repetition rates. Figure 4.19 depicts the pulse energy against incident pump power for pulses from thin film polarizer and R=97% cavity mirror.

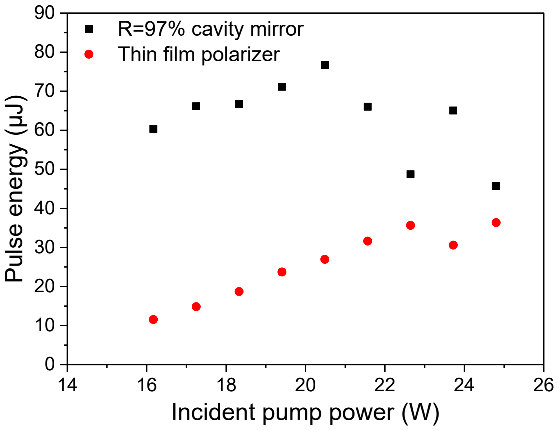

Figure 4.19. The cavity-dumped Q-switched pulse energy against incident pump power for pulses from the thin film polarizer and the R=97% cavity mirror, at 10 kHz repetition rate.

As the incident pump power increases, the pulse energy obtained from the R=97% cavity mirror increases until it reaches a peak of 76.1 μJ pulse energy (at 20.5 W incident pump power). From then on, the pulse energy fluctuates. For the pulses emitted from the thin film polarizer, the pulse energy increases with the incident pump power, except for a single point at 23.7 W incident pump power. This dip seems to correspond to the sudden increase in pulse energy at the same incident pump power for the pulses obtained from the R=97% cavity mirror. The highest pulse energy of 36.4 μJ with 2.9 ns pulse duration was achieved at 24.8 W incident pump power, corresponding to a peak power of 12.6 kW.

Overall, for the pulses obtained from the thin film polarizer, the pulse energy at 5 kHz repetition rate is higher than that at 10 kHz under the same pumping condition. Because when the repetition rate is greater than the characteristic frequency, the pulse energy decreases as the repetition rate increases, as discussed in Section 4.3.2. As a result, the highest peak power (15.2 kW) obtained at 5 kHz is 21% larger than that (12.6 kW) achieved at 10 kHz.

Further investigation was conducted with a HR mirror rather than the R=97% cavity mirror, thereby reducing the cavity loss and enhancing the cavity dumped pulse energy obtained from the thin film polarizer. The HR mirror was highly-reflecting (R>99.9%)

at laser wavelength (~755nm). Ideally, no output can be detected from the HR mirror when the Pockels cell and the thin film polarizer are properly oriented.

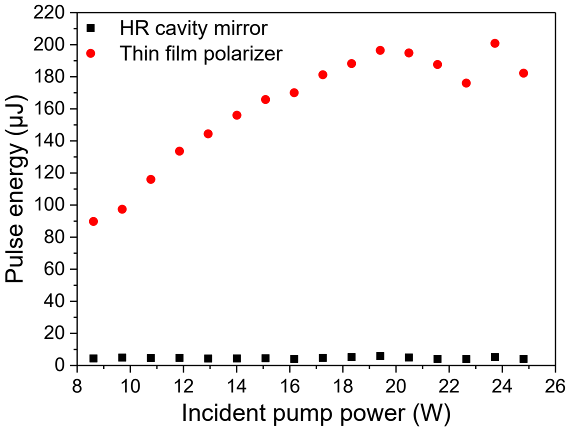

Figure 4.20. The cavity-dumped Q-switched pulse energy against incident pump power for pulses from the thin film polarizer and the HR mirror, at 5 kHz repetition rate.

Figure 4.20 displays the results of the pulse energy against incident pump power for pulses emitted from the thin film polarizer and the HR mirror at 5 kHz repetition rate. The pulse energy from the HR mirror is negligible compared to that from the cavity-dumped output at the thin film polarizer. As the incident pump power increases, the pulse energy from the HR mirror levels off. Whereas the pulse energy from the thin film polarizer first rises to a peak (196.4 μJ pulse energy at 19.4 W incident pump power). It then fluctuates and reaches a maximum of 200.8 μJ at 23.7 W incident pump power. The pulse duration was 2.9 ns (FWHM). At 5 kHz repetition rate, the highest cavity-dumped peak power achieved with the HR mirror cavity was 69.2 kW. This value is almost five times that of cavity dumped Q-switching with R=97% cavity mirror and more than sixty-times that of the standard Q-switched operation. Therefore, the cavity dumped Q-switching considerably reduced the pulse duration and improved the pulse energy, resulting in an immense improvement in the peak power.

4.5 Summary

This chapter has presented results from diode-end-pumped Q-switched Alexandrite lasers. Two laser-diode modules (a free-space laser module and a fiber-coupled one) were employed as pump lasers in this theis work, and their properties are presented at the beginning of this chapter. Compared to the fiber-coupled laser module, the free-space one has high power output, high polarisation purity, but low beam quality. The free-space laser module was used as the pump for actively Q-switched operation. The output was spatially redistributed using a beam shaping system due to the highly multimode output along the slow axis.

Prior to the Q-switched operation, the performance of a high-efficiency Alexandrite laser under CW pumping was characterized in terms of the threshold, output power, efficiency, peak wavelength and spectral bandwidth. The Alexandrite laser using an R=98% output coupler produced 17.1 W output power with a slope efficiency of 45.6% at the pump power of 43.1 W. It is noted that the peak wavelength of the output increased with the reflectance of output couplers because of the laser GSA effect.

The Q-switched operation was achieved using a BBO Pockels cell. The laser was operated at pulse repetition rates between 1 and 10 kHz, which is the first demonstration of a Q-switched Alexandrite laser under CW diode pumping. The pulse repetition rate was limited to the inverse of the Alexandrite's upper state lifetime (260 μs). This means the pulse repetition rate can be increased to ~3.8 kHz without pulse energy reduction. After exceeding this characteristic frequency, the pulse energy dropped down. The peak power was found to decrease with increasing repetition rate. The maximum peak power of 1.19 kW was achieved with 137.0 μJ pulse energy and 115 ns pulse duration at 1 kHz repetition rate.

Cavity dumping was implemented to eliminate the limitation of the standard Q-switching pulse width (115 ns) and to generate shorter pulses with few nanoseconds duration (2.9 ns FWHM). The cavity-dumped Q-switched operation considerably reduced the pulse duration and improved the pulse energy, resulting in a significant improvement in the peak power. The highest peak power of 69.2 kW (200.8 μJ pulse energy and 2.9 ns pulse duration) at 5 kHz repetition rate demonstrated from the Q-switched cavity-dumped operation is more than 60 times that of the standard Q-switching.

The thesis work presented in this chapter represents the first Q-switched operation in an Alexandrite laser under CW diode pumping. The results represent the highest ever pulse repetition rates from Alexandrite up to 10 kHz. The 2.9 ns duration pulses obtained from the cavity dumped Q-switched operation are the shortest non-mode-locked pulses produced from Alexandrite. The short pulses possessing high repetition rate generated from cavity-dumped Alexandrite lasers provide a valuable resource for LIDAR and altimetry applications.

Chapter 5

SESAM Passively Q-switched Alexandrite Lasers

In addition to active Q-switching, passive Q-switching is another technique for obtaining energetic short pulses. Passive Q switching is simple and cost-effective as compared with active Q-switching. Although the pulse energies are typically lower, passive Q-switching is more suitable for very high repetition rate operation.

This chapter focuses on the developments of diode-pumped passively Q-switched Alexandrite lasers. The passively Q-switched operation was achieved using a semiconductor saturable absorber mirror (SESAM). In addition, the wavelength tunability of the passively Q-switched system was investigated using a birefringent filter (BiFi) tuning element. As a precursor study, a compact linear diode-end-pumped Alexandrite laser was investigated to explore the output power and efficiency potential. A wavelength-tunable X-cavity Alexandrite laser under diode pumping was then developed and characterized. After replacing the back mirror with the SESAM, passively Q-switched operation was successfully demonstrated with the diode-pumped X-cavity Alexandrite laser. Some of the results in this chapter have contributed to one published journal article [159].

5.1 Compact Diode-end-pumped Alexandrite Laser

Figure 5.1 shows the compact diode-end-pumped CW Alexandrite laser with a Brewster-angle cut crystal. The pump module used was the fiber-coupled red diode laser described in Section 4.1.2. Although the fiber-coupled diode module produces less output power than the free-space one, it can generate a circularly symmetrical pump beam with better beam quality. The gain medium doped with 0.22% of Cr^{3+} was a *c*-cut Alexandrite rod with Brewster-angled end faces. It had a length of 8 mm and a diameter of 4 mm. The absorption coefficient of the Alexandrite rod was measured to be 6.6 cm^{-1}. The Alexandrite rod was contacted with indium foil and embedded in a water-cooled copper heat sink. It was mounted with its b-axis orientated horizontally in a plane-plane mirror cavity. The laser cavity was formed of two plane mirrors: a dichroic back mirror (BM) which was highly-transmitting for the pump and highly-reflecting at the laser wavelength and an output coupler (OC) with a reflectance of 98.8% at the laser wavelength. The temperature of the water-cooled copper heat sink for the crystal was maintained at 40°C.

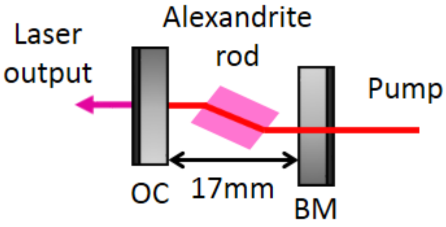

Figure 5.1. Schematic of the compact diode-pumped CW Alexandrite laser with linear cavity. BM is a dichroic back mirror, OC is an output coupler with R=98.8%.

5.1.1 Pump Delivery System

The pump delivery system for the Alexandrite laser is shown in Figure 5.2. An aspheric fiber collimator with a focal length of 35 mm was used to collimate the output from the fiber-coupled diode module. As the fiber delivery scrambles the polarisation of the pump laser, the polarisation purity of the pump laser is only 70%. The linearly polarised power (70%) was rotated by a half-wave plate to match the high absorbing b-axis of the Alexandrite laser. An aspheric lens with a focal length $f_p = 50$ mm then focused the pump beam to a spot on the pump face of the crystal. The focal length of the aspheric lens was determined by balancing the following two points: 1. A relatively small pump beam waist enabling a high pump intensity; 2. A relatively large pump beam waist providing a pump beam with small divergence over the absorbed path. The aspheric lens with f_p = 50 mm provided a beam waist diameter of 140 μm and a confocal parameter of 1.1 mm.

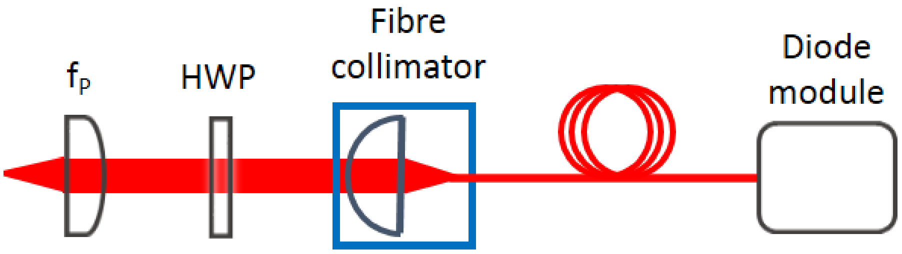

Figure 5.2. Schematic of the pump delivery system for the Alexandrite laser. Diode module is a fiber-coupled red diode laser. Fiber collimator is an aspheric lens with focal length of 35 mm. HWP is a half-wave plate. f_p is an aspheric lens with focal length of 50 mm.

5.1.2 Results of Compact Diode-pumped Alexandrite Laser

The most efficient operation was achieved by optimising the cavity length to alter the cavity mode size and adjusting the location of the pump beam waist with the aspheric pump lens (f_p) to achieve mode matching condition, which results in a cavity length of 17 mm.

Figure 5.3 (a) shows the results of the output power of the compact Alexandrite laser against incident pump power on the crystal. The slope efficiency was 28.0% producing 1.1 W output power at the maximum pumping level of 5.3 W, corresponding to an optical-to-optical conversion efficiency of 20.8%. The laser threshold for the system with the R=98.8% OC was 1.4 W. It is noted that only ~70% of the pump power parallel to b-axis of Alexandrite is absorbed. The slope efficiency is therefore closer to 40% with respect to absorbed pump power. The graphs in subsequent sections are also with respect to incident pump power, and the same scaling would apply.

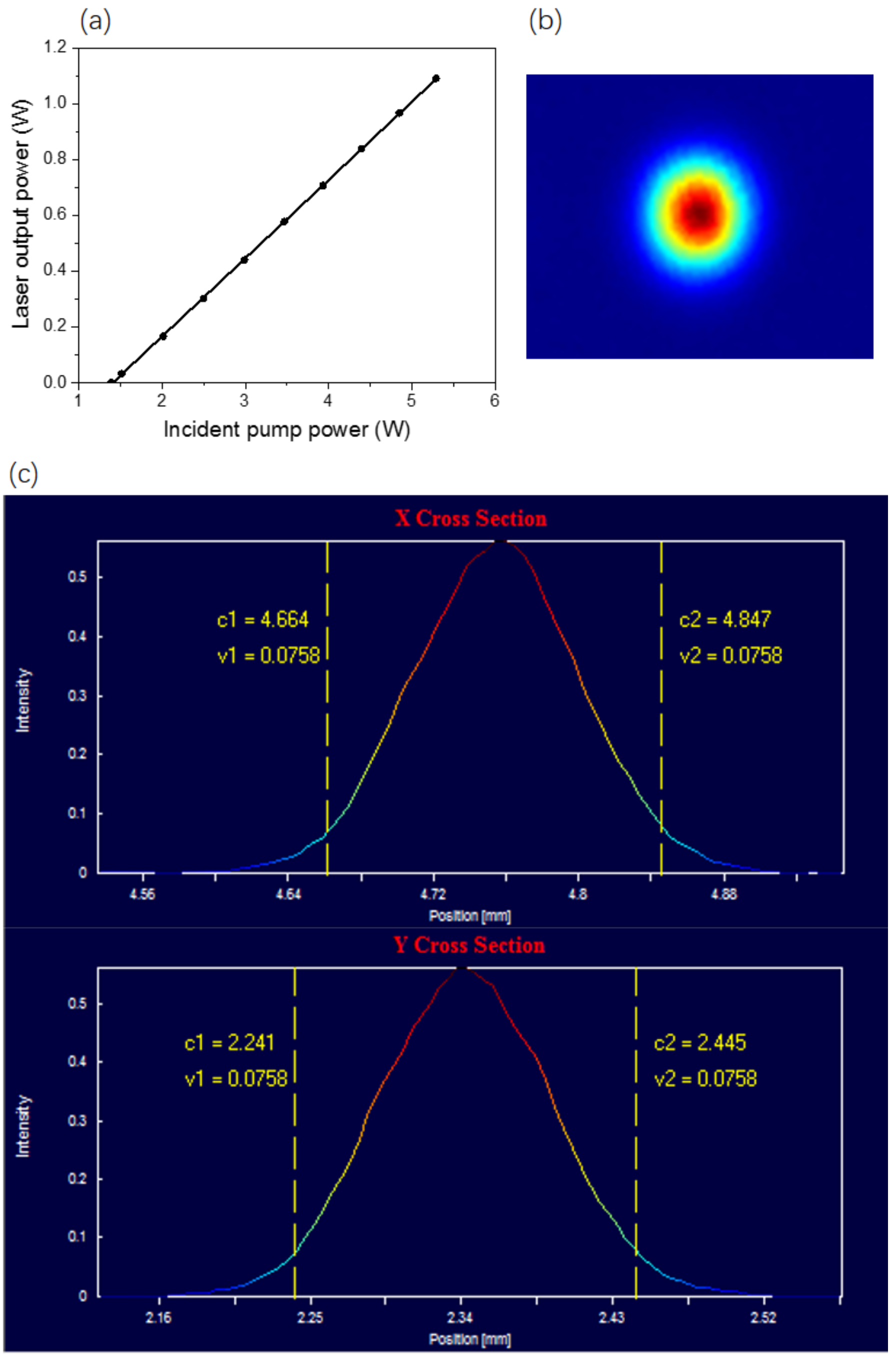

Figure 5.3. (a) The laser output power against incident pump power for the compact Alexandrite laser with R=98.8% OC. Line is linear fit to the power curve. (b) Spatial mode profile of the output beam with $M^2 < 1.1$ at 1.1 W output power. (c) Cross sections and beam width measurements ($1/e^2$) of the spatial mode profile in X and Y directions.

Figure 5.3 (b) shows the spatial profile of the laser output. The laser beam had a TEM_{00} beam profile with M^2_x=1.07 and M^2_y=1.03 at the emission wavelength of 756 nm. The laser beam size at the output coupler was investigated by using a relay-imaging system formed by a pair of f=200 mm lenses onto a CMOS camera. The laser beam was measured to be a diameter ($1/e^2$) of 183 µm (x) by 204µm (y), as shown in Figure 5.3 (c). The ellipticity of the laser beam was induced by the Brewster-angle cut crystal, as the Brewster faces induce astigmatism. The astigmatic properties of the Brewster-angle cut crystal and curved mirrors used in subsequent X-cavity Alexandrite lasers and a method to compensate the astigmatic distortions are discussed in more detail in Section 5.2.

5.2 Astigmatic Compensation

A 4-mirror X-shaped laser cavity with two folded arms requires oblique angles of incidence at cavity mirrors. The cavity mirrors used at oblique angles introduce astigmatism into the system. The Brewster-cut crystal used in the cavity also causes astigmatism. However, astigmatism introduced by the mirrors and the crystal can be used to compensate for each other. Firstly, the astigmatic properties of the curved mirrors and the Brewster-angle cut crystal are investigated in this section.

5.2.1 Astigmatic Properties

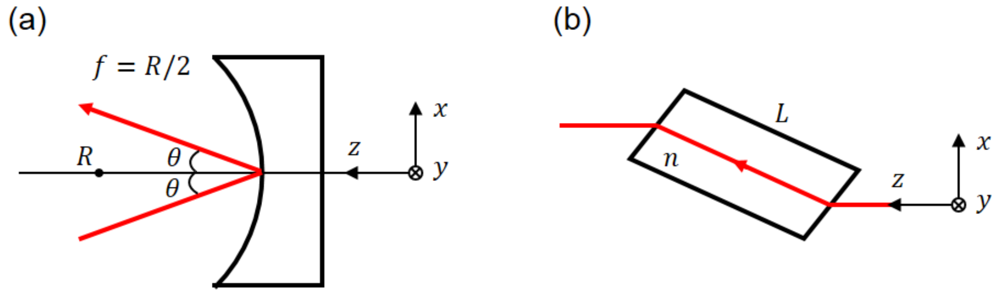

Figure 5.4. (a) A curved mirror with beam incident at an oblique angle. (b) A Brewster-cut gain medium with beam incident at Brewster's angle. Coordinates used in analysis are indicated.

A curved mirror with a radius of curvature of R has a focal length $f = R/2$, if the incident beam axis is normal to the mirror surface. If the curved mirror is used at an oblique angle (see Figure 5.4 (a)), it will focus ray bundles in x and y directions differently with two different effective focal lengths f_x and f_y. The focal lengths f_x and f_y are related to the incidence angle and the focal length f, given by [192]

$$f_x = f cos\theta = \frac{R cos\theta}{2} \tag{5.2.1}$$

$$f_y = \frac{f}{cos\theta} = \frac{R}{2cos\theta} \tag{5.2.2}$$

where θ is the incidence angle as shown in Figure 5.4 (a), f is the focal length of the mirror with the radius of curvature of R.

Brewster-angle faces also act differently on ray bundles in x and y directions. A beam traveling through a gain medium that is inclined at Brewster's angle with respect to the propagation direction experiences different lengths in the x and y directions. For a gain medium with a length of L, shown in Figure 5.4 (b), the effective length L_x and L_y are given by

$$L_x = \frac{L\sqrt{n^2+1}}{n^2} \tag{5.2.3}$$

$$L_y = \frac{L\sqrt{n^2+1}}{n^4} \tag{5.2.4}$$

Where n is the refractive index of the gain medium.

5.2.2 Implementation of Astigmatic Compensation

For the sake of simplicity, we first consider a 3-mirror folded cavity (see Figure 5.5 (a)) including two astigmatic elements – a curved mirror (M_2) and a Brewster-angle cut gain medium.

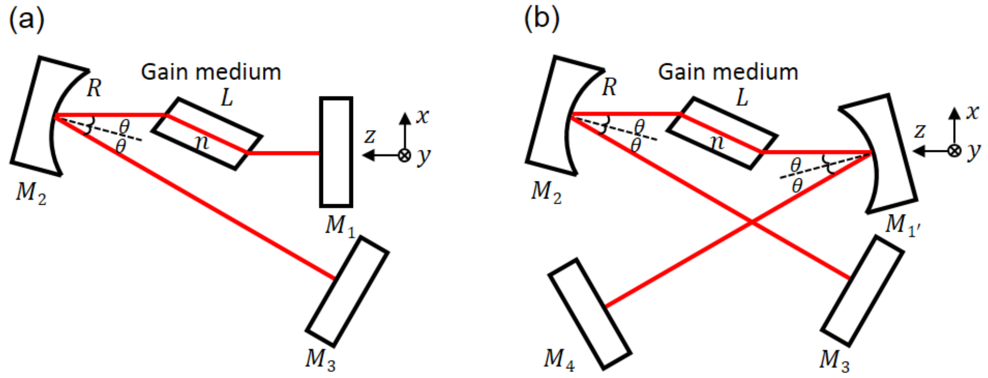

Figure 5.5. (a) Schematic of a folded cavity with 3 mirrors and a Brewster-cut crystal. (b) Schematic of an X-shaped cavity with 4 mirrors and a Brewster-cut crystal.

Astigmatic compensation is implemented by producing a maximum overlap between the stability range in x and y directions, which yields the following equation [192]

$$f_x - f_y = L_x - L_y \tag{5.2.5}$$

The substitution of Equations (5.2.1) - (5.2.4) into Equation (5.2.5) gives

$$R\ sin\theta\ tan\theta = \frac{2L(n^2-1)\sqrt{n^2+1}}{n^4} \tag{5.2.6}$$

4-mirror X-shaped cavity (see Figure 5.5 (b)) including two curved mirrors and a Brewster-cut gain medium, Equation (5.2.6) is rewritten as

$$R\ sin\theta\ tan\theta = \frac{L(n^2-1)\sqrt{n^2+1}}{n^4} \tag{5.2.7}$$

Compared with Equation (5.2.6), a factor of 2 is lost in Equation (5.2.7) since each curved mirror is responsible for compensating half the length of the gain medium. Equation (5.2.7) indicates that astigmatic compensation can be achieved by selecting the radius of curvature (R) of the mirrors and the incidence angle (θ) for a Brewster-cut crystal with a given length.

Equation (5.2.7) was numerically solved to determine the required parameters, the results of the incidence angle against the length of the Alexandrite crystal for curved mirrors with 50, 75 and 100mm radii of curvature are shown in Figure 5.6.

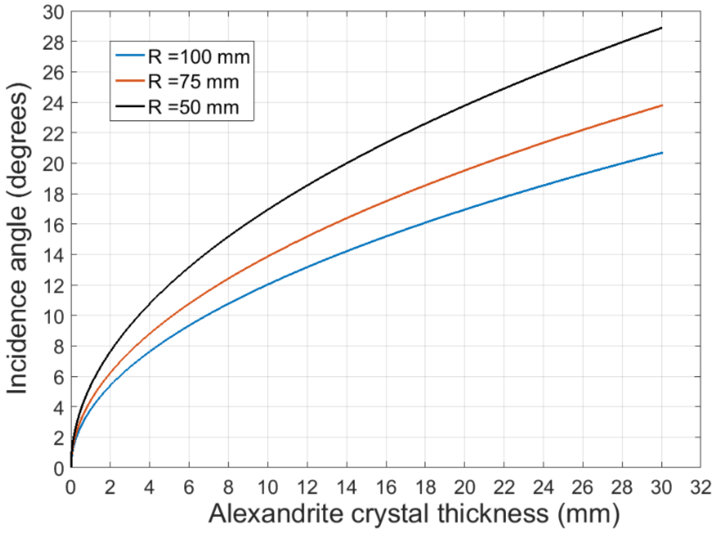

Figure 5.6. The incidence angle of the curved mirrors as a function of the length of the Alexandrite crystal (n=1.74) for radius of curvatures of 50, 75 and 100 mm for the astigmatic compensated X-shaped cavity.

The amount of astigmatism increases with the crystal length, hence requiring a larger incidence angle to achieve astigmatic compensation. For an Alexandrite crystal with a given length, curved mirrors with a longer radius of curvature require a smaller incidence angle to compensate astigmatism.

5.3 Astigmatic Wavelength Tunable X-cavity Alexandrite Laser

This section describes an attempt at configuring a diode-pumped X-cavity Alexandrite laser for wavelength tunable operation. Figure 5.7 shows the pump delivery system for the Alexandrite laser. The f_p = 50 mm aspheric pump lens in Figure 5.2 was replaced with an aspheric lens with focal length $f_{p'}$ = 100 mm. This is with the intention of providing more space between the pump lens and the crystal to accommodate a curved cavity mirror. Doubling the focal length of the pump lens doubles the pump beam waist size. In order to maintain the pump beam waist diameter at 140 µm, a two-element telescope system (f_1 = -100mm and f_2 = 200mm) was introduced to magnify the pump beam by a factor of two at the pump lens.

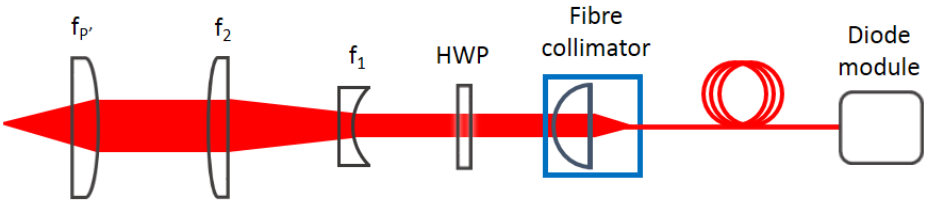

Figure 5.7. Schematic of the pump delivery system for the X-cavity Alexandrite laser. f_1 (-100 mm) and f_2 (200 mm) forms a two-element telescope system to double the size of the pump beam. $f_{p'}$ is an aspheric lens with focal length of 100 mm.

The cavity geometry of the tunable X-shaped diode-pumped CW Alexandrite laser is shown in Figure 5.8. A pair of curved mirrors both with the radius of curvature of R=100 mm was used to form the X-shaped cavity. According to Figure 5.6, the folding angles (θ_1, θ_2) of these mirrors was selected as $\theta_1 = \theta_2 = 22°$ to compensate the astigmatic distortions introduced by the curved mirrors and the crystal. The curved mirrors (CM_1 and CM_2) were highly-transmitting for pump and highly-reflecting at the laser wavelength. The angled pump-through mirror (CM_1) with a plano-concave substrate acted as an astigmatic negative lens that increased the pump size and negatively impacted the pump beam M^2 quality. The temperature of the water-cooled copper heat sink for the crystal was decreased from 40°C to 20°C to improve the beam stability, as the vibration of the laser beam caused by thermal effect was detected by the CMOS camera. The temperature of the red diode pump module was maintained at 16°C.

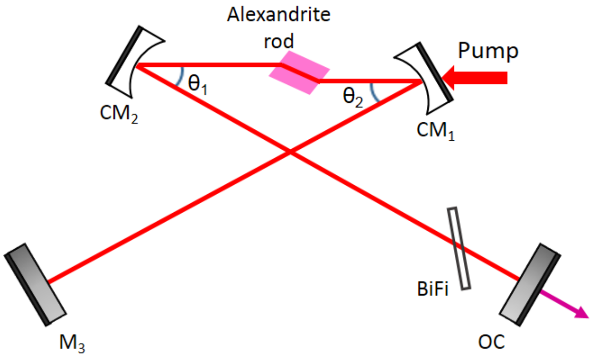

Figure 5.8. Schematic of the tunable diode-pumped CW X-cavity Alexandrite laser. CM_1 and CM_2 are curved mirrors with 100mm radius of curvature. M_3 is a HR mirror for laser. OC is an output coupler. BiFi is a birefringent filter tuner used for wavelength tuning.

To investigate the wavelength tunability of the X-cavity Alexandrite laser, a quartz birefringent filter (BiFi) tuner with a thickness of 0.5 mm and a free spectral range ($\Delta\lambda$) of 130 nm was inserted in the output coupler arm. The BiFi was aligned to sit at Brewster's angle. Wavelength tuning was achieved by rotating the BiFi plate about its surface normal via a goniometer. The principle of wavelength tuning through the use of a BiFi plate is described in greater detail in Section 5.3.1, along with other methods for achieving wavelength tuning.

5.3.1 Birefringent Filter Wavelength Tuning

To study the wavelength tuning properties of Alexandrite lasers, it is important to select a suitable method to tune the laser wavelength away from the center of the gain linewidth. Alexandrite as a broadband gain medium allows a relatively wide tuning range [45,46]. For a wide variety of applications, it is necessary to employ a wavelength selective element to tune the laser wavelength across the entire available gain spectrum. An external feedback grating in Littrow configuration has been used for the wavelength tuning of an Alexandrite laser [154]. Wavelength tuning is realized by adjusting the angle of the grating since for a given angle there exists a specific wavelength reflected back into the laser cavity. However, the tuning range is limited by self-seeding strength. Alternatively, a Brewster angle prism has also been used for wavelength tuning as it has low insertion losses which is significant for a low gain medium such as Alexandrite [45]. Also, the high damage resistance of the prism enables various applications of Alexandrite requiring high peak power. Wavelength tuning is achieved by prism rotation. Similar to the grating, for a given angular setting of the prism, there is a specific wavelength reflected back into the cavity. The Brewster angle prism could extend the tuning to a wider range, but the bandwidth is significantly broader.

Because of the linearly polarised emission of Alexandrite lasers, a birefringent filter (BiFi) inclined at Brewster's angle has been extensively used as a wavelength-selective element [30,37,45,46,155,159] The BiFi has low insertion losses and high damage resistance. A narrow linewidth (~0.1 nm) could be easily achieved using the BiFi within the Alexandrite laser cavity.

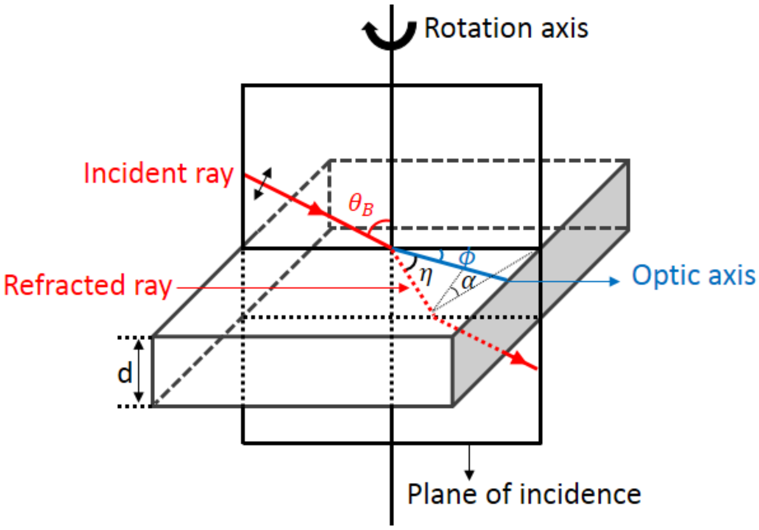

Figure 5.9. A birefringent filter plate used as a wavelength tuning element for the Alexandrite laser.

Figure 5.9 displays the schematic diagram of the BiFi used for the Alexandrite laser. It was a plate of quartz birefringent crystal with thickness d. The incoming P-polarised ray is incident on the plate surface at Brewster's angle (θ_B). The optic axis of the BiFi plate is in a plane parallel to the surface plane, whilst the rotation axis is perpendicular to the surface plane. The angle ϕ is the angle between the plane of incidence and the plane containing the optic axis and the rotation axis. The angle between the optic axis and the refracted ray traveling inside the plate is η. The angle α is the angle between the plane of incidence and the plane containing the optic axis and the refracted ray. The relations among these angles are shown in the following equations

$$cos\eta = cos\phi\ cos\theta_B \tag{5.2.8}$$

$$tan\phi = tan\alpha\ sin\theta_B \tag{5.2.9}$$

When the BiFi plate is rotated about th axis shown in Figure 5.9, the change of the angle ϕ results in the changes of the angle η and α [193].

As the refracted ray is not propagating along the optic axis, the polarisation is projected as two components – ordinary and extraordinary. The two polarisation components experience different refractive indices and different phase shifts as they pass through the BiFi plate. The difference in phase shifts is given by

$$\Delta\delta = \frac{2\pi(n_e - n_o)d\, sin^2\eta}{\lambda\, sin\theta_B} \tag{5.2.10}$$

where λ is the wavelength, n_o and n_e are the ordinary and extraordinary refractive indices, respectively. The phase difference $\Delta\delta$ is a function of wavelength λ. For each $\Delta\delta$ which is an integer multiple of 2π, there is a peak transmission wavelength which is given by

$$\lambda = \frac{(n_e - n_o)d\, sin^2\eta}{k\, sin\theta_B} \tag{5.2.11}$$

where k is an integer. For these wavelengths, the BiFi plate acts as a full waveplate. The incident ray with these wavelengths will be fully transmitted, as the polarisation state remains unchanged (P-polarised) after passing through the BiFi plate. All other wavelengths will suffer the loss when exiting the Brewster surface of the plate since the polarisation is shifted by the plate. Therefore, wavelength tuning is achieved by rotating the BiFi plate about the rotation axis, because this gives rise to the change of η through Equation (5.2.8) and hence the change of the peak transmission wavelength λ through Equation (5.2.11).

In principle, the tuning range of the BiFi plate is larger than the gain bandwidth of the medium. Assuming the variation of $(n_e - n_o)$ over the wavelength range of interest is negligible, the free spectral range of the BiFi plate is given by

$$\Delta\lambda = \frac{\lambda^2 sin\theta_B}{(n_e - n_o)d\, sin^2\eta} \tag{5.2.12}$$

According to Equation (5.2.12), the available wavelength tuning range is related to the plate thickness. The thinner the BiFi plate, the wider the available tuning range and the broader the bandwidth of the transmission peaks [11]. However, multiple BiFi plates whose thicknesses vary by integer ratios can be used to achieve narrow bandwidths [194].

5.3.2 Results of Wavelength Tunable Alexandrite Laser

The laser output power against incident pump power for the wavelength tunable X-cavity Alexandrite laser at the emission wavelength of 759 nm was depicted in Figure 5.10.

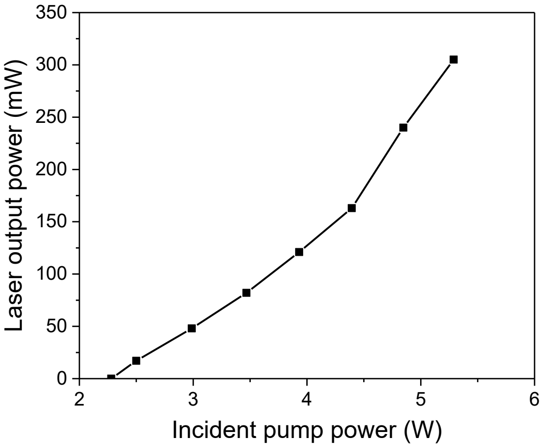

Figure 5.10.Laser output power against incident pump power for the wavelength tunable X-cavity Alexandrite laser with BiFi and R=99.0% OC at constant wavelength λ=759 nm.

The laser threshold was 2.3 W. The slope efficiency was 10.0% producing 306 mW output power at the maximum incident pump power of 5.3 W. The M^2 beam quality of $M^2_x = 1.56$ & $M^2_y = 1.53$ was measured at this output power. It is noted that the slope efficiency at higher pumping level was 13.9%, which suggests that the output power can be further increased by using more pump power. The reduced slope efficiency obtained from the wavelength tunable Alexandrite laser as compared with that (28%) of the compact diode-pumped system is due to losses induced by the cavity mirrors and BiFi plate.

The variation of the laser output power as a function of the emission wavelength was investigated using two output couplers with reflectance of 99.0% and 99.5%, respectively, as shown in Figure 5.11.

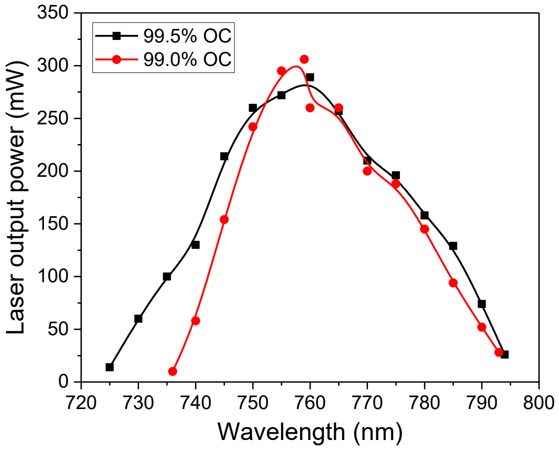

Figure 5.11. Wavelength tuning curves for the diode-pumped CW X-cavity Alexandrite laser using R=99.0% OC (red circles) and R=99.5% OC (black squares).

The wavelength of the diode-pumped CW Alexandrite laser with the R=99.0% output coupler was smoothly tuned from 736 to 793 nm over a range of 57 nm. A maximum output power of 306 mW was achieved at 759 nm. For the R=99.5% output coupler, the laser wavelength was tuned in the range extended from 725 to 794 nm (69 nm), with a maximum output power of 289 mW at 760 nm.

The reflectance plots for these two output couplers are shown in Figure 5.12. The wavelength tuning range is seen to be limited by the reduction of output coupler's performance on the short wavelength side. For the R=99.0% OC, the sharp fall in mirror reflectivity near 730 –740 nm is seen in the sharp cut-off of the tuning curve near 735 nm. The R=99.5% OC extends the curve further but has a sharp fall in mirror reflectivity near 710-725nm, which indicates the reason for the tuning cut-off near 725nm.

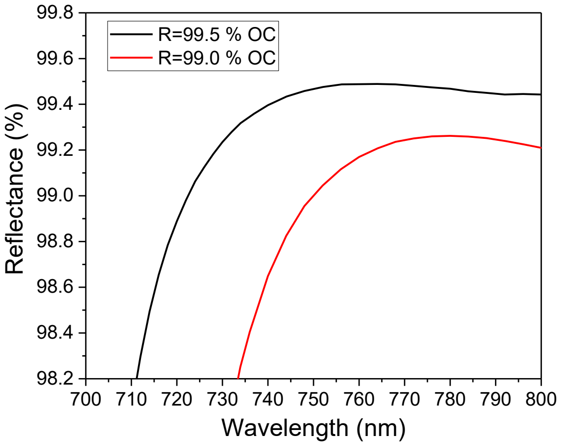

Figure 5.12. Reflectance plots (manufacture data) for R=99.5% OC (black curve) and R=99.0% OC (red curve).

The laser performance on the long wavelength side is partly limited by the temperature effect of the Alexandrite crystal. At a relatively low crystal temperature of 20°C, the gain cross-section and spectral shape favour shorter wavelengths. This means the long wavelength side of the tuning curve can be further extended by increasing the crystal temperature. However, the main focus of the study was operating the laser system around the SESAM wavelength band.

5.4 Wavelength Tunable Passively Q-switched Alexandrite Laser

After investigating the wavelength tunable CW Alexandrite laser cavity, the end mirror M_3 (see Figure 5.8) was replaced with a SESAM to obtain passively Q-switched laser pulses. Figure 5.13 shows the schematic diagram of the wavelength tunable passively Q-switched diode-pumped Alexandrite laser. The R=99.0% OC was used in this system. The BiFi plate was again used to tune the laser wavelength. The cavity had a total length of 345 mm.

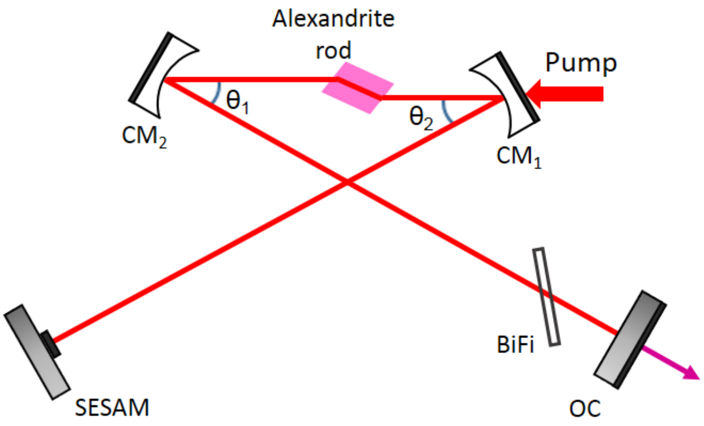

Figure 5.13. Schematic of the wavelength tunable passively Q-switched diode-pumped Alexandrite laser. CM$_1$ and CM$_2$ are curved mirrors with 100mm radius of curvature. M$_3$ is a HR mirror for laser. OC is an output coupler with R=99.0%.

5.4.1 SESAM Device

The SESAM device used for the passively Q-switched Alexandrite laser was bonded onto an aluminium disc with thermal adhesive to dissipate heat, as shown in Figure 5.14. The structure of the SESAM is shown in Figure 5.15. The SESAM consists of multiple layers of InP quantum dots on a distributed Bragg reflector. There are 7 groups each with 3 quantum dot layers, a total number of 21 quantum dot layers were incorporated within the structure for resonant periodic gain. Each InP quantum dot layer with a thickness of 0.62 nm was deposited on a layer of AlGaInP and capped by a GaInP quantum well to form a dot-in-well structure [195].

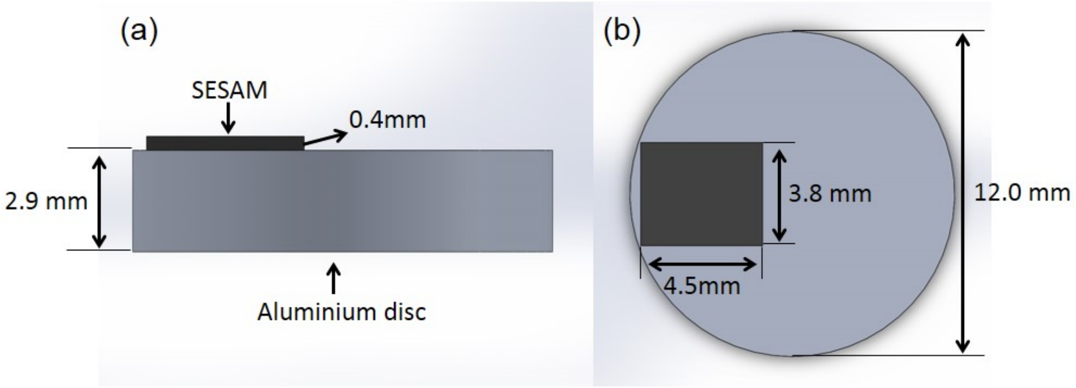

Figure 5.14. (a) Front and (b) top views of the SESAM device bonded on an aluminium disc.

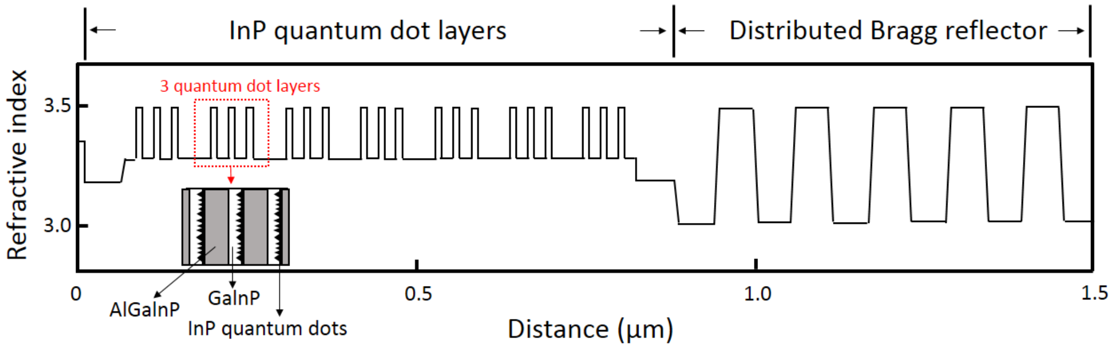

Figure 5.15. Schematic of the SESAM structure including InP quantum dot layers (7 x 3 layers) and distributed Bragg reflector.

The SESAM had a 50 nm reflectivity bandwidth centred at 765 nm shown in Figure 5.16. It had a saturable absorption with modulation depth of ~0.5% and some nonsaturable loss (~1%). Both the modulation depth and nonsaturable loss were wavelength dependent. The absorption recovery of the SESAM was bi-exponential with 0.4 ps for the fast component and 300 ps for the slow component. The saturation fluence of the SESAM was 30 μJ/cm^2.

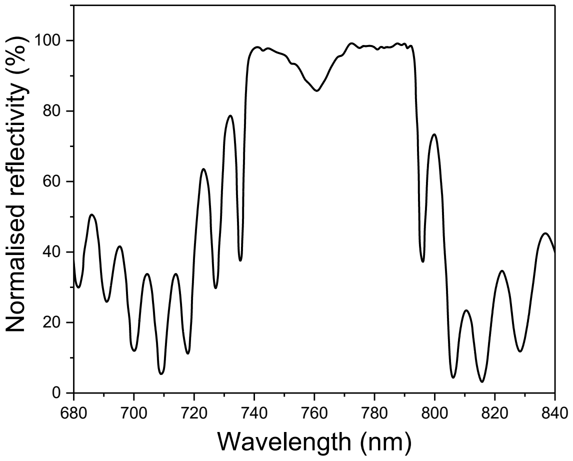

Figure 5.16. Reflectance plot for the SESAM used for the Passively Q-switched Alexandrite laser.

5.4.2 Results of Passive Q-switched Operation

After optimising the cavity alignment, the system shown in Figure 5.13 started passively Q-switching. Characteristics of pulses including the pulse width, repetition rate and average power were recorded for the passively Q-switched Alexandrite laser system.

The wavelength was tuned from 771 to 786 nm, but the laser operated in the passively Q-switched regime only between 775 to 781 nm. Figure 5.17 shows the evolution of the output power, pulse width, and repetition rate of the pulses obtained within the wavelength tuning range. Compared with the tuning curves obtained under CW operation of the Alexandrite laser (see Figure 5.10), the tuning range of the passively Q-switched Alexandrite laser is much narrower, which is limited by the reflectivity band of the SESAM. The resonant character of the SESAM in the wavelength range ~750-770 nm introduced high passive losses and affected the Q-switching behaviour.

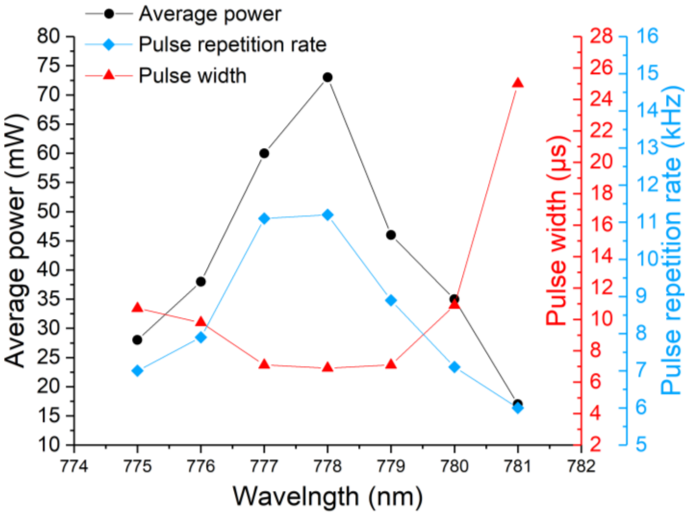

Figure 5.17. Average output power (mW), pulse width (μs), repetition rate (kHz) of the pulses obtained within wavelength tuning range for the passively Q-switched Alexandrite laser.

Figure 5.18 (a) & (b) showsthe pulse profile and pulse train, which were obtained at 778 nm, the spectrum with a spectral width (FWHM) of 0.32 nm is shown in Figure 5.18 (c). An average power of 73 mW and a repetition rate of 11.2 kHz resulted in the Q-switched pulse energy of 6.5 μJ under 5 W pump power. The pulse width (FWHM) was 6.9 μs. The relatively long pulse duration was due to the long cavity photon lifetime resulted from the large cavity length (345 mm) and the highly reflective output couplers we used (R=99.0%). The mode of the passively Q-switched operation was highly stable, as illustrated by the highly regular pulse train shown in Figure 5.18 (b).

The laser beam from the R=99.0% output coupler was imaged by a relay-imaging system (formed by a pair of lenses both with a focal length of 300 mm) onto the CMOS camera. The spatial profile is shown in Figure 5.18 (d). The laser beam waist has a diameter of 288 μm (x) by 326 μm (y) with $M^2 < 1.1$ in both axes. Because of the symmetry of the laser cavity, the beam size on the SESAM is roughly the same as the size on the OC. At the highest average output power of 73 mW, the estimated fluence on the SESAM was 0.88 J/cm^2.

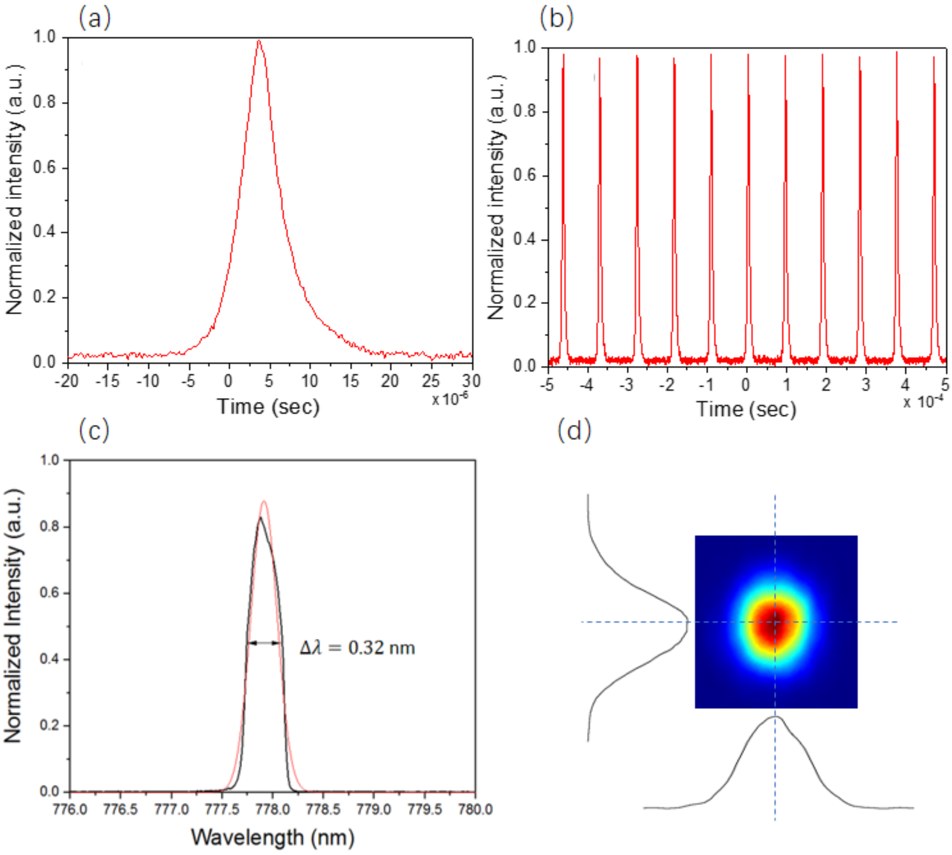

Figure 5.18. (a) Pulse profile and (b) pulse train observed from passively Q-switched Alexandrite laser at 778 nm with pulse width (FWHM) of 6.9 μs and repetition rate of 11.2 kHz. (c) The spectrum of the passively SESAM Q-switched Alexandrite laser pulses with a peak wavelength of 778 nm and a spectral width of 0.32 nm (FWHM). The red curve is the Gaussian fit to the spectrum. (d) Spatial profile of the output beam.

Figure 5.19 shows the results of the output power against incident pump power for the passively SESAM Q-switched Alexandrite laser using two output couplers with reflectance of 99.0% and 99.5%, respectively. These power curves were obtained with the BiFi removed from the cavity to reduce the insertion loss. The R=99.0% coupler had a higher threshold and a higher slope efficiency than the R=99.5% one. For the R=99.0% OC, the shortest pulse was 5.3 μs obtained at 10.7 kHz repetition rate with 90 mW average output power, which corresponds to 8.4 μJ pulse energy. For the R=99.5% OC, the shortest pulse duration obtained was 3.4 μs with 16.7 kHz repetition rate and 76 mW average output power (4.6 μJ pulse energy). Optical damage of the SESAM at 4.6 W incident pump power prevented the further increase of the incident pump power.

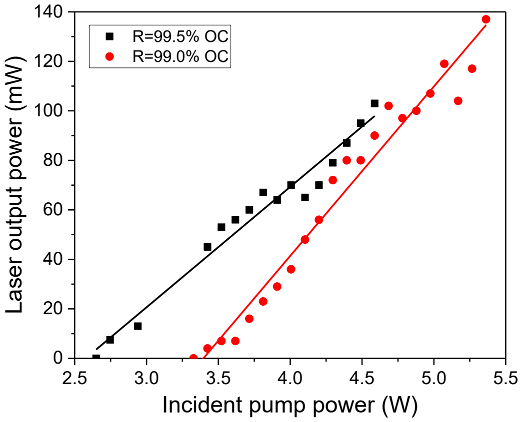

Figure 5.19. Laser output power against incident pump power for the passively Q-switched Alexandrite laser using R = 99.0% OC (red circles) and R = 99.5% OC (black squares).

5.5 Summary

This chapter investigated a wavelength tunable passively Q-switched diode-end-pumped Alexandrite laser. The passively Q-switched operation was realized using an X-shaped cavity with a SESAM device. Wavelength tuning of the Alexandrite laser was demonstrated using a BiFi plate.

Diode-end-pumping was achieved using a fiber-coupled red diode laser that delivers symmetric output with relatively high brightness. The fiber delivery partially scrambles the polarisation of the pump laser. As a result, only ~70% of the overall pump power was effectively used to pump the Alexandrite crystal due to the polarisation dependent absorption properties of Alexandrite.

Initially, a compact linear CW Alexandrite laser was developed to explore the output power and efficiency potential. An output power of 1.1 W with a slope efficiency of 28% was achieved at an incident pump of 5.3 W (~3.7 W absorbed pump power). Astigmatic properties of the Brewster-angle cut crystal and the curved mirrors at oblique angles were discussed in detail. For a 4-mirror X-shaped cavity including a Brewster-angle cut Alexandrite crystal with a given length, astigmatic compensation can be achieved by carefully selecting the radius of curvature and the tilt angle of the curved mirrors.

The CW X-cavity Alexandrite laser with a R=99.5% output coupler had a wavelength tuning range of 69 nm (from 725 to 794 nm). The short wavelength side of the tuning range can be further optimised by using an output coupler with a better-profiled mirror spectrum, while the long wavelength side can be extended by optimising the Alexandrite crystal temperature.

The Q-switched operation was observed between 775 and 781 nm. The reduced tuning range was due to the limited reflectivity band of the SESAM and the intracavity losses. Highly stable passively Q-switched pulses with 73 mW average output power (6.5 μJ pulse energy) and 6.9 μs pulse duration were obtained at 778 nm. The pulses had a TEM_{00} beam profile (M^2<1.1) and a narrow spectral width (0.32 nm). Pulses with 90 mW average output power and 5.3 μs duration at 10.7 kHz were obtained without using BiFi.

The results obtained in this study, especially the average output power and pulse energy, can be further improved by optimising mode matching and pumping (beam quality and pump power). The laser cavity used for the passively SESAM Q-switched operation was designed to produce a relatively large laser mode waist to match to the pump beam size at the pump face of the crystal. This necessitated a long distance between the curved mirrors with the radius of curvature of 100 mm and the crystal, which adversely affected the pump beam because of the negative lensing and aberrations induced by the pump-through curved mirror. In the next chapter, an enhanced ‘displaced mode’ cavity design using a ‘zero lens’ pump-through mirror with a shorter radius of curvature was investigated to solve the above problems. Further development aims to achieve higher efficiency and higher pulse energy. The passively Q-switched Alexandrite laser provides a simple route to wavelength tunable pulsed operation in the near-infrared band and potentially in the ultraviolet region via harmonic conversion.

Chapter 6

Single-longitudinal-mode Operation of an Alexandrite Ring Laser

Diode-pumping is a promising route to constructing simple, compact and inexpensive lasers. It would be desirable for diode-pumped Alexandrite lasers to have narrow linewidth, well controlled wavelength tunability and high output power to enable a multitude of precision applications, including light sources for LIDAR [174,175,196,197], high-resolution spectroscopy [198] and fiber-optic sensor [199,200]. Flash-lamp-pumped Q-switched unidirectional Alexandrite ring lasers injection-seeded by Ti:sapphire or diode lasers were developed for LIDAR and spectroscopy applications [174,175,196–198], but the overall laser systems were complex, bulky and of low efficiency. Recently, a Q-switched bi-directional Alexandrite ring laser [187] and a Q-switched ring system in single-longitudinal-mode (SLM) operation achieved by injection-seeding under pulsed diode-pumping have been developed for LIDAR applications [185]. These existing studies and the broad application prospects have aroused our interest in the SLM operation of Alexandrite lasers under diode pumping.

In this chapter, the development of a CW unidirectional Alexandrite ring laser is presented. Narrow-linewidth outputs are achieved with the SLM operation. In addition, the system has the advantages of low cost and compactness due to the use of direct diode pumping. This chapter begins with the description of a compact linear cavity, which is used to assess the potential of a Brewster-cut Alexandrite rod. Based on the X-shaped cavity design used in the passively Q-switched system, an optimized X-shaped cavity is developed and used as a precursor to the ring cavity. Finally, a method for implementing the unidirectional operation is given, along with the results obtained with the Alexandrite ring laser. The results and analyses obtained in this chapter have contributed to a journal article [149].

6.1 High Efficiency Compact Linear Alexandrite Laser

Prior to the ring laser operation, in order to assess the power and efficiency potential of the diode-pumped Alexandrite laser, a compact linear cavity was investigated in this section.

Figure 6.1 shows the schematic of the compact diode-end-pumped Alexandrite laser. The gain medium used in this cavity was a *c*-cut Alexandrite rod with Brewster-angled end faces. It had a length of 7.5 mm, a diameter of 4 mm and Cr^{3+}-doping concentration of 0.22 at.%. The absorption coefficient of the Alexandrite rod was measured to be 6.6 cm^{-1} with a He-Ne laser (633 nm). The rod was embedded in a water-cooled copper heat sink for temperature control. The temperature of the Alexandrite rod was maintained at 20°C. The b-axis and Brewster faces of the gain medium were orientated horizontally in a plane-plane compact linear cavity. The compact linear cavity was formed of two plane mirrors: a dichroic back mirror (BM) which was highly-transmitting (R<0.2%) at pump wavelength (~638 nm) and highly-reflecting (R>99.9%) at laser wavelength (~755 nm), and an output coupler (OC) with a reflectance of 98.8% at the laser wavelength. The cavity length was 13 mm.

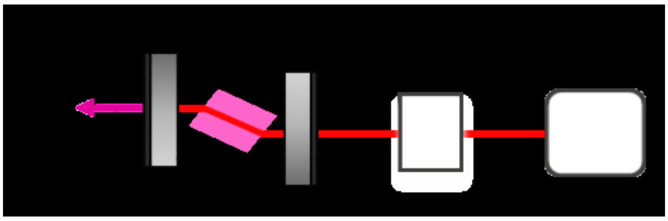

Figure 6.1. Schematic of the diode-end-pumped Alexandrite Brewster-angle cut rod with compact linear laser cavity. BM is a dichroic back mirror, OC is an output coupler with R=98.8%

Pumping was provided with the free-space red diode module, which has been described in Section 4.1. The temperature of the pump module was cooled to 16°C with a water chiller. The diode module was operated in CW mode. The pump beam was shaped in the horizontal direction with a beam shaping system due to the highly multimode character of the pump beam, which is described in detail in Section 6.1.1. The horizontal beam quality factor was improved but at the expense of the loss of the pump power.

6.1.1 Pump Beam Shaping

The pump beam was shaped in the horizontal direction with a beam shaping system shown in Figure 6.2. A 4° glass wedge and two mirrors (M_1 & M_2) were used to compensate the tilt of the output and control the beam path. The beam was then incident onto two inclined square mirrors (SM_1 & SM_2). Their separation was adjusted by micrometer translation stages, so the two square mirrors actually formed an adjustable slit aperture that allows a control of the beam quality in the horizontal direction. The central part of the pump beam was transmitted by the slit, whilst the rest was reflected onto a beam dump. Therefore, the horizontal M^2_x value can be improved by narrowing the slit aperture but at the expense of losing power. The apertured output was then reshaped with a horizontal telescope formed of two cylindrical lenses (HCL_1 & HCL_2) with focal lengths of -50 and 130 mm, respectively. The telescope was used to match the horizontal size of the pump beam to that in the vertical direction at an aspheric pump lens (f_p). The pump lens with focal length of 50 mm was used to focus the pump beam to a spot located near the input face of the Alexandrite rod. A half-wave plate (HWP) was used to orient the pump light with high polarisation purity of ~ 99% parallel to the high absorbing b-axis of the Alexandrite rod.

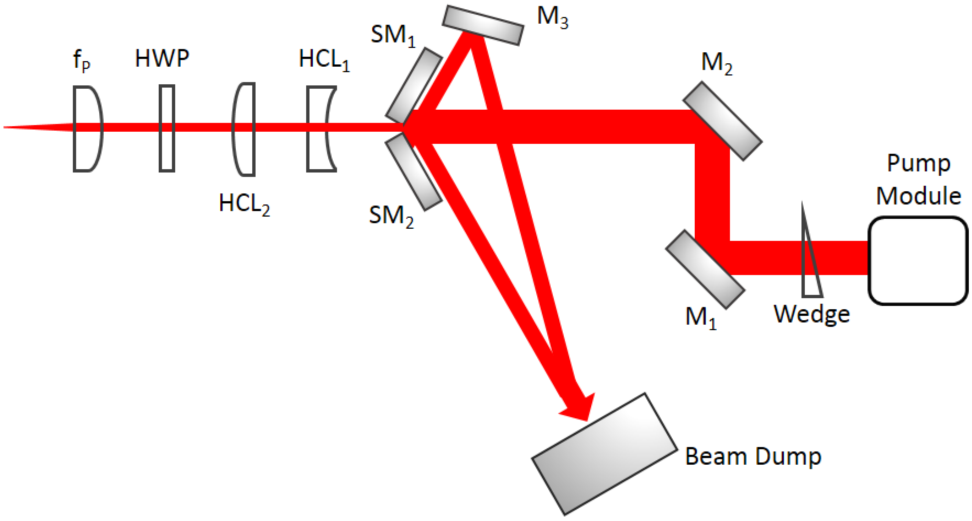

Figure 6.2. Schematic of the beam shaping optics. f_p is an aspheric pump lens with focal length of 50 mm. HWP is a half waveplate for matching pump polarisation to the crystal b-axis. HCL_1 and HCL_2 are two horizontal cylindrical lenses with focal length of -50 and 130 mm, respectively, formed a horizontal telescope. SM_1 and SM_2 are two square mirrors formed an adjustable slit aperature. M_1, M_2 and M_3 are plane mirrors.

An optical power of 5.6 W in CW mode with $M^2 = 30$ in both horizontal and vertical directions was available by setting the aperture size to be 1.5 mm. The waist diameter of the output beam was measured to be 123 µm (d_x) by 128 µm (d_y). Figure 6.3 shows the transmitted power as a function of the drive current. The diode threshold was 3.0 A and the power-current slope efficiency was 0.53 W/A.

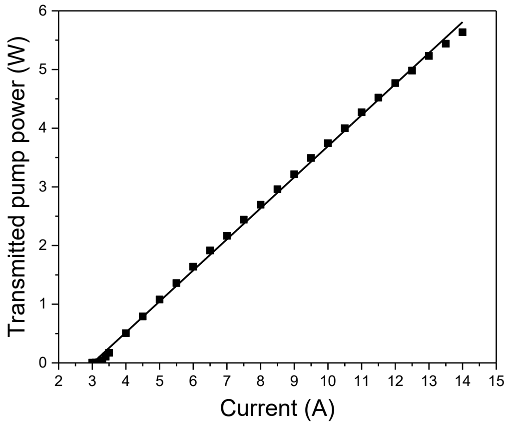

Figure 6.3. Pump power through the beam shaping optics against drive current at 16°C when the slit aperture size is 1.5 mm.

6.1.2 Results of Compact Linear Cavity

Figure 6.4 shows the results of the output power of the compact diode-end-pumped Alexandrite laser using the R=98.8% OC versus the incident pump power on the crystal.

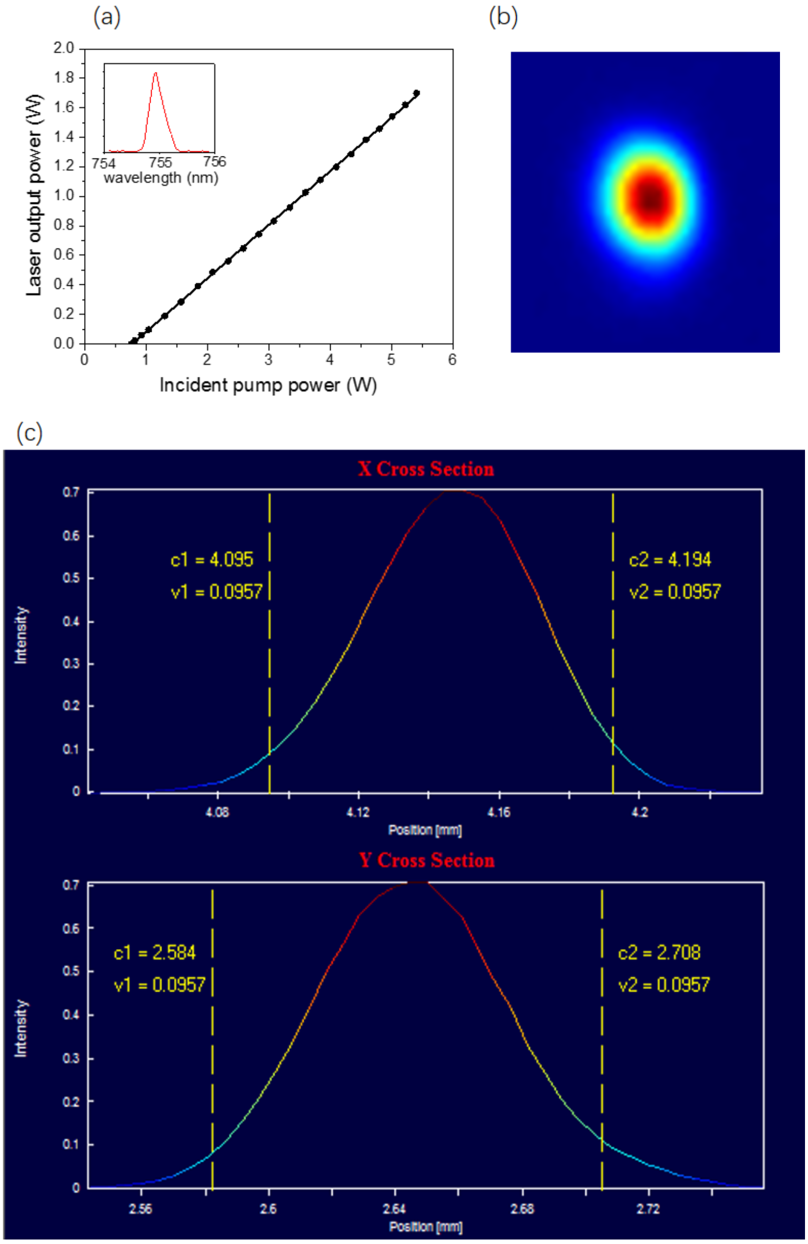

Figure 6.4. (a) Laser output power against CW incident pump power for the compact Alexandrite laser with R=98.8% OC. Line is linear fit to the power curve. Inset: wavelength spectrum of the compact linear Alexandrite laser. (b) Spatial mode profile of the output beam with M^2 =1.1 at 1.7 W output power. (c) Cross sections and beam width measurements ($1/e^2$) of the spatial mode profile in X and Y directions.

The laser threshold was 760 mW. A slope efficiency of 36.3% produced an output power of 1.7 W at the incident pump level of 5.4 W, corresponding to an optical-to-optical conversion efficiency of 31.5%. The spectral profile of the compact Alexandrite laser is shown in the inset of Figure 6.4. The spectrum centred at 755 nm with a bandwidth (FWHM) of 0.31 nm. Figure 6.4 (b) shows the spatial profile of the output of the compact cavity. The laser beam had a TEM_{00} beam profile with M^2 value of 1.1 in both x and y directions at the maximum pumping. Figure 6.4 (c) shows the cross sections and beam width measurement of the laser beam in X and Y directions. The laser beam was measured to be a diameter ($1/e^2$) of 99 μm (x) by 123 μm (y).

6.2 Enhanced X-shaped cavity

This section describes an investigation of an enhanced X-shaped cavity design based on the design investigated in Chapter 5. The pump delivery system and the mode matching strategy have been optimized to improve the laser efficiency and to reduce the cavity size. A ring cavity can be derived from the enhanced X-shaped cavity shown in Figure 6.5. Two identical curved (convex-concave) mirrors (CM_1^* and CM_2^*) with 50 mm radius of curvature were used as cavity mirrors. To optimize the compensation of the astigmatic distortions introduced by the Brewster-angle cut rod, the folding angles (θ_1, θ_2) of these mirrors were selected as $\theta_1 = \theta_2 = 28°$ according to Figure 5.6. Mirror M_3 with a high reflectance at the laser wavelength was the same as the BM used for the compact cavity in Figure 6.1. OC was an output coupler with a reflectance of 99.0% at the laser wavelength.

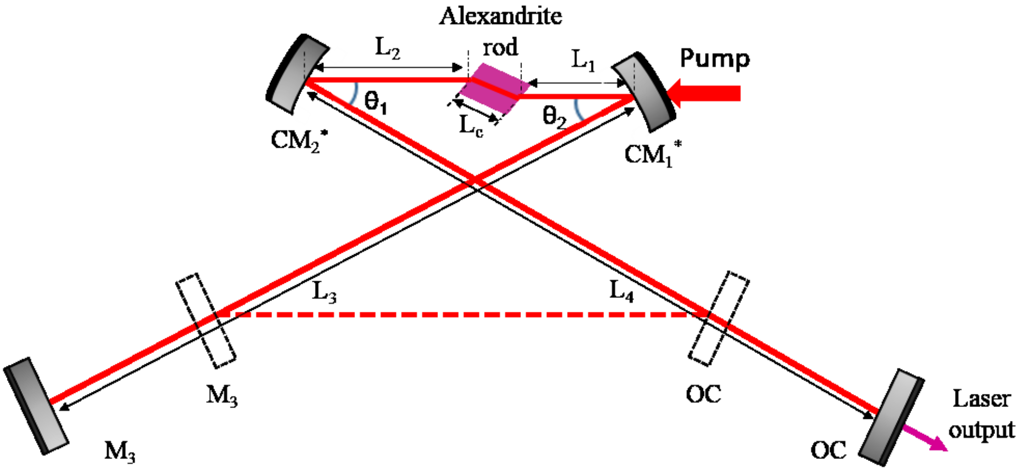

Figure 6.5. Schematic of diode-pumped X-cavity laser. CM_1^* and CM_2^* are curved mirrors with 50 mm radius of curvature. M_3 is a HR mirror for laser. OC is an output coupler with R=99.0%.

The enhanced X-shaped cavity was used as a precursor to the ring cavity design. The Alexandrite rod has a physical length of L_c (along with its axis of propagation) and a refractive index of n. The distances from the curved mirrors to the rod end faces are L_1 and L_2, respectively. The rest of the bow-tie ring section has a length of L. The total optical distance (D) as seen by the ring cavity beam is $L_1 + L_2 + nL_c + L$. The ring cavity can be considered as an equivalent X-shaped cavity with arm length L_3 and L_4 when the condition $L= L_3 + L_4$ is met.

6.2.1 Optimization of Pump Delivery System

The X-shaped cavity design was previously employed for the passively Q-switched operation of Alexandrite laser. The pump-through mirror (CM_1) with a plano-concave substrate was used at an oblique angle (see Figure 5.8) and equivalent to a lens as seen by the pump light. In this section, the negative impact of the pump-through mirror on the pump light is quantitatively analysed, and a solution has been found to weaken the impact of the mirror on the pump light.

For a lens in air, the focal length is given by the lensmaker's equation [201]:

$$\frac{1}{f} = (n-1)\left[\frac{1}{R_1} - \frac{1}{R_2} + \frac{(n-1)d}{nR_1R_2}\right] \tag{6.1}$$

where f is the focal length, n is the refractive index of the lens material, R_1 and R_2 are the radii of curvature of the front and rear surfaces of the lens, respectively, and d is the thickness of the lens.

For example, for a plano-concave substrate with $R_1 \rightarrow \infty$, R_2 = 100 mm, a refractive index of n = 1.5, and a thickness of d = 6.35 mm, the focal length f_{pc} is given by

$$f_{pc} = \frac{-R_2}{(n-1)} = -200\,mm \tag{6.2}$$

Obviously, the pump-through mirror with the plano-concave substrate acted as an astigmatic negative lens that increases the pump size and degrades the beam quality.

In order to increase the laser efficiency, it is proposed to improve the pump-through mirror system to deliver a smaller beam with higher quality. A ‘zero lens’ pump-through mirror with a convex-concave substrate was introduced in the enhanced X-shaped cavity design.

Considering a convex-concave mirror with R_1 = R_2 = 100 mm has n = 1.5 and d = 6.35 mm. Putting these parameters in Equation (6.1) results in the focal length f_{cc}

$$f_{cc} = \frac{n{R_1}^2}{(n-1)^2 d} = 9448\,mm \tag{6.3}$$

Therefore, the ‘zero lens’ pump-through mirror acts as a very weak positive lens as seen by the pump light.

In order to quantify the impact of the two different pump-through mirrors on the pump beam in both horizontal and vertical directions, ray matrices (ABCD matrices) are used to simulate the propagation of the pump beam through a pump lens and pump-through mirror.

The ABCD matrices for a curved interface between two dielectric media with an incident ray at an arbitrary angle in the horizontal (x) and vertical (y) planes are given by [71]

$$M_x = \begin{vmatrix} \dfrac{\cos\theta_2}{\cos\theta_1} & 0 \\ \dfrac{(n_2\cos\theta_2 - n_1\cos\theta_1)}{R\cos\theta_1\cos\theta_2} & \dfrac{\cos\theta_1}{\cos\theta_2} \end{vmatrix} \tag{6.4}$$

$$M_y = \begin{vmatrix} 1 & 0 \\ \dfrac{(n_2\cos\theta_2 - n_1\cos\theta_1)}{R\cos\theta_1\cos\theta_2} & 1 \end{vmatrix} \tag{6.5}$$

where R is the radius of curvature of the curved interface (see Figure 6.6 (a)), θ_1 is the angle of incidence, θ_2 is the angle of refraction. The refractive indices of medium 1 and medium 2 are n_1 and n_2, respectively.

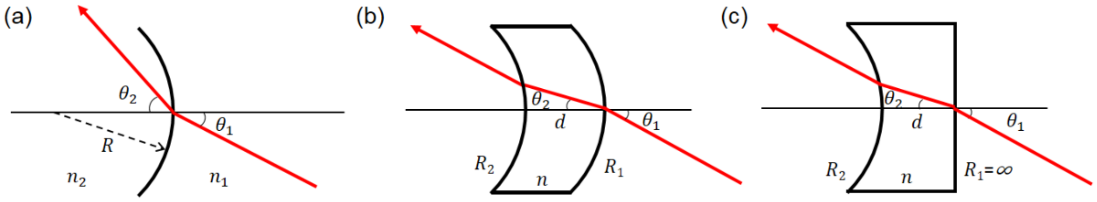

Figure 6.6. (a) A curved interface with an incident ray at an arbitrary angle. (b) A convex-concave mirror with an incident ray at an arbitrary angle. (c) A plano-concave mirror with an incident ray at an arbitrary angle.

The ABCD matrices for a convex-concave mirror (Figure 6.6 (b)) with an incident ray at an arbitrary angle (equivalent to a tilted curved mirror) can be obtained by applying Matrices (6.4) and (6.5) for two curved interfaces ($R_1 = R_2$) separated by a medium with a length of d. The refractive index of the medium is n. Compared with the convex-concave mirror, the first surface of a plano-concave mirror (Figure 6.6(c)) is plane ($R_1 \to \infty$), the rest of the parameters are exactly the same as that of the convex-concave mirror. Therefore, the matrices for curved mirrors in the horizontal (x) and vertical (y) directions are given by

$$M_{mirror-x} = M_{x(R_2)} \begin{vmatrix} 1 & \dfrac{d}{n} \\ 0 & 1 \end{vmatrix} M_{x(R_1)} \tag{6.6}$$

$$M_{mirror-y} = M_{x(R_2)} \begin{vmatrix} 1 & \dfrac{d}{n} \\ 0 & 1 \end{vmatrix} M_{y(R_1)} \tag{6.7}$$

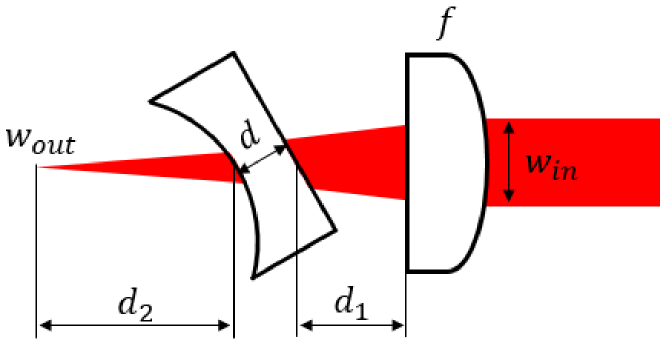

Figure 6.7. The schematic of a lens-mirror system consists of a pump lens and a tilted pump-through mirror.

Then, the ABCD matrices for propagating the pump beam through a pump lens and a tilted pump-through mirror (see Figure 6.7) for x- and y-directions are

$$M_{lens-mirror-x} = \begin{vmatrix} 1 & d_2 \\ 0 & 1 \end{vmatrix} M_{mirror-x} \begin{vmatrix} 1 & d_1 \\ 0 & 1 \end{vmatrix} \begin{vmatrix} 1 & 0 \\ -\frac{1}{f} & 1 \end{vmatrix} = \begin{vmatrix} A_x & B_x \\ C_x & D_x \end{vmatrix} \tag{6.8}$$

$$M_{lens-mirror-y} = \begin{vmatrix} 1 & d_2 \\ 0 & 1 \end{vmatrix} M_{mirror-y} \begin{vmatrix} 1 & d_1 \\ 0 & 1 \end{vmatrix} \begin{vmatrix} 1 & 0 \\ -\frac{1}{f} & 1 \end{vmatrix} = \begin{vmatrix} A_y & B_y \\ C_y & D_y \end{vmatrix} \tag{6.9}$$

where f is the focal length of the pump lens, d_1 is the distance between the lens and the mirror, d_2 is the distance between the mirror and the location of the pump beam waist.

For the lens-mirror system, the incoming beam is assumed to be collimated, so it is at a waist. Thus, the q parameter of the incoming beam is

$$q_{in} = i\frac{\pi w_{in}^2}{M^2\lambda} = iz_{0in} \tag{6.10}$$

where w_{in} is the waist size, M^2 is the beam quality factor, λ is the wavelength of the pump beam, z_{0in} is the Rayleigh range. According to Equation (2.1.4), the q parameter of the output beam is given by

$$\frac{1}{q_{out}} = \frac{1}{R} - i\frac{M^2\lambda}{\pi w_{out}^2} \tag{6.11}$$

By applying the ABCD law of Gaussian beam propagation, the q parameter of the output beam can also be expressed as

$$q_{out} = \frac{Aq_{in} + B}{Cq_{in} + D} \tag{6.12}$$

The substitution of Equation (6.10) into Equation (6.12) then gives

$$\frac{1}{q_{out}} = \frac{iz_{0in}C + D}{iz_{0in}A + B} = \frac{(BD + z_{0in}^2 AC)}{z_{0in}^2 A^2 + B^2} - i\frac{z_{0in}(AD - BC)}{z_{0in}^2 A^2 + B^2} \tag{6.13}$$

Equating the imaginary parts of Equation (6.11) and (6.13), and also using the ABCD matrices (Equation (6.8) and (6.9)) of the lens-mirror system, we get the waist size of the output beam in x- and y-planes, respectively

$$w_{out-x} = \frac{M_x^2 \lambda (z_{0in-x} A_x^2 + B_x^2)}{\pi z_{0in-x}(A_x D_x - B_x C_x)} \tag{6.14}$$

$$w_{out-y} = \frac{M_y^2 \lambda \left(z_{0in-y} A_y^2 + B_y^2\right)}{\pi z_{0in-y}\left(A_y D_y - B_y C_y\right)} \tag{6.15}$$

For a given distance (d_1) between the lens and the tilted mirror, the waist size of the output beam ($w_{out-x/y}$) and the distance (d_2) from the tilted mirror to the waist can be numerically solved. The waist size ($w_{out-x/y}$) is related to that of the incoming beam ($w_{in-x/y}$), the radii of curvature of the mirror (R_1 & R_2), the lens-mirror separation (d_1) and the angle of incidence (θ_1).

To visually describe the effect of the pump-through mirror on the pump beam, a parameter named 'beam waist size increase factor' is defined as the ratio of the beam waist size of the lens-mirror system and that of the only pump lens system. If the beam waist size is decreased by the mirror, the factor will be smaller than 1. Figures 6.8 shows the beam waist size increase factor as a function of the radius of curvature for the two different pump-through mirrors in x- and y- directions, respectively.

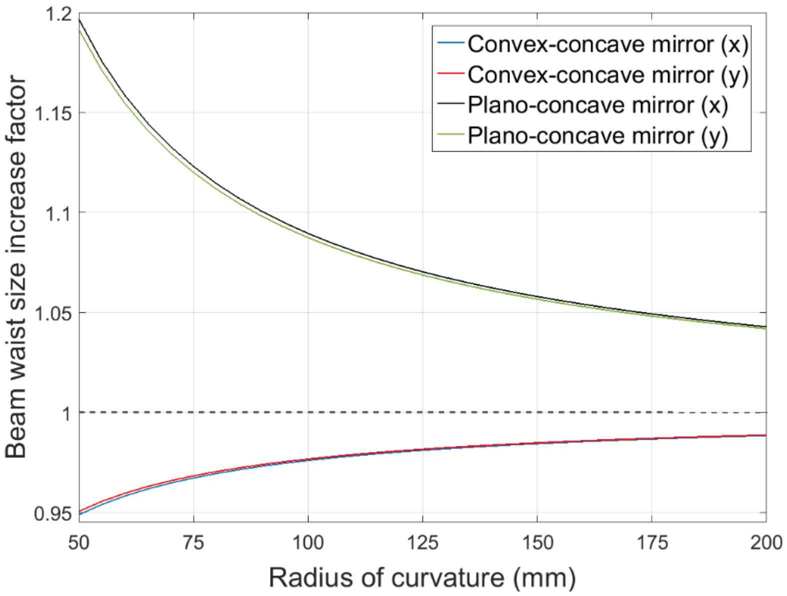

Figure 6.8. The beam waist size increase factor against the radius of curvature for convex-concave mirror and plano-concave mirror in x- and y- directions, respectively. The angle of incidence was set as 14°.

The results show that the plano-concave mirror has a more serious impact on the size of the pump beam waist than the convex-concave mirror (‘zero lens’). For example, for mirrors with 50 mm radius of curvature, the plano-concave mirror increases the waist size by ~20%, whilst the convex-concave mirror decreases the waist size by ~5%. Although the impact of these two types of mirrors on the beam size in x and y directions is different, the difference is very marginal. As the radius of curvature increases, the difference of the beam waist size increase factor between x and y directions is even more insignificant. Increasing the radius of curvature causes a weakened effect on the waist size for both types of mirrors. For mirrors with 200 mm radius of curvature, the plano-concave mirror increases the waist size by ~4.5%, while the convex-concave mirror decreases the waist size by only ~1.5%.

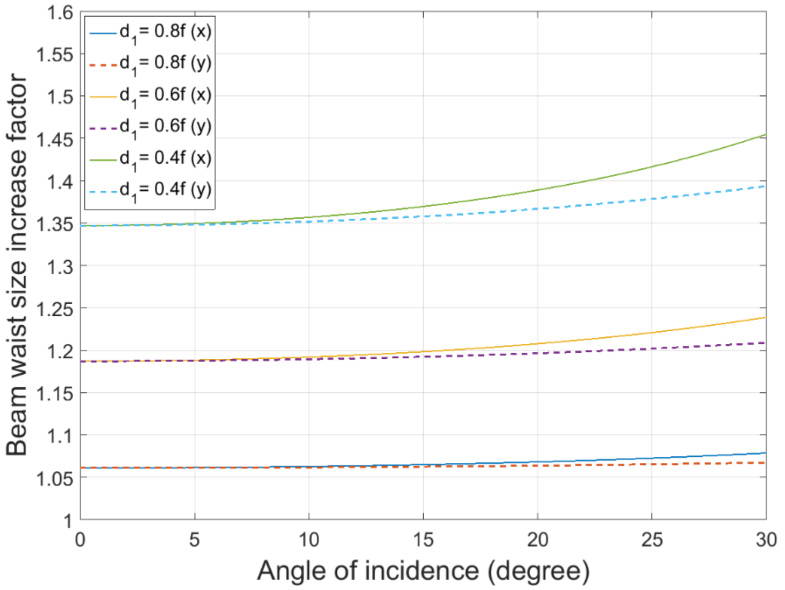

Figure 6.9. The beam waist size increase factor against the angle of incidence for various lens-mirror separations ($d_1 = 0.4\,f$, $0.6\,f$ and $0.8\,f$) for a plano-concave mirror with 50 mm radius of curvature. Solid lines represent the results for the x-direction, and dashed lines represent the results for the y-direction.

Figure 6.9 shows the beam waist size increase factor as a function of the angle of incidence for various lens-mirror separations ($d_1 = 0.4\,f$, $0.6\,f$ and $0.8\,f$) for a plano-concave mirror with 50 mm radius of curvature. Increasing the angle of incidence results in a more negative impact on the beam waist size. For $d_1 = 0.6\,f$, the beam waist size increase factor increases from 1.19 at $\theta_1 = 0°$ to 1.24 at $\theta_1 = 30°$ in the x-direction, corresponds to a 5% increase of the beam waist size.

The solid and dashed lines overlapped at $\theta_1 = 0°$ gradually diverge away from each other with the increasing angle. This indicates that the size of the beam waist in the x-direction is more sensitive to changes in angle than in the y-direction, especially when the lens-mirror separation is relatively small.

Decreasing the lens-mirror separation dramatically aggravates the negative impact of the mirror on the waist size. At $\theta_1 = 0°$, the beam waist size increases by ~6% when $d_1 = 0.8\,f$, and the value increases to ~35% when $d_1 = 0.4\,f$.

The results show that the plano-concave mirror defocuses the pump beam and leads to significant ellipticity at relatively large incident angles. This effect is even stronger for shorter lens-mirror separations.

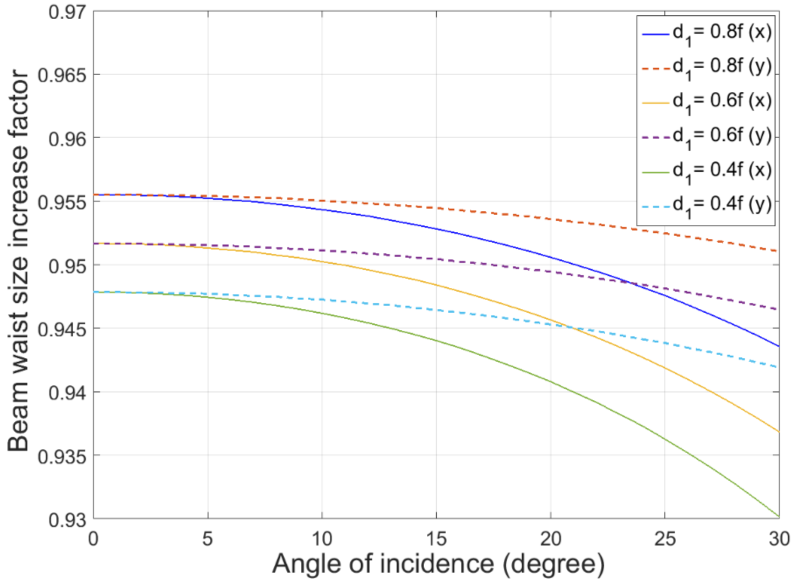

Figure 6.10. The beam waist size increase factor as a function of the angle of incidence for various lens-mirror separations ($d_1 = 0.4\,f$, $0.6\,f$ and $0.8\,f$) for a convex-concave mirror with 50 mm radius of curvature. Solid lines represent the results for the x-direction, and dashed lines represent the results for the y-direction.

Figure 6.10 shows the beam waist size increase factor as a function of the angle of incidence for various lens-mirror separations ($d_1 = 0.4\,f$, $0.6\,f$ and $0.8\,f$) for a convex-concave mirror with 50 mm radius of curvature. The angle of incidence also has different effects on the beam waist size in different directions. In comparison with the plano-concave mirror, the angular change for the convex-concave mirror has a small effect on the beam waist size. For $d_1 = 0.6\,f$, the beam waist size increase factor decreases from 0.952 at $\theta_1 = 0°$ to 0.944 at $\theta_1 = 30°$ in the x-direction, which means the beam waist size decreases by only 0.8%. In addition, the beam waist size is less affected by the mirror-lens separation for the convex-concave mirror. At $\theta_1 = 0°$, the beam waist size decreases by ~4.5% when $d_1 = 0.8\,f$ and by ~5.2% when $d_1 = 0.4\,f$.

In summary, the waist size of the pump beam transmitted through either the plano-concave mirror or the convex-concave mirror will be more or less affected regardless of the angle of incidence and the radius of curvature. The negative impact of both types of mirrors on the pump beam can be minimized by ensuring a relatively small angle of incidence and a relatively large mirror-lens separation. The convex-concave mirror has a significantly lower impact on the size and ellipticity of the beam waist. Therefore, a 'zero lens' pump-through mirror with a convex-concave substrate was used in the enhanced X-shaped cavity.

6.2.2 Optimization of Cavity Design

For the Alexandrite laser cavity designs described in previous sections, the strategy for TEM_{00} operation of an end-pumped solid-state laser is a design to produce a laser mode waist with the size and location to match to the pump beam at the pump face of the crystal, where the majority of the inversion volume is located [55,202,203]. This design is denoted as the 'matched mode' cavity design, the concept of the design is shown in Figure 6.11 (a). The 'matched mode' design necessitates a cavity mirror with a large radius of curvature and a large aperture size, and also a long distance between the mirror and the crystal.

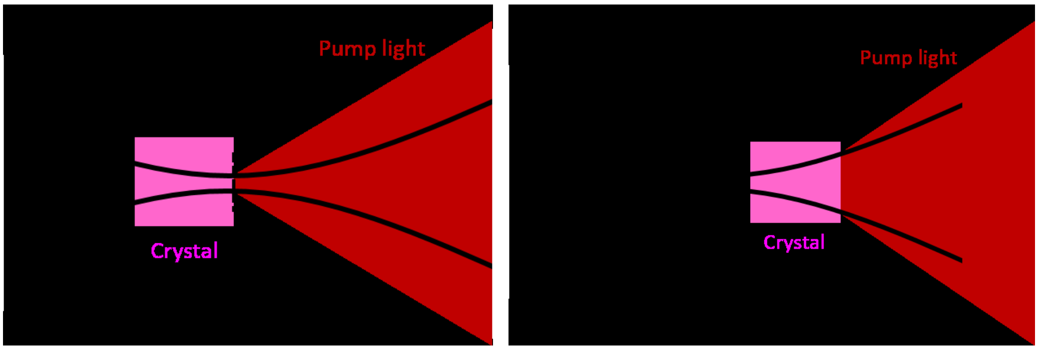

Figure 6.11. Schematic diagrams of (a) 'matched mode' cavity design and (b) 'displaced mode' cavity design. The dashed lines indicate the location of the laser mode waist.

In the enhanced X-shaped cavity, we employed a design using a laser mode waist radius (~20 μm) that was significantly smaller than the pump beam radius (64 μm) but with the waist location displaced from that of the pump face of the crystal. The displaced location of the laser waist was chosen to allow the expansion of the laser mode to match to the pump size at the pump face of the crystal. We denote this as the 'displaced mode' cavity design, as sketched in Figure 6.11 (b). The benefit of the ‘displaced mode’ cavity design with a small waist size (and hence high divergence angle) is that it allows the employment of curved cavity mirrors with a short radius of curvature, thereby enabling the cavity to be more compact. It is worth mentioning that the pump size cannot be reduced to this small waist size because of its high M^2 and its Rayleigh length needing to be matched to the absorption depth (1.5 mm) of the crystal.

6.2.3 Results of Enhanced X-shaped Cavity

The enhanced X-cavity Alexandrite laser using the ‘zero-lens’ pump-through mirror and ‘displaced mode’ cavity design was investigated in this section. The laser output power against the incident pump power for R=99.0% OC is shown in Figure 6.12. The laser threshold was 730 mW. At the maximum incident pump power (5.4 W), the system produced a laser output power of 1.2 W. The overall slope efficiency was 24.2%, but it increased to 30.9% at higher pumping level (>4 W). The anomalous power curve discontinuity was correlated to a power-dependent laser mode. The laser cavity was optimized at the maximum incident pump power, and thermal lensing varies with the pump power. When the pump power drops, the stability of the laser cavity will be affected by the thermal lensing accordingly. The laser mode on the end mirror (M_3) was relay-imaged with a pair of lenses (with focal length f=150 mm) onto a CMOS camera to investigate the stability of the enhanced X-shaped cavity. The degradation of the laser mode was clearly seen with the decrease of the incident pump power, and this phenomenon was observed repeatedly.

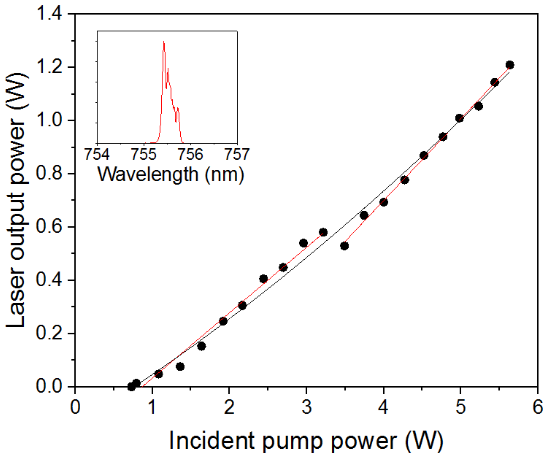

Figure 6.12. (a) Laser output power against incident pump power for the enhanced X-shaped Alexandrite laser. The Black line is linear fit to the overall power curve. Red Lines are linear fits to the power curve for two different gradients. Inset: Spectrum of the diode-pumped X-shaped Alexandrite laser in CW operation.

The inset of Figure 6.12 shows the laser spectrum with a peak wavelength of 755.3 nm and a bandwidth (FWHM) of 0.27 nm. The beam quality of $M^2{}_x = 1.10$ & $M^2{}_y = 1.72$ was measured at the full pumping power, and the laser beam size at the BM was measured to be diameter of 698 μm (x) by 456 μm (y). From these results, it can be seen that the system was still suffering some astigmatism, although the folding angles (θ_1, θ_2) were selected to compensate the astigmatic distortions. This might be related to the strong thermal lensing induced by the nearly linearly polarised pump with high intensity.

6.3 Diode-end-pumped Unidirectional Alexandrite Ring Laser

A 4-mirror bow-tie ring laser geometry is shown in Figure 6.13. The unidirectional operation of the ring laser was achieved by the introduction of a Faraday rotator (FR) and a half-wave plate (HWP) to compensate the rotation. A quartz birefringent filter (BiFi) plate with a thickness of 0.5 mm was inserted at Brewster's angle to allow wavelength tuning of the output. Our design was configured to have an ultra-compact cavity. The total cavity length was only 380 mm, and the overall footprint of the laser had dimensions ~140 x 90 mm. Here, the crystal temperature was increased to 40°C, as Alexandrite experiences increased performance at elevated temperatures [45,46].

For the pump module, the size of the slit aperture was increased from 1.5 to 2.7 mm. Therefore, the pump power was increased to 10.8 W, and the horizontal beam quality lowered to $M^2_x = 50$ whilst the vertical beam quality remain the same ($M^2{}_y = 30$).

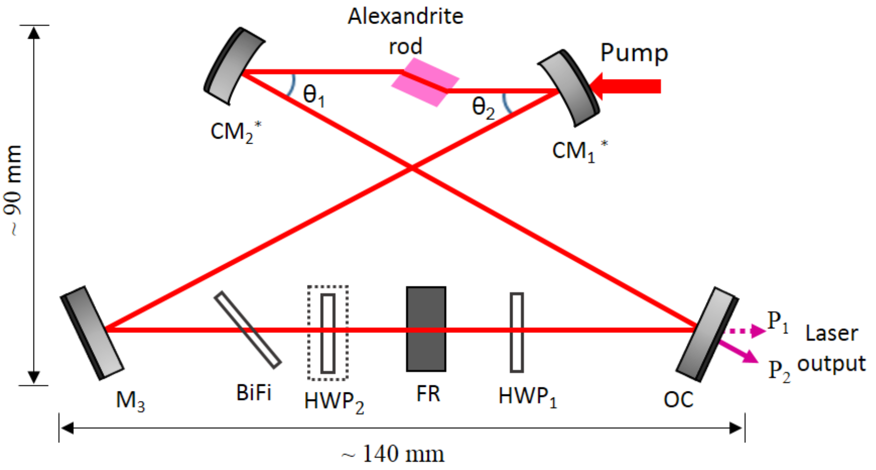

Figure 6.13. Schematic of the diode-pumped unidirectional Alexandrite ring laser. CM_1^* and CM_2^* are curved mirrors with 50 mm radius of curvature. M_3 is an HR mirror for laser. OC is an output coupler with R=99.0% at the incident angle ($\theta_1/2$) of 14°. The laser wavelength could be tuned using the birefringent filter (BiFi). The unidirectional operation of the ring cavity was achieved using a Faraday rotator (FR) and a half-wave plate (HWP_1). The unidirectional laser output P_1, P_2 could be switched by rotation of the HWP_1. HWP_2 is a second half-wave plate for additional polarisation control.

6.3.1 Realization of Unidirectional Operation

The unidirectional operation was implemented by introducing a Faraday rotator combined with a half-wave plate, which leads to different losses for the two propagation directions inside the ring cavity.

A Faraday rotator is a photonic device that can rotate the polarisation state of the transmitted light beam based on a magneto-optic effect [204]. When a linearly polarized beam travels through a transparent medium which is exposed to a magnetic field, and the magnetic field is applied parallel to the propagation direction of the beam, the polarisation direction of the beam is rotated by an angle β, which is given by

$$\beta = VBd \tag{6.16}$$

where B is the magnetic flux density along the propagation direction, V is the Verdet constant of the material, d is the length of the medium. The change of the polarisation direction is defined only by the sign of the Verdet constant and the direction of the magnetic field.

Faraday rotators are non-reciprocal elements, which means if a linearly polarized beam is transmitted through a Faraday rotator and returned after reflection at a normal incidence mirror, the polarisation changes of the two passes add up instead of offsetting each other. This non-reciprocal behaviour of Faraday rotators distinguishes them from other optical devices such as polarizers and waveplates, which allows Faraday rotators to be used as optical isolators in a laser cavity.

The Faraday rotator employed in our system includes a Brewster-angle cut Terbium Gallium Garnet (TGG) crystal with a length of 14.5 mm and a diameter of 4 mm. The TGG crystal was used as the magneto-optical medium and placed in a strong homogeneous magnetic field. The dimensions of the Faraday rotator are shown in Figure 6.14.

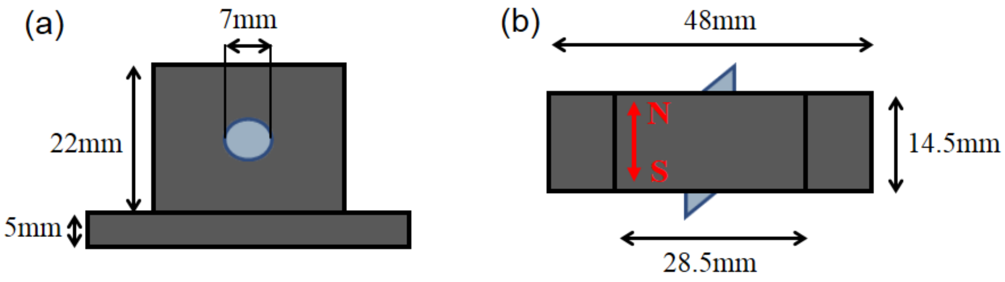

Figure 6.14. (a) Front and (b) top views of the Faraday rotator. S and N mark the south and north pole of the magnet.

Light passing through the Faraday rotator from the south (S) to the north (N) of the magnetic field experiences a clockwise polarisation rotation when viewed in the S/N direction. For light with a reversed direction of propagation traveling from N to S, the polarisation is again rotated clockwise as viewed in the S/N direction. An additional half-wave plate was introduced to offset the polarisation rotation of the Faraday rotator in one direction. Therefore, the polarisation of the light propagating in this direction remained unchanged before and after passing through the Faraday rotator and the half-wave plate, whereas the polarisation was rotated 90 degree for light propagating in the opposite direction. In the ring cavity, the combination of the Faraday rotator and the half-wave plate acting as an optical diode enforced unidirectional operation, and thereby preventing the formation of spatial hole burning that might otherwise arise from the standing-waves in a bi-directional ring cavity.

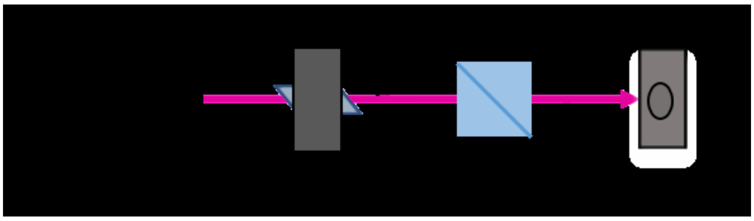

Figure 6.15. Setup used to measure the polarisation rotation of the Faraday rotator.

The polarisation rotation of the Faraday rotator was measured using a setup including an incident laser beam at a wavelength of 755 nm, a cube polarizer and a power meter, as shown in Figure 6.15. The cube polarizer was rotated to a position where the transmitted power was minimized. At and around this angular position, the transmitted power as a function of the cube polarizer's angle was measured for the Faraday rotator in both directions. The measurement was also conducted without using the Faraday rotator to confirm the polarisation state of the incident laser beam.

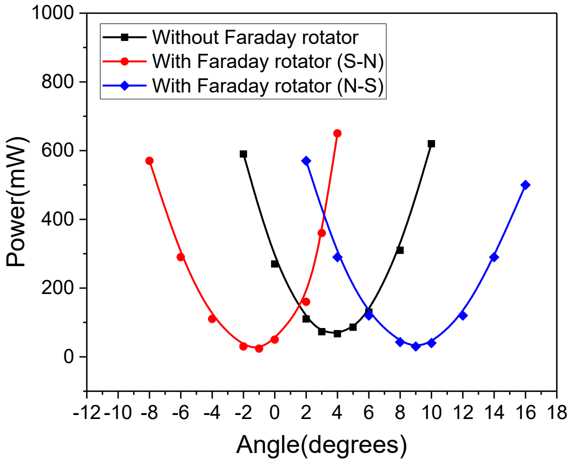

Figure 6.16. The transmitted power as a function of the cube polarizer's angle. S-N (N-S) corresponds to the laser beam travelling though the Faraday rotator from South to North pole (North to South pole).

Figure 6.16 shows the results of the transmitted power versus the angle of the cube polarizer for the system with and without the Faraday rotator. The Faraday rotator alters the polarisation of the incident beam by 4.5° (absolute value) in both directions.

The Faraday rotator was optimised for maximum transmission at 755 nm. The insertion loss of the Faraday rotator was then measured using a tunable Alexandrite laser at 755 nm. The insertion loss was $L_{FR} = 0.7\%$, which was obtained by measuring the incident power and transmitted power. It is noted that the loss varied negligibly as a function of wavelength. The insertion loss of the half-wave plate measured in the same way as for the Faraday rotator was $L_{HWP} = 0.1\%$.

6.3.2 Results of Unidirectional Operation

Figure 6.17 (a) shows the results of the output power against incident pump power for the unidirectional ring laser without the intracavity BiFi. At the maximum pump power of 10.8 W, the unidirectional ring laser produced an output power of 1.05 W (in a single direction P_2 shown in Figure 6.13). This corresponds to an optical-to-optical conversion efficiency of 9.7%. The laser output was in a fundamental TEM_{00} mode with beam quality of $M^2_x = 1.12$ and $M^2_y = 1.16$, as shown in Figure 6.17 (b). Figure 6.17 (c) shows the spatial profile of the output. Figure 6.17 (d) shows the cross sections and beam width measurement of the laser beam in X and Y directions. The laser beam was measured to be a diameter ($1/e^2$) of 163 μm (x) by 186 μm (y).

The laser slope efficiency was 11%. The lower slope efficiency compared to the compact linear cavity was consistent with the high insertion losses of multiple intra-cavity elements. The laser output power exhibits periodic variation as the incident pump power is increased, this is attributed to the variation of the laser spatial mode caused by thermally induced mode hopping. The laser leakage from the end mirror (M_3) was imaged by a relay-imaging system onto a CMOS camera to observe the behaviour of laser mode. When the mode hopping occurred, the output power would first decrease slightly and then increase with the incident pump power. The stability of the laser cavity is strongly affected by thermal lensing. The optical power of the thermal lens varies with the pump intensity. Therefore, under different incident pump powers, laser mode will change accordingly to adapt to the new stability conditions, as the cavity was optimised only at the maximum incident pump power. This behaviour was also found to be reproducible. Small deviations from linearity occurred in the power curve which was attributed to the variation of the laser spatial mode induced by thermal lensing at mid-pumping power.

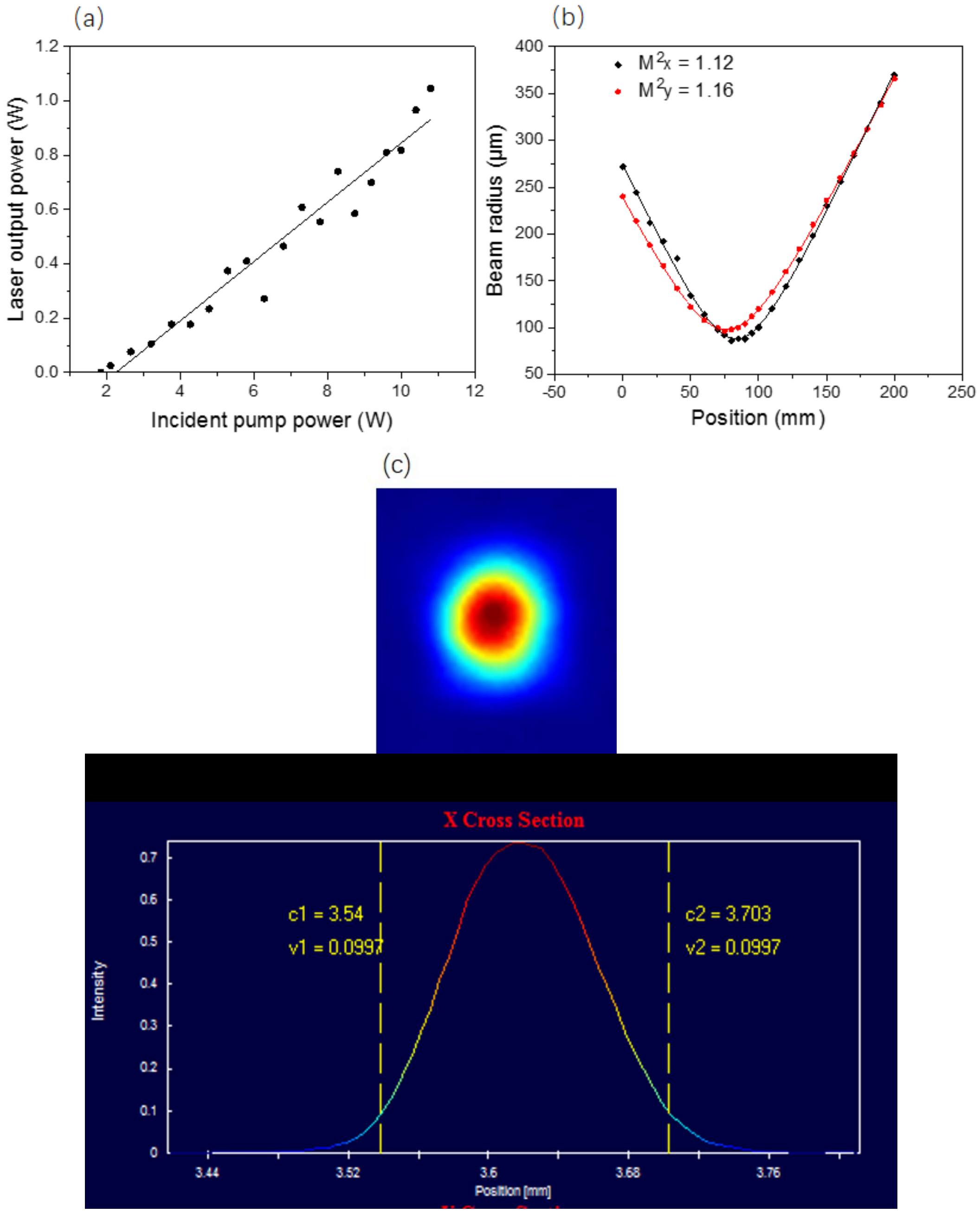

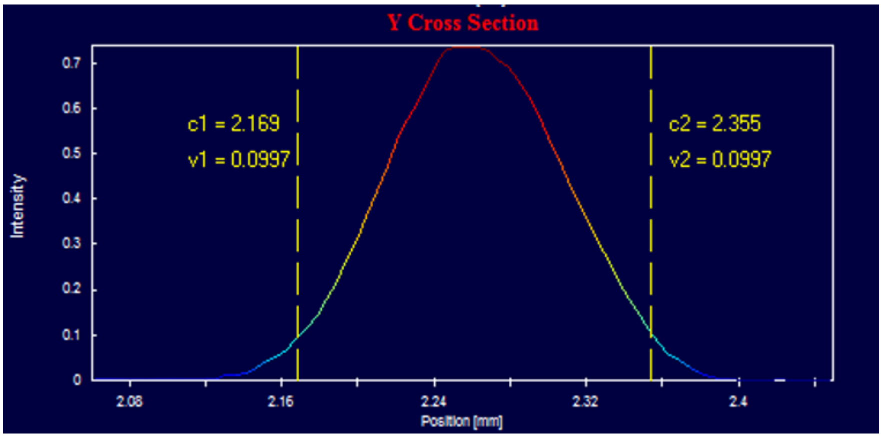

Figure 6.17. (a) Laser output power (P_2) against CW incident pump power for the diode-end-pumped unidirectional Alexandrite ring laser with R=99.0% output coupler under SLM operation. Line is linear fit to the power curve. (b) M^2 caustic fit for the SLM output of the unidirectional ring laser. (c) Spatial mode profile of the SLM output with $M^2 < 1.2$ at the maximum output power (1.05 W). (d) Cross sections and beam width measurements ($1/e^2$) of the spatial mode profile in X and Y directions.

The spectrum of the laser was investigated by analysing the laser output with a solid Fabry-Pérot (FP) etalon with 6.9 GHz free spectral range and a finesse of 50, corresponding to a resolving power ~140 MHz. The ring pattern produced by the interferometer was viewed on the CMOS camera via imaging in the focal plane of a f=150 mm lens. Single longitudinal mode (SLM) output was achieved in the unidirectional ring laser at an emission wavelength of 752 nm, which is seen in Figure 6.18 by the single ring pattern (per free spectral range) observed on the etalon. It is noted that the cavity mode spacing of 750 MHz (for the optical path length ~400 mm) was readily resolved by the FP etalon, and the single ring pattern confirmed the single longitudinal mode operation. This is the first demonstration of unidirectional single-longitudinal-mode operation with a CW diode-pumped Alexandrite ring laser. Since the cavity was not stabilised nor narrowed with an etalon, the spectrum could fluctuate and even operate on more than a single mode on occasion. Further optimization can be expected by adding of an intracavity etalon for enhanced spectral narrowing and a piezo-electric control of cavity length for wavelength stabilisation.

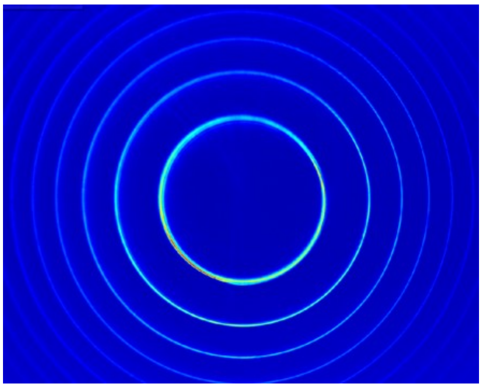

Figure 6.18. Spectral ring patterns from a Fabry–Pérot etalon showing single-longitudinal-mode operation at output power of 1.05 W and laser wavelength of 752 nm.

A brief investigation was conducted to explore the wavelength tunability of the unidirectional Alexandrite ring laser. Wavelength tuning was achieved by introducing the BiFi plate into the laser cavity and adjusting its angle. In an initial study, the variation of the CW output power as a function of the emission wavelength is shown in Figure 6.19 (a), and in a later implementation in Figure 6.19 (b). The tuning curves were obtained at the maximum pumping power of 10.8W with the unidirectional output in P_2 direction.

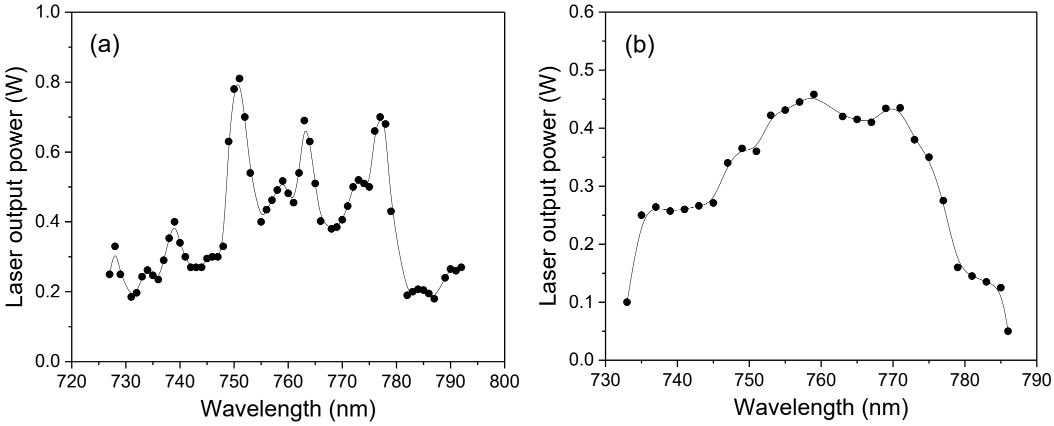

Figure 6.19. Wavelength tuning curves for the unidirectional Alexandrite ring laser, (a) using one half-wave plate (HWP_1), and (b) using two half-wave plates (HWP_1 and HWP_2).

In the first study, the unidirectional ring operation was able to be maintained from 727 to 792 nm over a total tuning range of 65 nm, shown in Figure 6.19 (a). The wavelength tuning curve exhibited modulation with a periodicity of ~12 nm (with 5 main structures peaked at 728, 739, 751, 763, 777 nm). This periodic modulation is consistent with a birefringent filtering effect of the Alexandrite crystal, which rotates the polarisation of the intracavity radiation as a function of the wavelength of the laser light when the beam path is not precisely along a crystal principal axis (the c-axis in this case). As a result, the intracavity laser light experiences loss from Brewster-cut faces of Alexandrite crystal except when the birefringence acts as an integer-wavelength waveplate, and thereby resulting in the highest power at these discrete wavelengths but preventing a smooth and continuous wavelength tuning. A potential reason for the birefringent filtering is that the crystal cut is slightly mismatched with the Brewster-cut. Smoother wavelength tuning should be expected from better crystal cut.

To improve the quality of wavelength tuning with the current Brewster-cut Alexandrite crystal, some compensation was implemented by adding a second half-wave plate (HWP_2) between the FR and the BiFi into the ring cavity shown in Figure 6.13. Figure 6.19 (b) depicts the tuning curve for this case. In this instance, the wavelength was tuned more smoothly from 733 to 786 nm with considerably reduced modulation. The polarisation of the intracavity light was partially able to offset birefringent rotation in the laser crystal but at the expense of lower output power and slightly narrower tuning range.

It is also seen in Figure 6.19 (a) and (b) that abrupt termination of lasing occurred at the extremes of the tuning range suggesting an extended tuning range appears possible. The tuning range is partially limited by the reduction of spectral coating performance of intracavity optics on either wavelength side of the Alexandrite's central lasing band ~755 nm. Further long-wavelength extension might also be possible by using higher temperatures of the Alexandrite crystal.

6.4 Summary

This chapter has presented the results from the first unidirectional SLM operation of a CW diode-pumped Alexandrite ring laser with wavelength tunability. Initially, a diode-end-pumped Alexandrite laser using a compact linear cavity design was investigated. CW laser output with a power of 1.7 W and a slope efficiency of 36.3% in a TEM_{00} beam profile (with an excellent M^2 value of 1.1) was obtained from 5.4 W pump power at 638 nm.

An enhanced X-shaped cavity was investigated and used as a precursor to the ring cavity. The enhanced design was based on the X-shaped cavity employed for the passively Q-switched operation described in Chapter 5. The pump-through mirror with a plano-concave substrate used in the previous design was equivalent to an astigmatic negative lens as seen by the pump light, and its negative impact on the pump light was quantitatively analysed. A ‘zero lens’ pump-through mirror with a convex-concave substrate was then introduced into the enhanced cavity design. Compare to the plano-concave mirror, the ‘zero lens’ mirror has been shown to have an insignificant impact on the pump light. A novel ‘displaced mode’ cavity design was used in the laser system, which allows the use of cavity mirrors with the short radius of curvature and guarantees the compactness of the system.

The unidirectional operation of a bow-tie shaped ring cavity was implemented by using a Faraday rotator combined with a half-wave plate. The SLM output was achieved with the unidirectional ring laser. The output power exceeded 1 W at 752 nm and the slope efficiency was 11%. The laser output possessed a TEM_{00} mode with a good beam quality of $M^2 < 1.2$. In addition, the emission wavelength was tuned between 727 and 792 nm using a BiFi.

These results show promise for the diode-pumped Alexandrite ring laser in SLM operation with tunability. There is clearly scope for further improvement in efficiency, stability and tuning performance, as the investigations were not fully optimized in this work. Further optimization is expected to operate the system with better quality optics and intra-cavity elements with reduced passive insertion loss and to operate the crystal at higher temperatures for efficiency enhancement and extension of tuning range to longer wavelengths. An etalon and a piezo-electric cavity length control can be added for further spectral narrowing and wavelength stabilisation, respectively.

The first successful demonstration of the SLM operation of the wavelength-tunable continuous-wave Alexandrite ring laser opens the way for the development of cost-effective and compact laser systems with narrow linewidth and precise wavelength tunability in realizing applications in areas such as LIDAR light source, high-resolution spectroscopy and fiber-optic sensors.

Chapter 7

Thesis Summary

This thesis presented work on red-diode-pumped Alexandrite lasers, with an emphasis on developing compact and low-cost formats for potential scientific and industrial applications. This final chapter summarizes the key results of the experimental and numerical work presented in this thesis, along with some suggestions for further improvement.

Laser diodes typically have a relatively narrow linewidth output. The emission wavelength of a laser diode is dependent on the chemical composition ratio of the semiconductor material and can be tailored over a wide range. These properties, along with good efficiency and compactness, make laser diodes an ideal pump source for solid-state lasers. The choice of pumping scheme is critical to a solid-state laser system as it determines the overall efficiency and the laser beam quality. After comparing the relative merit of different pumping schemes, end-pumping was selected for laser systems discussed in this work since it allows for an output with good spatial quality, low lasing threshold and high-power efficiency. End pumping, however, can induce thermal lensing which leads to the degradation of both laser beam quality and output power. Therefore, efficient thermal management and reasonable cavity design are necessary for alleviating the thermal lensing effect.

Alexandrite has many superior properties as a laser material, including high mechanical strength, high thermal conductivity and high thermal fracture limit, which makes it a promising candidate as a gain medium for sustainable high-power operation. The spectroscopic properties and temperature-dependent characteristics of Alexandrite were studied as they provide important information for understanding the lasing characteristics. For instance, ground state absorption in the lasing wavelength region and ESA in both the pump and lasing wavelength region normally have significant impacts on the laser performance and limit the wavelength tuning range. By exploring the multiple excitation bands of Alexandrite, diverse pump source options become feasible, which is desirable for a variety of applications.

Initially, a red-diode-pumped actively Q-switched Alexandrite laser was built. A free-space laser module possessing nearly linear polarised output (99% polarisation purity) and high intensity (CW output as high as 66 W) was used as the pump source for the actively Q-switched operation. Due to the highly multimodal nature of the pump diode of the output along the slow axis, the pump output was spatially redistributed using a beam shaping system. As a result, the pump beam became more circular at focus, which facilitates the mode matching condition. Q-switching was then achieved using a BBO Pockels cell. The laser was operated at pulse repetition rates between 1 and 10 kHz, this is to the best of our knowledge the first demonstration of a Q-switched Alexandrite laser under CW diode pumping. The pulse repetition rate can be increased to a characteristic frequency (~3.8 kHz) without pulse energy degradation. Past this frequency, the pulse energy was found to drop quickly. This is because the characteristic frequency is subject to the upper state lifetime (~260 μs) of Alexandrite, when the pulse repetition rate exceeds this characteristic frequency, the population inversion cannot recover to its maximum possible value between each pulse emission. The peak power, therefore, was found to decrease as the repetition rate increased, and the maximum peak power achieved was 1.19 kW at 1 kHz repetition rate.

In order to obtain shorter pulses without compromising the peak power, a cavity-dumped Q-switched system was developed by modifying the already Q-switched laser system. The cavity-dumped Q-switched operation not only considerably reduced the pulse duration but also improved the pulse energy parameter, which resulted in a significant improvement in the peak power. The highest peak power of 69.2 kW (corresponding to 200.8 μJ pulse energy and 2.9 ns pulse duration) was achieved with the Q-switched cavity-dumped Alexandrite laser, which is more than 60 times that of the standard Q-switching.

Additionally, a wavelength-tunable passively Q-switched diode-pumped Alexandrite laser was then demonstrated for the first time. As compared with active Q-switching, passive Q-switching is simple and cost-effective, which presents an alternative way to provide pulsed laser sources. A fiber-coupled laser diode module that delivers symmetric output was used as the pump laser. The passively Q-switched operation was attained using a SESAM device, and the wavelength tuning was demonstrated using a birefringent plate. The laser system used a X-shaped cavity design that contained a Brewster-angle cut crystal and curved mirrors. Due to the astigmatism introduced by the crystal and curved mirrors, an astigmatism-compensated cavity was developed. The compensation was achieved through selecting the radius of curvature and the tilt angle of the curved mirrors. Before passively Q-switching, the wavelength tunability of the Alexandrite laser was investigated in CW mode, and a wide tuning range of 69 nm (from 725 to 794 nm) was obtained. It is believed that the lower limit of the tuning range can be further extended by employing an output coupler with better-profiled reflectivity spectrum, whereas the upper limit can be expanded by optimizing the Alexandrite crystal temperature.

The Passively Q-switched operation was achieved between 775 and 781 nm. Compared to CW operation, the reduced tuning range was due to the narrow reflectivity band of the SESAM and the high intracavity losses. Highly stable passively Q-switched output yielding 73 mW average output power, and 6.9 μs pulse duration was obtained with the repetition rate of 11.2 kHz. Moreover, the pulses had a TEM_{00} beam profile with an M^2 factor less than 1.1. It is noteworthy that an even higher average power of 90 mW was achieved without using the BiFi plate. The average output power and pulse energy can be further improved by using a pump source with higher output power and better beam quality. Notably, due to the negative lensing and aberrations, the pump-through mirror used in this cavity design adversely affected the pump beam and thus the system efficiency. This issue, however, was addressed with an enhanced cavity design in the next stage of the project, where a ‘zero lens’ pump-through mirror with a shorter radius of curvature was employed instead.

Consequently, a new design based on the X-shaped cavity of the passive Q-switched system was used as a precursor to a ring cavity. This enhanced cavity design employed the customized ‘zero lens’ mirror with a convex-concave substrate instead of the mirror with a plano-concave substrate used previously. The impacts of these two different types of mirrors on the pump beam were quantitatively analysed, and the results showed that the ‘zero lens’ mirror had an insignificant impact on the pump beam as compared to the adverse spatial impact of the plano-concave mirror. In addition, a ‘displaced mode’ cavity design allowed the use of cavity mirrors with a short radius of curvature thus making the system more compact.

The unidirectional operation of the ring laser was achieved using a Faraday rotator combined with a half-wave plate. The SLM output with power exceeding 1W at 752 nm possessed a TEM_{00} mode (with a high beam quality of $M^2 < 1.2$), which represents the first successful SLM operation of a CW Alexandrite ring laser under diode pumping. Moreover, the emission wavelength was successfully tuned between 727 and 792 nm. It is expected that operating the system with better quality optics and low-insertion-loss intracavity elements will result in further improvement in efficiency and extension of tuning range. On the other hand, a longer extension of wavelength range can be achieved using higher crystal temperatures. An intracavity etalon and a piezo-electric control can also be added into the system for enhanced spectral narrowing and wavelength stabilisation, respectively.

The work presented in this thesis has contributed to the solid-state laser field, especially in terms of the development of diode-pumped Alexandrite lasers. In particular, the first demonstration of Q-switched operation in an Alexandrite laser under CW diode pumping generated the highest ever pulse repetition rate and the shortest non-mode-locked pulses, which in turn provide a valuable resource for LIDAR and altimetry applications. The first passively Q-switched diode-pumped Alexandrite laser was also demonstrated to exhibit favourable properties, such as short pulse capability and wavelength tunability. This provides a simple and cost-effective route to achieve pulsed operation of Alexandrite lasers. Despite the low pulse energies achieved with the passively Q-switched operation, the results lay the foundation for the further optimization and power scaling of this new generation of passively Q-switched Alexandrite lasers. Moreover, the first successful demonstration of the SLM operation of the diode-pumped CW Alexandrite ring laser unlocks the potential of the development of low-cost and compact laser systems with narrow linewidth and wavelength tunability. With further improvement and development of these systems, it is foreseeable that such high precision systems will be of great interest for applications including remote sensing (LIDAR) light sources.

Bibliography

[1] A. Einstein, "The Quantum Theory of Radiation," Phys. Zeitschrif **18**, 1–15 (1917).

[2] J. P. Gordon, H. J. Zeiger, and C. H. Townes, "oscillator and new Molecular microwave hyperfine structure in the microwave spectrum of NH_3," Phys. Rev. **95**, 282–284 (1954).

[3] N. G. Basov and A. M. Prokhorov, "Application of molecular beams for radio spectroscopic investigation of molecular rotational spectra," Zh. Eksp. Teor. Fiz. **27**, 431–438 (1954).

[4] N. V Karlov, O. N. Krokhin, and S. G. Lukishova, "History of quantum electronics at the Moscow Lebedev and General Physics Institutes : Nikolaj Basov and Alexander Prokhorov," Appl. Opt. **49**, F32–F46 (2010).

[5] A. L. Schawlow and C. H. Townes, "Infrared and Optical Masers," Phys. Rev. **112**, 1940–1949 (1958).

[6] T. H. Maiman, "Stimulated Optical Radiation in Ruby," Nature **187**, 493–494 (1960).

[7] W. Koechner, *Solid-State Laser Engineering*, Sixth Edition (Springer, 2006).

[8] T. Reichert, M. Neiger, H.-P. Popp, K.-J. Dietz, A. Dohn, and U. Kronert, "Continuous-wave laser pump light sources: new concepts," Appl. Opt. **32**, 6607–6609 (1993).

[9] W. Streifer, D. R. Scifres, G. L. Harnagel, D. F. Welch, J. Berger, and M. Sakamoto, "Advances in Diode Laser Pumps," IEEE J. Quantum Electron. **24**, 883–894 (1988).

[10] R. Scheps, *Introduction to Laser Diode-Pumped Solid State Lasers* (SPIE-The International Society for Optical Engineering, 2001).

[11] O. Svelto, *Principles of Lasers*, Fifth Edition (Springer, 2010).

[12] D. L. Dexter and J. H. Schulman, "Theory of Concentration Quenching in Inorganic Phosphors," J. Chem. Phys. **22**, 1063–1070 (1954).

[13] S. Chenais, F. Druon, F. Balembois, P. Georges, A. Brenier, and G. Boulon, "Diode-pumped Yb:GGG laser: comparison with Yb:YAG," Opt. Mater. **22**, 99–

106 (2003).

[14] A. I. Zagumennyi, V. G. Ostroumov, I. A. Shcherbakov, T. Jensen, J. P. Meyen, and G. Huber, "The Nd:$GdVO_4$ crystal: a new material for diode-pumped lasers," Sov. J. Quantum Electron. **22**, 1071–1072 (1992).

[15] Y. Sato and T. Taira, "The studies of thermal conductivity in $GdVO_4$, YVO_4, and $Y_3Al_5O_{12}$ measured by quasi-one-dimensional flash method," Opt. Express **14**, 10528–10536 (2006).

[16] J. Soures, S. Kumpan, and J. Hoose, "High Power Nd:Glass Laser for Fusion Applications," Appl. Opt. **13**, 2081–2094 (1974).

[17] J. S. Uppal, P. D. Gupta, and D. D. Bhawalkar, "Study of thermally induced active birefringence in Nd:glass laser rods," J. Appl. Phys. **54**, 6615–6619 (1983).

[18] G. D. Baldwin and E. P. Riedel, "Measurements of Dynamic Optical Distortion in Nd-Doped Glass Laser Rods," J. Appl. Phys. **38**, 2726–2738 (1967).

[19] E. Snitzer, "Optical Maser Action of Nd^{3+} in a Barium Crown Glass," Phys. Rev. Lett. **7**, 444–446 (1961).

[20] C. G. Young, "Glass Lasers," Proc. IEEE **57**, 1267–1289 (1969).

[21] S. M. Yarema and D. Milam, "Gain Saturation in Phosphate Laser Glasses," IEEE J. Quantum Electron. **QE-18**, 1941–1946 (1982).

[22] M. J. Weber, "Glass for Neodymium Fusion Lasers," J. Non. Cryst. Solids **42**, 189–196 (1980).

[23] R. J. Mears, L. Reekie, M. Jauncey, and D. N. Payne, "Low-noise Erbium-doped Fiber Amplifier Operating at 1.54µm," Electron. Lett. **23**, 1026–1028 (1987).

[24] E. Desurvire, J. R. Simpson, and P. C. Becker, "High-gain erbium-doped traveling-wave fiber amplifier," Opt. Lett. **12**, 888–890 (1987).

[25] C. E. Chryssou, F. Di Pasquale, and C. W. Pitt, "Improved Gain Performance In Yb^{3+}-Sensitized Er^{3+}-Doped Alumina (Al2O3) Channel Optical Waveguide Amplifiers," J. Light. Technol. **19**, 345–349 (2001).

[26] J. E. Geusic, H. M. Marcos, and L. G. Van Uitert, "Laser Oscillations in Nd-doped Yttrium Aluminum, Yttrium Gallium and Gadolinium Garnets," Appl. Phys. Lett. **4**, 182–184 (1964).

[27] L. F. Johnson, R. E. Dietz, and H. J. Guggenheim, "Optical Maser Oscillation from Ni^{2+} in MgF_2 Involving Simultaneous Emission of Phonons," Phys. Rev. Lett. **11**, 6–8 (1963).

[28] L. F. Johnson and H. J. Guggenheim, "Phonon-Terminated Coherent Emission from V^{2+} Ions in MgF_2," J. Appl. Phys. **38**, 4837–4839 (1967).

[29] L. F. Johnson and H. J. Guggenheim, "Electronic- and Phonon-Terminated Laser Emission from Ho^{3+} in BaY_2F_8," IEEE J. Quantum Electron. **QE-10**, 442–449 (1974).

[30] J. C. Walling, H. P. Jenssen, R. C. Morris, E. W. O'Dell, and O. G. Peterson, "Tunable-laser performance in BeAl(2)O(4):Cr(3+)," Opt. Lett. **4**, 182–183 (1979).

[31] P. F. Moulton, "Spectroscopic and laser characteristics of Ti:Al_2O_3," J. Opt. Soc. Am. B **3**, 125–133 (1986).

[32] P. Albers, E. Stark, and G. Huber, "Continuous-wave laser operation and quantum efficiency of titanium-doped sapphire," J. Opt. Soc. Am. B **3**, 134–139 (1986).

[33] R. Ell, U. Morgner, F. X. Kärtner, J. G. Fujimoto, E. P. Ippen, V. Scheuer, G. Angelow, T. Tschudi, M. J. Lederer, A. Boiko, and B. Luther-Davies, "Generation of 5-fs pulses and octave-spanning spectra directly from a Ti:sapphire laser," Opt. Lett. **26**, 373–375 (2001).

[34] S. Masui, T. Miyoshi, T. Yanamoto, and S. Nagahama, "1 W AlInGaN Based Green Laser Diodes," in *2013 Conference on Lasers and Electro-Optics Pacific Rim (CLEO-PR)* (2013), pp. WH3-1.

[35] S. Sawai, A. Hosaka, H. Kawauchi, K. Hirosawa, and F. Kannari, "Demonstration of a Ti:sapphire mode-lock laser pumped directly with a green diode laser," Appl. Phys. Express **7**, 1–3 (2013).

[36] K. Gürel, V. J. Wittwer, M. Hoffmann, C. J. Saraceno, S. Hakobyan, B. Resan, A. Rohrbacher, K. Weingarten, S. Schilt, and T. Südmeyer, "Green-diode-pumped femtosecond Ti:Sapphire laser with up to 450 mW average power," Opt. Express **23**, 30043–30048 (2015).

[37] E. Beyatli, I. Baali, B. Sumpf, G. Erbert, A. Leitenstorfer, A. Sennaroglu, and U. Demirbas, "Tapered diode-pumped continuous-wave alexandrite laser," J. Opt. Soc. Am. B **30**, 3184–3192 (2013).

[38] S. A. Payne, L. L. Chase, H. W. Newkirk, L. K. Smith, and W. F. Krupke, "$LiCaAlF_6:Cr^{3+}$: A Promising New Solid-state Laser Material," J. Quantum Electron. **24**, 2243–2252 (1988).

[39] U. Demirbas, D. Li, J. R. Birge, A. Sennaroglu, G. S. Petrich, L. a. Kolodziejski, F. X. Kaertner, and J. G. Fujimoto, "Low-cost, single-mode diode-pumped Cr: Colquiriite lasers," Opt. Express **17**, 14374–14388 (2009).

[40] M. Stalder, B. H. T. Chai, and M. Bass, "Flashlamp pumped Cr:$LiSrAlF_6$ laser," Appl. Phys. Lett. **58**, 216–218 (1991).

[41] S. A. Payne, L. L. Chase, L. K. Smith, W. L. Kway, and H. W. Newkirk, "Laser performance of $LiSrAlF_6:Cr^{3+}$," J. Appl. Phys. **66**, 1051–1056 (1989).

[42] F. Druon, F. Balembois, and P. Georges, "New laser crystals for the generation of ultrashort pulses," Comptes Rendus Phys. **8**, 153–164 (2007).

[43] I. T. Sorokina, E. Sorokin, and E. Wintner, "Efficient continuous-wave TEM_{00} and femtosecond Kerr-lens mode-locked Cr:LiSrGaF laser," Opt. Lett. **21**, 204–206 (1996).

[44] L. K. Smith, S. A. Payne, W. L. Kway, L. L. Chase, and B. H. T. Chai, "Investigation of the Laser Properties of $Cr^{3+}:LiSrGaF_6$," IEEE J. Quantum Electron. **28**, 2612–2618 (1992).

[45] J. C. Walling, O. G. Peterson, H. P. Jenssen, R. C. Morris, and E. W. O'Dell, "Tunable alexandrite lasers," IEEE J. Quantum Electron. **QE**-**16**, 1302–1315 (1980).

[46] J. W. Kuper, T. Chin, and H. E. Aschoff, "Extended Tuning Range of Alexandrite at Elevated Temperatures," in *Advanced Solid State Lasers*, G. Dube, ed. (Optical Society of America, 1990), Vol. 6, pp. 56–58.

[47] A. Sanchez, R. E. Fahey, A. J. Strauss, and R. L. Aggarwal, "Room-temperature continuous-wave operation of a $Ti:Al_2O_3$ laser," Opt. Lett. **11**, 363–364 (1986).

[48] R. Scheps, J. F. Myers, T. R. Glesne, and H. B. Serreze, "Monochromatic end-pumped operation of an alexandrite laser," Opt. Commun. **97**, 363–366 (1993).

[49] J. C. Walling, D. F. Heller, H. Samelson, D. J. Harter, J. A. Pete, and R. C. Morris, "Tunable Alexandrite Lasers: Development and Performance," IEEE J. Quantum Electron. **QE**-**21**, 1568–1581 (1985).

[50] E. Sorokin, "Solid-state materials for few-cycle pulse generation and amplification," in *Few-Cycle Laser Pulse Generation and Its Applications*, F. X. Kärtner, ed. (Springer, 2004), pp. 3–71.

[51] G. Dhanaraj, K. Byrappa, V. Prasad, and M. Dudley, *Handbook of Crystal Growth* (Springer, 2010).

[52] Z. Chen and G. Zhang, "Free-running emerald laser pumped by laser diode," Chinese Opt. Lett. **4**, 649–651 (2006).

[53] C.-K. Chang, J.-Y. Chang, and Y.-K. Kuo, "Optical Performance of Cr:YSO Q-switched Cr:LiCAF and Cr:LiSAF Lasers," in *High-Power Lasers and Applications Proceedings of SPIE* (2002), Vol. 4914, pp. 498–509.

[54] D. Klimm, R. Uecker, and P. Reiche, "Melting behavior and growth of colquiriite laser crystals," Cryst. Res. Technol. **40**, 352–358 (2005).

[55] R. A. Fields, M. Birnbaum, and C. L. Fincher, "Highly efficient Nd:YVO$_4$ diode-laser end-pumped laser," Appl. Phys. Lett. **51**, 1885–1886 (1987).

[56] G. Ernst, M. Bode, A. T, and H. Welling, "300-W cw diode-laser side-pumped Nd:YAG rod laser," Opt. Lett. **20**, 1148–1150 (1995).

[57] D. Golla, S. Knoke, W. Schone, A. Tiinnermann, and H. Schmidt, "High Power Continuous-Wave Diode-Laser-Pumped Nd:YAG Laser," Appl. Phys. B Lasers Opt. **58**, 389–392 (1994).

[58] J. E. Bernard and A. J. Alcock, "High-efficiency diode-pumped Nd:YVO$_4$ slab laser," Opt. Lett. **18**, 968–970 (1993).

[59] A. Minassian, B. Thompson, and M. J. Damzen, "Ultrahigh-efficiency TEM$_{00}$ diode-side-pumped Nd:YVO$_4$ laser," Appl. Phys. B Lasers Opt. **76**, 341–343 (2003).

[60] A. Giesen and J. Speiser, "Fifteen Years of Work on Thin-Disk Lasers: Results and Scaling Laws," IEEE J. Sel. Top. Quantum Electron. **13**, 598–609 (2007).

[61] A. Giesen, H. Hiigep, A. Voss, K. Wittig, U. Brauch, and H. Opower, "Scalable Concept for Diode-Pumped High-Power Solid-State Lasers," Appl. Phys. B Lasers Opt. **58**, 365–372 (1994).

[62] E. Innerhofer, T. Südmeyer, F. Brunner, R. Häring, A. Aschwanden, and R. Paschotta, "60-W average power in 810-fs pulses from a thin-disk Yb:YAG laser," Opt. Lett. **28**, 367–369 (2003).

[63] J. Negel, A. Loescher, A. Voss, D. Bauer, D. Sutter, A. Killi, M. A. Ahmed, and T. Graf, "Ultrafast thin-disk multipass laser amplifier delivering 1.4 kW (4.7 mJ, 1030 nm) average power converted to 820 W at 515 nm and 234 W at 343 nm," Opt. Express **23**, 21064–21077 (2015).

[64] H. W. Kogelnik, "Imaging of Optical Modes -- Resonators with Internal Lenses," Bell Syst. Tech. J. **44**, 455–494 (1965).

[65] H. Kogelnik and T. Li, "Laser Beams and Resonators," Proc. IEEE **54**, 1312–1329 (1966).

[66] G. Herziger and H. Weber, "Equivalent optical resonators," Appl. Opt. **23**, 1450–1452 (1984).

[67] V. Magni, "Resonators for solid-state lasers with large-volume fundamental mode and high alignment stability," Appl. Opt. **25**, 107–117 (1986).

[68] T. Y. Fan, "Heat Generation in Nd:YAG and Yb:YAG," IEEE J. Quantum Electron. **29**, 1457–1459 (1993).

[69] W. Koechner, "Thermal Lensing in a Nd:YAG Laser Rod," Appl. Opt. **9**, 2548–

2553 (1970).

[70] W. A. Clarkson and D. C. Hanna, "Resonator design considerations for efficient operation of solid-state lasers end-pumped by high-power diode-bars," in *Optical Resonators - Science and Engineering: Proceedings of the NATO Advanced Research Workshop on Optical Resonators - Theory and Design*, R. Kossowsky, M. Jelínek, and J. Novak, eds. (Springer, 1998), pp. 327–361.

[71] E.Siegman, *Lasers* (University Science Books, 1986).

[72] A. E. Siegman and S. W. Townsend, "Output Beam Propagation and Beam Quality from a Multimode Stable-Cavity Laser," IEEE J. Quantum Electron. **29**, 1212–1217 (1993).

[73] T. G. Polanyi and W. R. Watson, "Interferometric Investigation of Modes in Optical Gas Masers," J. Opt. Soc. Am. **54**, 449–453 (1964).

[74] A. Yariv, *Optical Electronics in Modern Communications*, Fifth Edition (Publishing House of Electronics Industry, 2007).

[75] A. Yariv, "Energy and Power Considerations in Injection and Optically Pumped Lasers," Proc. IEEE **51**, 1723–1731 (1963).

[76] P. Laures, "Variation of the 6328 Å gas laser output power with mirror transmission," Phys. Lett. **10**, 61–62 (1964).

[77] J. A. Baker and C. W. Peters, "Mode selection and enhancement with a ruby laser," Appl. Opt. **1**, 674 (1962).

[78] T. Li, "Mode Selection in an Aperture-Limited Concentric Maser Interferometer," Bell Syst. Tech. J. **42**, 2609–2620 (1963).

[79] K. Ait-Ameur, "Transverse mode selection in resonator with a super-Gaussian aperture," J. Mod. Opt. **40**, 1833–1838 (1993).

[80] T. Li, "Diffraction Loss and Selection of Modes in Maser Resonators with Circular Mirrors," Bell Syst. Tech. J. **44**, 917–932 (1965).

[81] P. W. Smith, "Mode selection in lasers," Proc. IEEE **60**, 422–440 (1972).

[82] J. A. Giordmaine and W. Kaiser, "Mode-selecting prism reflectors for optical masers," J. Appl. Phys. **35**, 3446–3451 (1964).

[83] V. Evtuhov and J. K. Neeland, "Study of the Output Spectra of Ruby Lasers," IEEE J. Quantum Electron. **ED-12**, 7–12 (1965).

[84] T. Li and P. W. Smith, "Mode Selection and Mode Volume Enhancement in a Gas Laser with Internal Lens," Proc. IEEE **53**, 399–400 (1965).

[85] A. E. Siegman, "Unstable Optical Resonators for Laser Applications," Proc. IEEE

53, 277–287 (1965).

[86] A. E. Siegman and R. Arrathoon, "Modes in Unstable Optical Resonators and Lens Waveguides," IEEE J. Quantum Electron. **3**, 156–163 (1967).

[87] S. R. Barone, "Optical Resonators in the Unstable Region," Appl. Opt. **6**, 861–863 (1967).

[88] L. Bergstein, "Modes of stable and unstable optical resonators," Appl. Opt. **7**, 495–504 (1968).

[89] W. F. Krupke and W. R. Sooy, "Properties of an Unstable Confocal Resonator CO_2 Laser System," IEEE J. Quantum Electron. **QE**-**5**, 575–586 (1969).

[90] J. T. LaTourette, S. F. Jacobs, and P. Rabinowitz, "Improved Laser Angular Brightness Through Diffraction Coupling," Appl. Opt. **3**, 981–982 (1964).

[91] A. Collinson, "A Stable , Single-Frequency RF-Excited Gas Laser at 6328 Å," Bell Syst. Tech. J. **44**, 1511–1519 (1965).

[92] K. M. Baird, D. S. Smith, G. R. Hanes, and S. Tsunekane, "Characteristics of a Simple Single-Mode He-Ne Laser," Appl. Opt. **4**, 569–571 (1965).

[93] J. V. Ramsay and K. Tanaka, "Construction of Single-Mode D.C. Operated He/Ne Lasers," Jpn. J. Appl. Phys. **5**, 918–923 (1966).

[94] C. F. Bruce, "Stable Single-Frequency He-Ne Laser," Appl. Opt. **10**, 880–883 (1971).

[95] S. A. Collins and G. R. White, "Interferometer laser mode selector," Appl. Opt. **2**, 448–449 (1963).

[96] T. J. Kane and R. L. Byer, "Monolithic, unidirectional single-mode Nd:YAG ring laser," Opt. Lett. **10**, 65–67 (1985).

[97] W. A. Clarkson and D. C. Hanna, "Single frequency Q-switched operation of a laser dipole-pumped, Nd:YAG ring laser," Opt. Commun. **73**, 469–474 (1989).

[98] L. J. Bromley and D. C. Hanna, "Single-frequency Q-switched operation of a diode-laser-pumped Nd:YAG ring laser using an acousto-optic modulator," Opt. Lett. **16**, 378–380 (1991).

[99] A. B. Neilson, W. A. Clarkson, and D. C. Hanna, "Single-frequency cw and Q-switched operation of a diode-pumped Nd:YAG 1.3-microm ring laser," Opt. Lett. **18**, 1426–1428 (1993).

[100] K. I. Martin, W. A. Clarkson, and D. C. Hanna, "3 W of single-frequency output at 532 nm by intracavity frequency doubling of a diode-bar-pumped Nd:YAG ring laser," Opt. Lett. **21**, 875–877 (1996).

[101] B. A. Thompson, A. Minassian, and M. J. Damzen, "Unidirectional single-frequency operation of a Nd:YVO_4 ring laser with and without a Faraday element," Appl. Opt. **43**, 3174–3177 (2004).

[102] T. F. Johnston and W. Proffitt, "Design and Performance of a Broad-Band Optical Diode to Enforce One-Direction Traveling- Wave Operation of a Ring Laser," IEEE J. Quantum Electron. **QE-16**, 483–488 (1980).

[103] R. Roy, P. A. Schulz, and A. Walther, "Acousto-optic modulator as an electronically selectable unidirectional device in a ring laser," Opt. Lett. **12**, 672–674 (1987).

[104] J. Neev and F. V Kowalski, "Unidirectional device for a ring laser using an acousto-optic modulator," Opt. Lett. **13**, 375–377 (1988).

[105] W. A. Clarkson and D. C. Hanna, "Acousto-optically induced unidirectional single mode operation of a Q-switched miniature Nd:YAG ring laser," Opt. Commun. **81**, 375–378 (1991).

[106] W. A. Clarkson, A. B. Neilson, and D. C. Hanna, "Unidirectional Operation of Ring Lasers via the Acoustooptic Effect," IEEE J. Quantum Electron. **32**, 311–325 (1996).

[107] G. T. Maker and G. P. A. Malcolm, "Single-frequency diode-pumped Nd:YAG ring laser with no intracavity elements," Opt. Lett. **18**, 1813–1815 (1993).

[108] W. G. Wagner and B. A. Lengyel, "Evolution of the giant pulse in a laser," J. Appl. Phys. **34**, 2040–2046 (1963).

[109] R. W. Hellwarth, *Control of Fluorescent Pulsations* (Columbia University Press, 1961).

[110] R. C. Benson and M. R. Mirarchi, "The Spinning Reflector Technique for Ruby Laser Pulse Control," IEEE Trans. Mil. Electron. **8**, 13–21 (1964).

[111] E. I. Gordon, "A Review of Acoustooptical Deflection and Modulation Devices," Proc. IEEE **54**, 1391–1401 (1966).

[112] R. O. Carpenter, "The Electro-Optic Effect in Uniaxial Crystals of the Dihydrogen Phosphate Type .*,† III . Measurement of Coefficients," J. Opt. Soc. Am. **40**, 225–229 (1950).

[113] U. Keller, K. J. Weingarten, X. K. Franz, D. Kopf, B. Braun, I. D. Jung, R. Fluck, H. Clemens, N. Matuschek, and J. A. Der Au, "Semiconductor Saturable Absorber Mirrors (SESAM ' s) for Femtosecond to Nanosecond Pulse Generation in Solid-State Lasers," IEEE J. Sel. Top. Quantum Electron. **2**, 435–453 (1996).

[114] J. Dong, P. Deng, Y. Liu, Y. Zhang, J. Xu, W. Chen, and X. Xie, "Passively Q-switched Yb:YAG laser with Cr^{4+}:YAG as the saturable absorber," Appl. Opt. **40**,

4303–4307 (2001).

[115] B. Yao, Y. Tian, G. Li, and Y. Wang, "InGaAs / GaAs saturable absorber for diode-pumped passively Q-switched dual-wavelength Tm:YAP lasers," Opt. Express **18**, 13574–13579 (2010).

[116] S. Y. Set, H. Yaguchi, Y. Tanaka, and M. Jablonski, "Ultrafast Fiber Pulsed Lasers Incorporating Carbon Nanotubes," IEEE J. Sel. Top. Quantum Electron. **10**, 137–146 (2004).

[117] A. Schmidt, S. Rivier, G. Steinmeyer, J. H. Yim, W. B. Cho, S. Lee, F. Rotermund, M. C. Pujol, X. Mateos, M. Aguiló, F. Díaz, V. Petrov, and U. Griebner, "Passive mode locking of Yb:KLuW using a single-walled carbon nanotube saturable absorber," Opt. Lett. **33**, 729–731 (2008).

[118] P. T. Guerreiro, S. Ten, N. F. Borrelli, J. Butty, G. E. Jabbour, and N. Peyghambarian, "PbS quantum-dot doped glasses as saturable absorbers for mode locking of a Cr:forsterite laser," Appl. Phys. Lett. **71**, 1595–1597 (1997).

[119] M. N. Cizmeciyan, J. W. Kim, S. Bae, B. H. Hong, F. Rotermund, and A. Sennaroglu, "Graphene mode-locked femtosecond Cr:ZnSe laser at 2500 nm," Opt. Lett. **38**, 341–343 (2013).

[120] G. Sobon, J. Sotor, I. Pasternak, A. Krajewska, W. Strupinski, and K. M. Abramski, "Multilayer graphene-based saturable absorbers with scalable modulation depth for mode-locked Er- and Tm-doped fiber lasers," Opt. Mater. Express **5**, 2884–2894 (2015).

[121] Z. Wang, L. Zhan, M. Qin, J. Wu, L. Zhang, Z. Zou, and K. Qian, "Passively Q-Switched Er-Doped Fiber Lasers Using Alcohol," J. Light. Technol. **33**, 4857–4861 (2015).

[122] T. Xian, L. Zhan, L. Gao, W. Zhang, and W. Zhang, "Passively Q-switched fiber lasers based on pure water as the saturable absorber," Opt. Lett. **44**, 863–866 (2019).

[123] E.F.Farrell, J.H.Fang, and R.E.Newnham, "Refinement of the Chrysoberyl structure," Am. Mineral. **48**, 804–810 (1963).

[124] M. L. Shand, J. C. Walling, and H. P. Jenssen, "Ground State Absorption in the Lasing Wavelength Region of Alexandrite: Theory and Experiment," IEEE J. Quantum Electron. **QE**-**18**, 167–169 (1982).

[125] H. Samelson, J. C. Walling, and D. F. Heller, "Unique applications of alexandrite lasers," in *Advanced Laser Technology and Applications* (1982), pp. 85–94.

[126] P. K. Cheo, *Handbook of Solid-State Lasers* (Marcel Dekker, Inc., 1989).

[127] M. J. Weber, D. Milam, and W. L. Smith, "Nonlinear Refractive Index of Glasses

and Crystals," Opt. Eng. **17**, 463–469 (1978).

[128] J. Steve Guch and C. E. Jones, "Alexandrite-laser performance at high temperature.," Opt. Lett. **7**, 608–610 (1982).

[129] R. C. Powell, L. Xi, and X. Gang, "Spectroscopic properties of Alexandrite crystals," Phys. Rev. B **32**, 2788–2797 (1985).

[130] W. R. Kerridge, "Diode-pumped Alexandrite laser development and vortex mode generation," PhD Thesis, Imperial College London (2018).

[131] D. E. McCumber, "Theory of Phonon-Terminated Optical Masers," Phys. Rev. **134**, A299–A306 (1964).

[132] Z. Zhang, K. T. V. Grattan, and A. W. Palmer, "Thermal characteristics of alexandrite fluorescence decay at high temperatures, induced by a visible laser diode emission," J. Appl. Phys. **73**, 3493–3498 (1993).

[133] M. L. Shand and H. P. Jenssen, "Temperature dependence of the excited-state absorption of Alexandrite," IEEE J. Quantum Electron. **QE**-**19**, 480–484 (1983).

[134] S. K. Gayen, W. B. Wang, V. Petričević, and R. R. Alfano, "Nonradiative transition dynamics in alexandrite," Appl. Phys. Lett. **49**, 437–439 (1986).

[135] M. L. Shand, J. C. Walling, and R. C. Morris, "Excited-state absorption in the pump region of alexandrite," J. Appl. Phys. **52**, 953–955 (1981).

[136] M. L. Shand and J. C. Walling, "Excited-State Absorption in the Lasing Wavelength Region of Alexandrite," IEEE J. Quantum Electron. **QE**-**18**, 1152–1155 (1982).

[137] J. C. Walling, O. G. Peterson, and R. C. Morris, "Tunable CW Alexandrite Laser," IEEE J. Quantum Electron. **QE**-**16**, 120–121 (1980).

[138] H. Samelson, J. C. Walling, T. Wernikowski, and D. J. Harter, "CW Arc-Lamp-Pumped Alexandrite Lasers," IEEE J. Quantum Electron. **24**, 1141–1150 (1988).

[139] H. Samelson and D. J. Harter, "High-pressure mercury arc lamp excited cw alexandrite lasers," in *Conference on Lasers and Electro-Optics* (1984), pp. 19–22.

[140] K. Torizuka, M. Yamashita, and T. Yabiku, "Continuous-wave alexandrite laser pumped by a direct-current mercury arc lamp," Appl. Opt. **32**, 7394–7398 (1993).

[141] J. C. Walling and O. G. Peterson, "High Gain Laser Performance in Alexandrite," IEEE J. Quantum Electron. **QE**-**16**, 119–120 (1980).

[142] C. J. Lee, P. J. M. van der Slot, and K.-J. Boller, "A gain-coefficient switched Alexandrite laser," J. Phys. D. Appl. Phys. **46**, 1–4 (2013).

[143] S. T. Lai and M. L. Shand, "High efficiency cw laser-pumped tunable alexandrite laser," J. Appl. Phys. **54**, 5642–5644 (1983).

[144] J. W. Kuper and D. C. Brown, "Green pumped Alexandrite lasers," in *Conference on Lasers and Applications in Science and Engineering* (2005), Vol. 5707, pp. 265–270.

[145] J. W. Kuper and D. C. Brown, "High efficiency CW green pumped Alexandrite lasers," Proc. SPIE - Solid State Lasers XV Technol. Devices **6100**, 1–8 (2006).

[146] S. Ghanbari, R. Akbari, and A. Major, "Femtosecond Kerr-lens mode-locked Alexandrite laser," Opt. Express **24**, 14836–14840 (2016).

[147] S. Ghanbari, K. A. Fedorova, A. B. Krysa, E. U. Rafailov, and A. Major, "Femtosecond Alexandrite laser passively mode-locked by an InP/InGaP quantum-dot saturable absorber," Opt. Lett. **43**, 232–234 (2018).

[148] W. R. Kerridge-Johns and M. J. Damzen, "Temperature effects on tunable cw Alexandrite lasers under diode end-pumping," Opt. Express **26**, 7771–7785 (2018).

[149] X. Sheng, G. Tawy, J. Sathian, A. Minassian, and M. J. Damzen, "Unidirectional single-frequency operation of a continuous-wave Alexandrite ring laser with wavelength tunability," Opt. Express **26**, 31129–31136 (2018).

[150] M. Fibrich, J. Šulc, D. Vyhlídal, H. Jelínková, and M. Čech, "Alexandrite spectroscopic and laser characteristic investigation within a 78–400 K temperature range," Laser Phys. **27**, 1–6 (2017).

[151] M. Fibrich, J. Šulc, D. Vyhlídal, H. Jelínková, and M. Čech, "Temperature influence on spectroscopic and lasing properties of blue laser diode pumped Alexandrite crystal," in *Proceedings of SPIE* (2018), Vol. 10511, pp. 1–8.

[152] R. Scheps, B. M. Gately, J. F. Myers, J. S. Krasinski, and D. F. Heller, "Alexandrite laser pumped by semiconductor lasers," Appl. Phys. Lett. **56**, 2288–2290 (1990).

[153] X. Peng, A. Marrakchi, J. C. Walling, and D. F. Heller, "Watt-level red and UV output from a CW diode array-pumped tunable alexandrite laser," in *Conference on Lasers & Electro-Optics* (2005), pp. 479–481.

[154] A. Teppitaksak, A. Minassian, G. M. Thomas, and M. J. Damzen, "High efficiency >26 W diode end-pumped Alexandrite laser," Opt. Express **22**, 16386–16392 (2014).

[155] I. Yorulmaz, E. Beyatli, A. Kurt, A. Sennaroglu, and U. Demirbas, "Efficient and low-threshold Alexandrite laser pumped by a single-mode diode," Opt. Mater. Express **4**, 776–789 (2014).

[156] E. A. Arbabzadah and M. J. Damzen, "Fibre-coupled red diode-pumped

Alexandrite TEM_{00} laser with single and double-pass end-pumping," Laser Phys. Lett. **13**, 1–6 (2016).

[157] G. M. Thomas, A. Minassian, X. Sheng, and M. J. Damzen, "Diode-pumped Alexandrite lasers in Q-switched and cavity-dumped Q-switched operation," Opt. Express **24**, 27212–27224 (2016).

[158] M. J. Damzen, G. M. Thomas, and A. Minassian, "Diode-side-pumped Alexandrite slab lasers," Opt. Express **25**, 11622–11636 (2017).

[159] U. Parali, X. Sheng, A. Minassian, G. Tawy, J. Sathian, G. M. Thomas, and M. J. Damzen, "Diode-pumped Alexandrite laser with passive SESAM Q-switching and wavelength tunability," Opt. Commun. **410**, 970–976 (2018).

[160] P. Pichon, A. Barbet, J.-P. Blanchot, F. Druon, F. Balembois, and P. Georges, "LED-pumped alexandrite laser oscillator and amplifier," Opt. Lett. **42**, 4191–4194 (2017).

[161] M. Lando, Y. Shimony, R. M. J. Benmair, D. Abramovich, V. Krupkin, and A. Yogev, "Visible solar-pumped lasers," Opt. Mater. **13**, 111–115 (1999).

[162] Light. Age. Inc., "PAL^{TM} Pulsed Alexandrite Laser System," Retrieved from http://lightage.com/web/pal-pulsed-alexandrite-laser/.

[163] D. J. Goldberg, "Laser Treatment of Pigmented Lesions," Dermatol. Clin. **15**, 397–407 (1977).

[164] J. P. Trafeli, J. M. Kwan, K. J. Meehan, Y. Domankevitz, S. Gilbert, K. Malomo, and E. V. Ross, "Use of a long-pulse alexandrite laser in the treatment of superficial pigmented lesions," Dermatologic Surg. **33**, 1477–1482 (2007).

[165] S. Tatlidede, O. Egemen, A. Saltat, G. Turgut, A. Karasoy, and I. Kuran, "Hair Removal with the Long-Pulse Alexandrite Laser," Aesthetic Surg. **25**, 138–143 (2005).

[166] S. A. Laughlin and D. K. Dudley, "Long-Term Hair Removal Using a 3-Millisecond Alexandrite Laser," J. Cutan. Med. Surg. **4**, 83–88 (2000).

[167] R. E. Fitzpatrick and M. P. Goldman, "Tattoo removal with the Alexandrite laser: a clinical and histologic study," in *Proceedings of SPIE* (1993), Vol. 1876, pp. 110–111.

[168] T. S. Alster, "Q-switched alexandrite laser treatment (755 nm) of professional and amateur tattoos," Am. Acad. Dermatology **33**, 69–73 (1995).

[169] M. L. Leuenberger, M. W. Mulas, T. R. Hata, M. P. Goldman, R. E. Fitzpatrick, and J. M. Grevelink, "Comparison of the Q-Switched Alexandrite, Nd:YAG, and Ruby Lasers in Treating Blue-Black Tattoos," Dermatologic Surg. **25**, 10–14 (1999).

[170] M. J. Damzen, G. M. Thomas, A. Teppitaksak, and A. Minassian, "Progress in diode-pumped Alexandrite lasers as a new resource for future space Lidar missions," in *Proceedings of SPIE* (2014), Vol. 10563, pp. 1–9.

[171] D. Bruneau, H. Cazeneuve, C. Loth, and J. Pelon, "Double-pulse dual-wavelength alexandrite laser for atmospheric water vapor measurement.," Appl. Opt. **30**, 3930–3937 (1991).

[172] D. Bruneau, T. A. des Lions, P. Quaglia, and J. Pelon, "Injection-seeded pulsed alexandrite laser for differential absorption lidar application," Appl. Opt. **33**, 3941–3950 (1994).

[173] P. Ponsardin, N. S. Higdon, B. E. Grossmann, and E. V. Browell, "Spectral control of an alexandrite laser for an airborne water-vapor differential absorption lidar system," Appl. Opt. **33**, 6439–6450 (1994).

[174] V. Wulfmeyer and J. Bösenberg, "Single-mode operation of an injection-seeded alexandrite ring laser for application in water-vapor and temperature differential absorption lidar," Opt. Lett. **21**, 1150–1152 (1996).

[175] V. Wulfmeyer, "Ground-based differential absorption lidar for water-vapor and temperature profiling: development and specifications of a high-performance laser transmitter," Appl. Opt. **37**, 3804–3824 (1998).

[176] U. von Zahn and J. Hoffner, "Mesopause temperature profiling by potassium lidar," Geophys. Res. Lett. **23**, 141–144 (1996).

[177] J. Höffner and F. J. Lübken, "Potassium lidar temperatures and densities in the mesopause region at Spitsbergen (78°N)," J. Geophys. Res. **112**, 1–14 (2007).

[178] J. A. Mckay and T. D. Wilkerson, "Diode-pumped alexandrite laser for DIAL and Doppler lidar," in *Proceedings of SPIE* (1997), Vol. 3127, pp. 124–132.

[179] W. Krichbaumer, H. Herrmann, E. Nagel, R. Häring, J. Streicher, C. Werner, A. Mehnert, T. Halldorsson, S. Heinemann, P. Peuser, and N. P. Schmitt, "A diode-pumped Nd:YAG lidar for airborne cloud measurements," Opt. Laser Technol. **25**, 283–287 (1993).

[180] M. Ostermeyer, P. Kappe, R. Menzel, and V. Wulfmeyer, "Diode-pumped Nd:YAG master oscillator power amplifier with high pulse energy, excellent beam quality, and frequency-stabilized master oscillator as a basis for a next-generation lidar system," Appl. Opt. **44**, 582–590 (2005).

[181] T. D. Kawahara, T. Kitahara, F. Kobayashi, Y. Saito, and A. Nomura, "Sodium temperature lidar based on injection seeded Nd:YAG pulse lasers using a sum-frequency generation technique," Opt. Express **19**, 3553–3561 (2011).

[182] T. D. Kawahara, S. Nozawa, N. Saito, T. Kawabata, T. T. Tsuda, and S. Wada,

"Sodium temperature/wind lidar based on laser-diode-pumped Nd:YAG lasers deployed at Tromsø, Norway (696°N, 192°E)," Opt. Express **25**, A491–A501 (2017).

[183] J. R. Miller, E. W. Hare, and J. Wu, "Quantitative characterization of the vegetation red edge reflectance 1. An inverted-Gaussian reflectance model," Int. J. Remote Sens. **11**, 1755–1773 (1990).

[184] A. Ansmann, R. Neuber, P. Rairoux, and U. Wandinger, *Advances in Atmospheric Remote Sensing with Lidar* (Springer, 2006).

[185] A. Munk, B. Jungbluth, M. Strotkamp, H.-D. Hoffmann, R. Poprawe, J. Höffner, and F.-J. Lübken, "Diode-pumped alexandrite ring laser in single-longitudinal mode operation for atmospheric lidar measurements," Opt. Express **26**, 14928–14935 (2018).

[186] A. Munk, B. Jungbluth, M. Strotkamp, H.-D. Hoffmann, R. Poprawe, and J. Höffner, "Alexandrite laser in Q-switched, single longitudinal mode operation pumped by a fiber-coupled diode module," in *Proceedings of SPIE* (2019), Vol. 10896, pp. 1–9.

[187] A. Munk, B. Jungbluth, M. Strotkamp, S. Gaussmann, H.-D. Hoffmann, R. Poprawe, and J. Hoeffner, "Diode-pumped Alexandrite Ring Laser," in *Conference of Advanced Solid State Lasers* (2015), pp. 1–3.

[188] W. R. Kerridge-Johns and M. J. Damzen, "Analytical model of tunable Alexandrite lasing under diode end-pumping with experimental comparison," J. Opt. Soc. Am. B **33**, 2525–2534 (2016).

[189] G. D. Goodno, Z. Guo, R. J. D. Miller, I. J. Miller, J. W. Montgomery, S. R. Adhav, and R. S. Adhav, "Investigation of β-BaB_2O_4 as Q switch for high power applications," Appl. Phys. Lett. **66**, 1575–1577 (1995).

[190] L. Mcdonagh and R. Wallenstein, "47 W, 6 ns constant pulse duration, high-repetition-rate cavity-dumped Q-switched TEM_{00} Nd:YVO_4 oscillator," Opt. Lett. **31**, 3303–3305 (2006).

[191] A. A. Vuylsteke, "Theory of Laser Regeneration Switching," J. Appl. Phys. **34**, 1615–1622 (1963).

[192] H. W. Kogelnik, E. P. Ippen, A. Dienes, and C. V. Shank, "Astigmatically Compensated Cavities for CW Dye Lasers," IEEE J. Quantum Electron. **QE-8**, 373–379 (1972).

[193] S. Zhu, "Birefringent filter with tilted optic axis for tuning dye lasers: theory and design," Appl. Opt. **29**, 410–415 (1990).

[194] A. L. Bloom, "Modes of a laser resonator containing tilted birefringent plates,"

J. Opt. Soc. Am. **64**, 447–452 (1974).

[195] P. J. Schlosser, J. E. Hastie, S. Calvez, A. B. Krysa, and M. D. Dawson, "InP/AlGaInP quantum dot semiconductor disk lasers for CW TEM_{00} emission at 716 - 755 nm," Opt. Express **17**, 21782–21787 (2009).

[196] S. C. Collins, T. D. Wilkerson, V. B. Wickwar, D. Rees, J. C. Walling, and D. F. Heller, *The Alexandrite Ring Laser: A Spectrally Narrow Lidar Light Source for Atmospheric Fluorescence and Absorption Observations* (Springer Verlag, 1997).

[197] X. Chu, "Alexandrite-ring-laser-based Fe Doppler lidar for mobile/airborne deployment," in *23rd International Laser Radar Conference* (2006), pp. 1–4.

[198] P. Bakule, P. E. G. Baird, M. G. Boshier, S. L. Cornish, D. F. Heller, K. Jungmann, I. C. Lane, V. Meyer, P. H. G. Sandars, W. T. Toner, M. Towrie, and J. C. Walling, "A chirp-compensated, injection-seeded alexandrite laser," Appl. Phys. B Lasers Opt. **71**, 11–17 (2000).

[199] E. M. Strzelecki, D. A. Cohen, and L. A. Coldren, "Investigation of Tunable Single Frequency Diode Lasers for Sensor Applications," J. Light. Technol. **6**, 1610–1618 (1988).

[200] C. Spiegelberg, J. Geng, Y. Hu, Y. Kaneda, S. Jiang, and N. Peyghambarian, "Low-Noise Narrow-Linewidth Fiber Laser at 1550nm," J. Light. Technol. **22**, 57–62 (2004).

[201] E. Hecht, *Optics*, Fifth Edition (Pearson, 2017).

[202] B. Zhou, T. J. Kane, G. J. Dixon, and R. L. Byer, "Efficient , frequency-stable laser-diode-pumped Nd:YAG laser," Opt. Lett. **10**, 62–64 (1985).

[203] D. L. Sipes, "Highly efficient neodymium:yttrium aluminum garnet laser end pumped by a semiconductor laser array," Appl. Phys. Lett. **47**, 74–76 (1985).

[204] M. Faradey, "Experimental researches in electricity.—Nineteenth series," Philos. Trans. R. Soc. London **136**, 1–20 (1846).